

Evaluating the Performance of the ProtoDUNE–SP Detector using Michel Electrons

Aidan Reynolds

University College
University of Oxford

*A thesis submitted for the degree of
Doctor of Philosophy*

Hilary 2020

Abstract

This thesis presents the results of a study of electromagnetic interactions in the ProtoDUNE–SP liquid argon time projection chamber (LArTPC) detector. The LArTPC detector technology provides high spatial resolution on the final states of neutrino interactions, allowing interaction modes to be distinguished based on the event topology. In order to perform high precision measurements of ν_e in LArTPC detectors, electrons must be identified and their energy accurately reconstructed. In this work EM activity is studied in the 10–50 MeV range using Michel electrons as a source with a well defined energy spectrum. The sensitivity, bias, and energy scale are studied and the implications for neutrino physics in the Deep Underground Neutrino Experiment are discussed.

Evaluating the Performance of the ProtoDUNE-SP Detector using Michel Electrons



Aidan Reynolds
University College
University of Oxford

A thesis submitted for the degree of
Doctor of Philosophy
Hilary 2020

Abstract

This thesis presents the results of a study of electromagnetic interactions in the ProtoDUNE-SP liquid argon time projection chamber (LArTPC) detector. The LArTPC detector technology provides high spatial resolution on the final states of neutrino interactions, allowing interaction modes to be distinguished based on the event topology. In order to perform high precision measurements of ν_e in LArTPC detectors, electrons must be identified and their energy accurately reconstructed. In this work EM activity is studied in the 10–50 MeV range using Michel electrons as a source with a well defined energy spectrum. The sensitivity, bias, and energy scale are studied and the implications for neutrino physics in the Deep Underground Neutrino Experiment are discussed.

Contents

List of Figures	vi
Glossary	ix
1 Introduction	1
2 Neutrino Physics	5
2.1 A Brief History of Neutrino Physics	6
2.2 Neutrinos in the Standard Model	12
2.3 Neutrino Oscillations	14
2.3.1 Neutrino Oscillations in Vacuum	15
2.3.2 Neutrino Oscillations in Matter	17
2.3.3 Current Knowledge and Open Questions	19
2.4 Neutrino Interactions	22
2.5 Supernova Neutrinos	26
2.5.1 Core-collapse Supernova Dynamics	27
2.5.2 SN1987A	29
2.5.2.1 Kamiokande-II	29
2.5.2.2 IMB	29
2.5.2.3 Baksan	30
2.5.3 Supernova Neutrino Prospects in DUNE	31
2.5.3.1 Supernova Neutrino Interactions in Liquid Argon .	32
2.5.3.2 Supernova Neutrino Events in DUNE	33
3 The ProtoDUNE-SP Experiment	35
3.1 ProtoDUNE-SP in the Context of DUNE	36
3.1.1 Liquid Argon Time Projection Chambers	37
3.2 The ProtoDUNE-SP Detector	40
3.2.1 The Liquid Argon TPC	40
3.2.2 The Photon Detection System	42
3.3 The H4 beamline	44
3.4 The Cosmic Ray Tagger	46
3.5 The Data Acquisition System	47

3.6	Simulation	49
3.7	Reconstruction	50
3.8	ProtoDUNE-SP Online Monitoring System	56
3.8.1	Data Processing	57
3.8.2	Monitoring Web Interface	63
4	Electromagnetic Energy Loss in Liquid Argon	69
4.1	Electromagnetic Energy Loss in Matter	69
4.1.1	Energy Loss for Heavy Charged Particles	70
4.1.2	Energy Loss for Electrons	70
4.1.3	Energy Loss for Photons	73
4.1.4	Typical Interaction Signatures in ProtoDUNE-SP	76
5	Neural Networks	78
5.1	Artificial Neural Networks	79
5.1.1	Convolutional Neural Networks	81
5.1.2	Residual Neural Networks	83
5.2	Supervised Learning	84
5.2.1	Backpropagation	84
5.2.2	Batch Normalisation	84
5.2.3	Regularisation	84
6	Charge Identification with Convolutional Neural Networks	85
6.1	Neural Networks	85
6.2	Hit Identification with Convolutional Neural Networks	87
6.3	Performance on ProtoDUNE-SP Simulation	91
6.4	Validation and Performance on ProtoDUNE-SP Data	94
7	Study of Michel Electrons in ProtoDUNE-SP	99
7.1	Michel Electrons in Liquid Argon	100
7.2	Michel Electron Event Selection	104
7.3	Michel Electron Energy Reconstruction	109
7.3.1	Michel Electron Hit Tagging with U-Nets	109
7.3.2	Michel Electron Reconstruction	111
7.3.2.1	Hit Selection	111
7.3.2.2	Ionisation Energy Reconstruction	115
7.3.2.3	Michel Electron Energy Reconstruction	117
7.4	Conclusions	122

8 Implications for DUNE	124
8.1 Supernova Neutrinos in DUNE	124
8.2 Impacts of Energy Uncertainties	124
9 Conclusions	125
References	126

List of Figures

2.1	Ratio of data to Monte Carlo for electron and muon neutrino fluxes measured by the Super Kamiokande experiment as a function of L/E_ν .	10
2.2	Solar neutrino flux composition as measured by the SNO experiment.	11
2.3	Ratio of observed neutrino flux to the predicted flux in the absence of neutrino oscillations in the KamLAND experiment.	12
2.4	Feynman diagrams for neutrino scattering in matter.	17
2.5	The two possible neutrino mass orderings: normal and inverted.	18
2.6	90% confidence intervals for $\sin^2(\theta_{23}) - \Delta m_{32}^2$.	21
2.7	Confidence intervals for δ_{CP} from the T2K experiment [42].	23
2.8	Confidence intervals for δ_{CP} from the NO ν A experiment [38].	24
2.9	Muon neutrino cross section as a function of energy.	26
2.10	Measured supernova neutrino events from SN1987A in Kamiokande-II.	30
2.11	Supernova neutrino energy spectrum.	31
2.12	Supernova neutrino cross sections in liquid argon.	32
2.13	Supernova neutrinos predictions for a 10kpc supernova in DUNE.	34
3.1	The Deep Underground Neutrino Experiment.	36
3.2	LArTPC detection principal.	38
3.3	The main components of the ProtoDUNE-SP TPC.	41
3.4	The operating principal of the photon detector modules in ProtoDUNE-SP.	43
3.5	Schematic of the H4 beamline magnets and instrumentation.	45
3.6	Time of flight vs momentum distributions from the H4 beamline instrumentation.	45
3.7	Location of the H4 beamline and cosmic ray taggers in relation to the ProtoDUNE-SP detector.	47
3.8	Outline of the data acquisition system in ProtoDUNE-SP.	48
3.9	Example of noise filtering and 2D deconvolution in ProtoDUNE-SP data.	51
3.10	Reconstructed hits from ProtoDUNE-SP data.	52
3.11	Diagram demonstrating the track stitching algorithm in ProtoDUNE-SP.	53

3.12	Reconstructed particle hierarchy from Pandora.	54
3.13	dE/dx vs residual range for a stopping muon sample in ProtoDUNE–SP data.	56
3.14	Data flow in the ProtoDUNE–SP online monitoring system.	57
3.15	Examples of online monitoring plots for the TPC data.	60
3.16	An example of a beam window event display from the ProtoDUNE–SP online monitoring system.	61
3.17	Examples of online monitoring plots for the photon detection system data.	62
3.18	Examples of online monitoring plots for the timing and trigger data. .	63
3.19	Examples of online monitoring plots for the beam instrumentation. .	64
3.20	Examples of online monitoring plots for the cosmic ray tagger. . . .	65
3.21	Data flow diagram for the web interface in the ProtoDUNE–SP online monitoring system.	65
3.22	An example of an online monitoring page.	66
3.23	Example of the dynamic binning algorithm in the ProtoDUNE–SP online monitoring system.	67
4.1	Stopping power as a function of energy for muons in liquid argon. .	71
4.2	Stopping power as a function of energy for electrons in liquid argon. .	73
4.3	Photon interaction cross sections in liquid argon.	75
4.4	Photon mean free path in liquid argon.	75
4.5	Typical particle interactions in ProtoDUNE–SP for different particle species.	77
5.1	Graphical representation of an individual neuron in an artificial neural network.	79
5.2	A graphical representation of a multi–layer perceptron.	80
5.3	A graphical representation of a convolutional neural network.	83
6.1	Example CNN input images.	89
6.2	Network architecture used for hit classification.	91
6.3	Validation and training set losses.	92
6.4	Shower classifier output distributions.	93
6.5	Michel classifier output distributions.	94
6.6	ROC curves.	95
6.7	CNN output on an event from ProtoDUNE–SP data.	97
6.8	Output distributions for the track classifier on reconstructed Pandora objects.	98
7.1	Michel electron energy spectra in Liquid Argon	101

7.2	Michel electron candidate event from ProtoDUNE–SP data.	101
7.3	Properties of radiated energy deposits from Michel electrons.	103
7.4	Spatial distribution of radiated ionisation deposits.	104
7.5	Available ionisation energy vs true Michel electron energy.	105
7.6	Fraction of Michel electron energy collected vs collection radius. .	106
7.7	Fraction of Michel–like hits in the best Michel electron candidate. .	107
7.8	Purity and efficiency of Michel electron event selection as a function of energy.	108
7.9	CNN architecture used to select ionisation energy deposits.	111
7.10	U-Net training and validation loss as a function of epoch.	112
7.11	Example input, true output, and prediction images for U-Net.	113
7.12	U-Net Predicted Distribution.	114
7.13	Number of hits in Michel electron events.	114
7.14	U-Net output distribution.	115
7.15	U-Net purity vs completeness.	116
7.16	Reconstructed Hit Ionisation Energy	117
7.17	Reconstructed Michel Electron Ionisation Energy	118
7.18	Reconstructed Ionisation vs True Ionisation.	118
7.19	Fractional energy difference between reconstructed and true Michel electron energy.	119
7.20	Energy resolution and bias as a function of true ionisation energy. .	119
7.21	Quadratic Energy Scale Factor.	121
7.22	Reconstructed Energy vs True Michel Electron Energy.	121
7.23	Fractional energy difference between reconstructed and true Michel electron energy.	122
7.24	Energy resolution and bias as a function of true Michel electron energy.	123

Glossary

DUNE Deep Underground Neutrino Experiment.

EW Electroweak.

LArTPC . . . Liquid Argon Time Projection Chamber.

MLP Multi-layer Perceptron

PMNS Pontecorvo—Maki—Nakagawa—Sakata

SSM Standard Solar Model

1

Introduction

Since the discovery of neutrino flavour oscillations, which implies that neutrinos have mass, neutrino physics has enjoyed a period of rapid development. The field has begun to transition into an era of precision, with many of the parameters governing these oscillations having been well constrained. The fact that neutrinos have mass, and the success of the PMNS theory in describing neutrino oscillations, leads to a number of fundamental questions which have important implications in both particle physics and cosmology:

- What is the mechanism giving rise to neutrino mass?
- Are neutrinos Dirac or Majorana particles?
- What is the absolute scale and ordering of the neutrino masses?
- Do neutrinos and anti-neutrinos oscillate differently, and would this help to explain the matter anti-matter asymmetry in the universe?

In addition to these questions from the neutrino physics community, the high resolution and large masses of modern neutrino detectors make them useful tools for both astronomy and astrophysics. 2017 has widely been considered as the dawn of multi-messenger astronomy, with a measurement of gravitational waves at the

Laser Interferometer Gravitational-Wave Observatory (LIGO) being correlated with measurements of a neutron star merger from electromagnetic telescopes [1]. This measurement was shortly followed by a similar correlation but in the neutrino sector between a high energy neutrino event in the IceCube Neutrino Observatory and a number of traditional telescopes [2]. Within our galaxy, neutrino detectors provide a unique opportunity to understand the underlying mechanisms in supernovae; in the case of such a supernova, the structure of the neutrino flux at earth provides a mechanism to measure effects in the early stages of the supernova burst which are inaccessible with electromagnetic measurements [3].

Each of these questions places unique constraints on the design of an appropriate neutrino detector. The discovery of a matter anti-matter asymmetry in neutrino oscillations can be answered by making precise measurements of neutrino oscillations. This requires reliably identifying the flavour and energy of neutrinos in order to measure the appearance and disappearance spectra associated with neutrinos produced in long baseline neutrino experiments. To identify the low energy electrons produced in supernova neutrino interactions, a detector with low thresholds and low backgrounds is required. The Deep Underground Neutrino Experiment (DUNE) aims to tackle these challenges by utilising the Liquid Argon Time Projection Chamber (LArTPC) technology, whose high spatial and calorimetric resolution allows for more accurate topological classification of neutrino interactions [4]. To achieve these goals, a significant programme of LArTPC research is ongoing with construction, reconstruction, and analysis methods all under development in a number of LArTPC based experiments [5–8].

This thesis presents an analysis of charged particle interactions in the ProtoDUNE-SP LArTPC detector. A hit classification algorithm is developed and a sample of Michel electrons is used to provide a measurement of electron energy bias for low energy electrons. The analysis described in this thesis uses data collected with the ProtoDUNE-SP detector between August and November 2018.

Michel electrons have an energy spectrum spanning 0–60 MeV; understanding electrons in this energy range is important as they are the same energy as those

produced when neutrinos from supernova bursts interact. In a LArTPC at these energies, the energy deposition of electrons transitions between ionisation dominated and radiation dominated regimes making for a particularly complicated combined event topology [9]. The work presented here details a reconstruction strategy based on augmenting hit identification from a convolution neural network with simple clustering to identify and reconstruct Michel electron events. Analysis of these Michel electron events in ProtoDUNE–SP data and simulation quantifies the energy scale and energy scale bias for low energy electrons in a surface level LArTPC detector; this measurement can provide valuable input to studies of supernova burst neutrinos in LArTPC detectors.

Chapter 2 provides a theoretical overview of neutrinos within the standard model. Interactions, oscillations, and production will be discussed summarising the current knowledge in the field, as well as open questions which will be studied in ongoing and upcoming experiments. The role of neutrinos in supernova bursts and the detection of such neutrinos in a LArTPC detector will be discussed in more detail.

The ProtoDUNE–SP experiment is described in chapter 3, including details of the beam line, detector, cosmic ray flux, and simulations. An overview of the LArTPC detection principle will be given with specific details of the ProtoDUNE–SP design. Some details of detector operations will be discussed, paying particular attention to the monitoring of the detector via the online data quality monitoring system.

Chapter 4 will cover details of electromagnetic energy loss in liquid argon. Electron and photon energy loss will be discussed as well as processes leading to electron-ion recombination. The impacts of these effects on electron reconstruction in liquid argon will be highlighted.

The main analysis of this thesis will be described in chapters 6 and 7. Details of a hit classification algorithm based on convolutional neural networks will be given and Michel electron reconstruction will be highlighted as an example use for the output of this algorithm. Michel electron production and energy loss in liquid argon will be discussed. This will be followed by details of the reconstruction strategy used in the Michel electron analysis. The reconstructed Michel electron spectrum will be

compared between data and simulation, and the energy resolution and energy scale bias for low energy electrons in the ProtoDUNE–SP detector will be estimated.

Chapter 8 will analyse the implications of the results of the Michel electron analysis for supernova neutrino physics in the DUNE experiment; the impacts of energy scale bias on these analyses will be investigated, and the possible performance of DUNE assuming the measured bias will be discussed.

A summary of the results presented in this thesis will be given in chapter 9 along with a discussion of the implications of these results for neutrino physics in LArTPC detectors.

2

Neutrino Physics

Contents

2.1	A Brief History of Neutrino Physics	6
2.2	Neutrinos in the Standard Model	12
2.3	Neutrino Oscillations	14
2.3.1	Neutrino Oscillations in Vacuum	15
2.3.2	Neutrino Oscillations in Matter	17
2.3.3	Current Knowledge and Open Questions	19
2.4	Neutrino Interactions	22
2.5	Supernova Neutrinos	26
2.5.1	Core-collapse Supernova Dynamics	27
2.5.2	SN1987A	29
2.5.3	Supernova Neutrino Prospects in DUNE	31

Despite being one of the most abundant particle in the universe, neutrinos are some of the most elusive; due to the fact that neutrinos can only interact via the weak interaction. The history of neutrino physics is therefore strongly connected to the discovery and study of weak interactions. Measurements by Chadwick in 1914 showed that the energy spectrum of electrons released in β -decays was continuous, this is in contrast to discrete spectra observed in α and γ decays, and seemingly violates conservation of energy under the assumption of a two-body final state which was expected at the time. In order to solve this problem, Pauli postulated that the continuous energy spectrum could be explained, if the energy

released in a β -decay could be shared with an additional neutral weakly interacting fermion, which Pauli named the neutron. Fermi later renamed Pauli's fermion to the neutrino after Chadwick discovered the neutron in 1932. Despite claims that neutrinos might never be detected, neutrinos have now been discovered and they have been found to have a number of interesting properties, which were not anticipated when neutrinos were first postulated.

This chapter will detail some of the history and theory of neutrino's and their interactions. Section 2.1 will give a brief historical overview of neutrino physics. Section 2.2 will introduce the theory of neutrinos in the Standard Model, followed by a discussion of neutrino oscillations in Section 2.3. Neutrino interactions will be discussed briefly in Section 2.4. Finally Section 2.5 will discuss the production and measurement of neutrinos from supernovae.

2.1 A Brief History of Neutrino Physics

The first attempt to incorporate the neutrino into a theoretical model came in 1934, when Fermi presented his theory of β -decay. In this theory the neutrino takes part in a four-point interaction with the other components of the β -decay interaction [10]. The incredible success of this theory in explaining the observed properties of β -decays provided strong evidence for the neutrinos existence, however, in 1934 after using Fermi's theory to predict the strength of neutrino interactions, H. Bethe and R. Peierls found that the interactions were so weak that they might never be observed, a prediction that held true for over 20 years [11].

The first breakthrough in experimental neutrino physics would come in 1956. F. Reines and C. Cowan were attempting to measure positrons produced in inverse β -decay interactions,

$$\bar{\nu}_e + p \rightarrow n + e^+. \quad (2.1)$$

A detector containing 1400 litres of liquid scintillator was used to measure the large flux of electron anti-neutrinos in the vicinity of the Savannah River nuclear reactor. They observed a large increase in the rate of positron events when the reactor

was on compared to when the reactor was switched off, the first experimental evidence for the existence of neutrinos [12].

The discovery of the electron neutrino opened the door to answer questions of neutrino flavour. As neutrinos are produced alongside a charged lepton it is natural to compare the properties of neutrinos with their partners in the weak interaction. At the time of the discovery of the neutrino there were two known charged leptons, the electron and the muon, and physicists asked whether the neutrinos produced alongside muons are different from those produced alongside electrons. In 1962, Lederman et al discovered the muon neutrino at Brookhaven National Laboratory; by creating a beam of muon-associated neutrinos from decaying pions, and observing the leptons produced in neutrino interactions after all other particles had been absorbed. They found that only muons were produced in the resulting neutrino interactions, and therefore the neutrinos produced were only ever associated with a muon, which shows that neutrinos are produced with a distinct flavour in weak interactions [13].

In 1973 the Gargamelle experiment at the European Organisation for Nuclear Research (CERN) released results on the measurement of neutrino interactions [14]. They observed a new type of interaction, neutral current (NC) interactions:

$$\nu_l + N \rightarrow \nu_l + X \quad (2.2)$$

which are characterised by the lack of an observable charged lepton in the final state. Unlike charged current (CC) interactions, which are mediated by the charged W boson, these NC interactions are mediated by the neutral Z⁰ boson.

With the discovery of the tau-lepton in 1977, it was expected that there should be an associated tau neutrino, however, it wouldn't be detected until 2001 by the DONUT experiment [15]. In the experiment, tau neutrinos were produced from the decay of charmed mesons produced in collisions between protons and a stationary target. The neutrino interactions were detected in emulsion detectors, where the unique geometry of the interaction, in which a short tau

track is produced at the vertex followed by a long muon track, allowed them to be distinguished from other decays.

While additional neutrino species are possible, data from measurements of the Z boson line–shape at LEP in 1992 restricts the number of active light neutrino species to be three [16]. An active light neutrino is any neutrino with $m_\nu < \frac{m_Z}{2}$ that can interact with the Z boson, such that the decay $Z \rightarrow \nu\bar{\nu}$ is possible.

Alongside the discovery of three different types of neutrino, there were interesting results when observing neutrinos produced in the Sun. The flux of neutrinos from the Sun at the earth surface had been predicted with Bachall’s Standard Solar Model (SSM). However, in 1968 when Davis et al measured the flux in the Homestake experiment they found a deficit with respect to the prediction of the SSM [17, 18], the so called solar neutrino problem. In the Homestake experiment electron neutrinos where being measured via there inverse beta decay interactions with the chlorine in the target,



The neutrino interaction rate was measured by counting the number of argon atoms in the chlorine tank by capturing them on helium gas which was periodically bubbled through the chamber.

In addition to the solar neutrino problem, a similar deficit was observed in 1988 for muon neutrinos produced during cosmic ray showers. The Kamiokande experiment was able to measure both electron and muon neutrino interactions via the Cerenkov radiation produced by the charged leptons in water. Their data was consistent with the expected rate of electron neutrinos from the atmosphere, however, a deficit of muon neutrinos was observed [19].

The next generation of the Kamiokande experiment, Super–Kamiokande, aimed to understand the observed deficit of atmospheric muon neutrinos with a larger water Cerenkov detector capable of resolving the angular distribution of atmospheric neutrino interactions. Super–Kamiokande consists of a cylindrical vessel containing 50 kt of ultra pure water, surrounded by an array of around 13,000 photomultiplier

tubes to detect the Cerenkov light. Electron and muon neutrinos can be distinguished based on the pattern of Cerenkov light that is left in the detector; muons leave clear Cerenkov rings in the detector due to their higher mass, while electrons, which can scatter and shower, tend to leave diffuse "fuzzy" rings on the wall of the detector. In 1998, Super-Kamiokande published measurements of the flux of atmospheric muon neutrinos as a function of azimuthal angle [20]. Since these neutrinos are created a short distance from the earth's surface, the incoming angle of the neutrino can be used to estimate the distance travelled by the neutrino before arriving at the detector; the down-going neutrinos have only travelled a short distance in the atmosphere ($\sim 10\text{km}$), while the up-going neutrinos have travelled through the entire earth to reach the detector ($\sim 13,000\text{km}$). Figure 2.1, shows the flux of neutrinos measured by Super Kamiokande as a function of L/E_ν ; the muon neutrino flux is consistent with the no oscillation prediction at small L/E_ν , however, for large L/E_ν a clear deficit is observed.

While it wouldn't pin down the exact cause of the solar neutrino problem, the Sudbury Neutrino Observatory (SNO) was able to provide unique insight into the observed solar neutrino fluxes in 2002. Unlike other water Cerenkov detectors, SNO was filled with heavy water, D_2O , instead of its lighter isotope. The use of heavy water gives rise to additional neutrino interactions which allowed the SNO experiment to distinguish between three different interaction modes: charged current (CC), neutral current (NC), and elastic scattering (ES). Each mode is sensitive to different parts of the solar neutrino flux, including some sensitivity to the muon neutrino and tau neutrino fluxes via the NC and ES interactions. Analysis of the data for each of the three unique interaction modes lead to a measurement of the flavour composition of the solar neutrino flux at earth, while also finding the overall neutrino flux at earth to be consistent with the SSM. Figure 2.2 shows the composition of the solar neutrino flux as measured in the SNO experiment [21], the flux prediction based on the measured rate of NC events is consistent with the predictions of the SSM. The composition of solar neutrinos measured in the SNO experiment is not a result of simple neutrino oscillations, it also depends on the effect of matter



Figure 2.1: Ratio of data to Monte Carlo for electron and muon neutrino fluxes measured by the Super Kamiokande experiment as a function of L/E_ν . The Monte Carlo prediction is based on the assumption of no oscillations. The muon neutrino flux is consistent with the no oscillation prediction at small L/E_ν , however, for large L/E_ν a clear deficit is observed. The best fit under the assumption of atmospheric ($\nu_\mu \rightarrow \nu_\tau$) oscillations is shown, the best fit parameters are $\Delta m^2 = 2.2 \times 10^{-3} \text{ eV}^2$, and $\sin^2 2\theta = 1$. [20].

on the neutrino propagation in the Sun via the Mikheyev–Smirnov–Wolfenstein (MSW) effect. However at the time a number of solutions were still possible: MSW conversion, decoherence, neutrino decay, and others [22].

An L/E_ν dependence in the neutrino flux would have to be measured in order for neutrino oscillations to be the unique solution to the problem. To make this measurement a much shorter neutrino baseline would be needed, and a detector with good energy resolution. In 2002 the Kamioka Liquid Scintillator Anti-neutrino Detector (KamLAND) experiment measured $\bar{\nu}_e$ oscillations from a number of nuclear reactors, which produce neutrinos at the MeV scale [23, 24]. Along with an overall deficit of neutrino events, they were able to use the high energy resolution of the KamLAND detector to measure an L/E_ν dependence of the $\bar{\nu}_e$ survival probability. Figure 2.3, shows the ratio of the observed neutrino flux with the

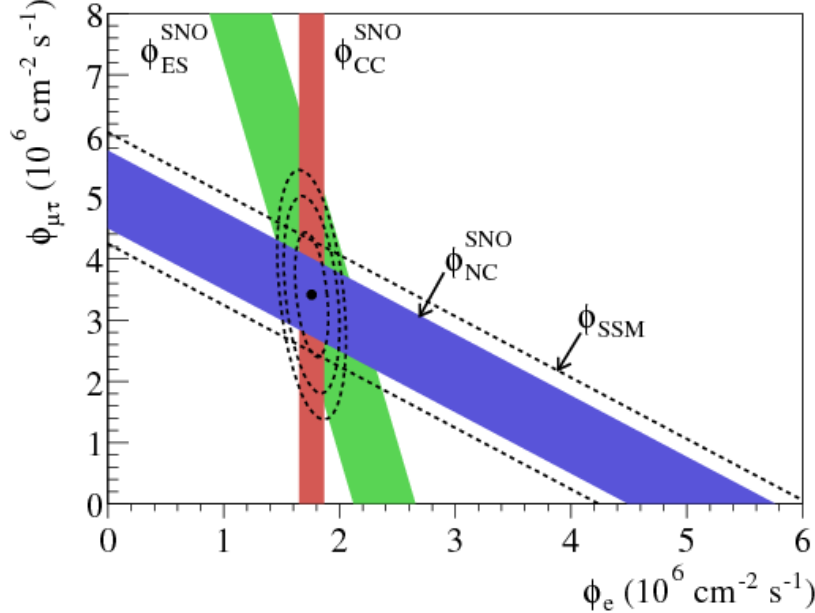


Figure 2.2: Solar neutrino flux composition as measured by the SNO experiment. The coloured bands represent the measured flux of charged current (CC), neutral current (NC), and elastic scattering (ES) events, including a $\pm 1\sigma$ spread. The central contours represent 68%, 95%, and 99% probability contours for the joint ϕ_e and $\phi_{\mu\tau}$ fit. The dashed lines represent the predicted flux of ${}^8\text{B}$ neutrinos based on the standard solar model [21].

no oscillation predicted flux as a function of L/E_ν , a clear dependence can be seen and this data was enough to prove that neutrino oscillations were the only solution to the solar neutrino problem.

Based on the results of the above experiments, it was assumed that electron and muon type neutrinos oscillate into tau type neutrinos, which then went undetected. The first evidence of tau neutrino production in oscillations wouldn't come until 2010, when the OPERA experiment measured a ν_τ candidate in a ν_μ beam. They used similar emulsion detectors to those used to discover the ν_τ in DONUT, and a muon neutrino beam on a 730 km baseline from CERN to Laboratori Nazionali del Gran Sasso (LNGS). By the end of the experiment a total of 10 candidate events have been observed, 6.1σ above the expected background [25, 26].

Since the discovery of neutrino oscillations, many more experiments have made measurements of oscillations and the majority of the parameters of the neutrino oscillation models have been constrained. Important results of these experiments for

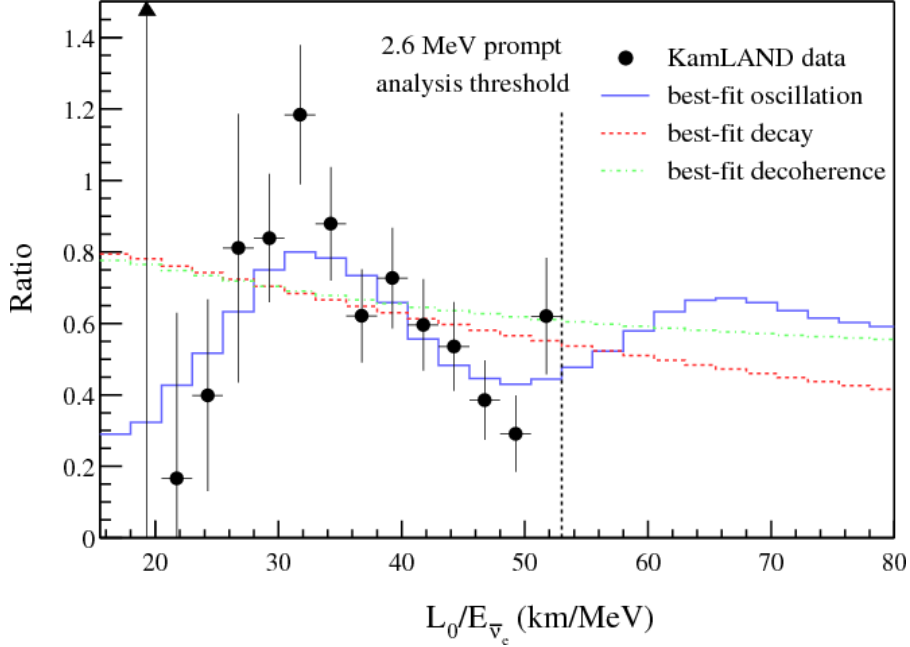


Figure 2.3: Ratio of observed neutrino flux to the predicted flux in the absence of neutrino oscillations in the KamLAND experiment as a function of L/E_ν . The data are fit with three different models: the red dashed line represents the best fit to a neutrino decay model, the green dashed line is for a decoherence model, and the solid blue line represents the best fit of the data to a neutrino oscillation model. The neutrino oscillation model, which has a different shape to the other two models, is found to give the best fit to the data [24].

constraining the parameters of the neutrino oscillation models will be highlighted in Section 2.3, along with a theoretical overview of neutrino oscillations.

2.2 Neutrinos in the Standard Model

In the standard model neutrinos form part of the left handed fermion doublets

$$\psi_i = \begin{pmatrix} \nu_i \\ l_i^- \end{pmatrix}, \quad (2.4)$$

where they are paired with a charged lepton of the same flavour in CC interactions, and i represents any of the three known generations of leptons. Their interactions with other particles in the standard model is determined by the electroweak (EW) theory, which is derived from the $SU(2) \times U(1)$ gauge group. The neutrino fields

enter into the SM Lagrangian in the CC and NC interactions:

$$\mathcal{L}^{CC} = -\frac{g_W}{\sqrt{2}} j_\alpha^{CC}(x) W^\alpha(x) + h.c. \quad (2.5)$$

$$\mathcal{L}^{NC} = -\frac{g_W}{\cos\theta_W} j_\alpha^{NC}(x) Z^\alpha(x) + h.c. \quad (2.6)$$

Here

$$j_\alpha^{CC}(x) = \sum_{\beta=e,\mu,\tau} \bar{\nu}_\beta(x) \gamma_\alpha \frac{1}{2} (1 - \gamma_5) l_\beta(x) \quad (2.7)$$

is the leptonic charged-current and

$$j_\alpha^{NC}(x) = \frac{1}{2} \sum_{\beta=e,\mu,\tau} \bar{\nu}_\beta(x) \gamma_\alpha \frac{1}{2} (1 - \gamma_5) \nu_\beta(x) \quad (2.8)$$

is the neutrino neutral-current, $W^\alpha(x)$ and $Z^\alpha(x)$ are the vector boson fields for the W^\pm and Z^0 bosons respectively, g_W is the electroweak coupling constant, and θ_W is the Weinberg angle.

Mass is included in the standard model through the Dirac mass term in the Lagrangian

$$\begin{aligned} \mathcal{L}^D &= m_D \bar{\psi} \psi \\ &= m_D \overline{(\psi_L + \psi_R)} (\psi_L + \psi_R) \\ &= m_D (\bar{\psi}_L \psi_R + \bar{\psi}_R \psi_L) \end{aligned} \quad (2.9)$$

where L and R represent the left and right handed components of the field. The lack of right handed neutrino states therefore means neutrinos are assumed to be massless in the standard model. For massive neutrinos to exist the standard model, right handed neutrino fields need to be introduced. In addition, it is still not known whether neutrinos are Dirac or Majorana particles, meaning that additional Majorana mass terms are possible. A more general neutrino mass term including both Dirac and Majorana components is

$$\mathcal{L}^{D+M} = \begin{pmatrix} \bar{\nu}_L & \bar{\nu}_R \end{pmatrix} \begin{pmatrix} m_L & m_D \\ m_D & m_R \end{pmatrix} \begin{pmatrix} \nu_L \\ \nu_R \end{pmatrix}. \quad (2.10)$$

2.3 Neutrino Oscillations

Neutrino oscillations are a result of quantum mechanical interference between different massive neutrino eigenstates. The mass eigenstates are produced and measured coherently because the energy and momenta of the neutrino states are not measured with enough precision to distinguish the mass eigenstate of the neutrino.

Neutrinos are produced in a state of definite flavour, $\alpha = e, \mu, \tau$, in charged current (CC) and neutral current (NC) weak interactions,

$$W^+ \rightarrow l_\alpha^+ \nu_\alpha, \quad W^- \rightarrow l_\alpha^- \nu_\alpha, \quad Z \rightarrow \nu_\alpha \bar{\nu}_\alpha. \quad (2.11)$$

The CC processes are used in neutrino oscillation experiments because they give information about the initial flavour state of the neutrinos. These processes are governed by the Lagrangian of the CC leptonic interactions, as in Equation 2.5.

Neutrino flavour states, ν_α , can be represented as a superposition of neutrino mass eigenstates in any case where the energy and momentum of the neutrino is not known with enough precision to determine the neutrino mass. The basis transformation takes the form

$$\nu_\alpha = \sum_k U_{\alpha k}^* \nu_k, \quad (2.12)$$

where ν_k are the neutrino mass eigenstates, and U is a unitary mixing matrix.

The representation of neutrino flavour states as a superposition of mass eigenstates gives rise to the phenomenon of neutrino oscillations. Consider a neutrino produced in a CC weak interaction with flavour α . This neutrino flavour state is described by equation 2.12, where U is a unitary mixing matrix called the PMNS (Pontecorvo, Maki, Nakagawa, and Sakata) matrix. For three flavour mixing the PMNS matrix takes the form:

$$U = \begin{pmatrix} U_{e1} & U_{e2} & U_{e3} \\ U_{\mu 1} & U_{\mu 2} & U_{\mu 3} \\ U_{\tau 1} & U_{\tau 2} & U_{\tau 3} \end{pmatrix}. \quad (2.13)$$

2.3.1 Neutrino Oscillations in Vacuum

In a vacuum, the neutrino mass states are eigenstates of the free particle Hamiltonian

$$\mathcal{H} |\nu_k\rangle = E_k |\nu_k\rangle, \quad (2.14)$$

with energy

$$E_k = \sqrt{\mathbf{p}^2 + m_k^2}. \quad (2.15)$$

So the solutions to the time dependent Schrodinger equation are plane waves

$$|\nu_k(t)\rangle = e^{-iE_k t} |\nu_k\rangle. \quad (2.16)$$

The time evolution of the initial flavour state is:

$$|\nu_\alpha(t)\rangle = \sum_k U_{\alpha k}^* e^{-iE_k t} |\nu_k\rangle. \quad (2.17)$$

The mass states can be written in terms of the flavour states by inverting Equation 2.12:

$$|\nu_k\rangle = \sum_\alpha U_{\alpha k} |\nu_\alpha\rangle. \quad (2.18)$$

Here, we have used the fact that the states form an orthonormal basis, $\langle\nu_\alpha|\nu_\beta\rangle = \delta_{\alpha\beta}$, and that the transformation matrix is unitary, $UU^\dagger = \mathbf{1}$.

Substituting Equation 2.18 into the time evolution of the flavour state, Equation 2.17, gives:

$$|\nu_\alpha(t)\rangle = \sum_{\beta=e,\mu,\tau} \left(\sum_k U_{\alpha k}^* e^{-iE_k t} U_{\beta k} \right) |\nu_\beta\rangle \quad (2.19)$$

So as the initial flavour state evolves with time, it becomes a superposition of different flavour states; this process is known as neutrino oscillation. The probability of finding the initial neutrino in flavour state ν_β as a function of time is:

$$P_{\nu_\alpha \rightarrow \nu_\beta}(t) = |\langle\nu_\beta|\nu_\alpha(t)\rangle|^2 \quad (2.20)$$

$$= \sum_{kj} U_{\alpha k}^* U_{\beta k} U_{\alpha j} U_{\beta j}^* e^{-i(E_k - E_j)t}. \quad (2.21)$$

All neutrino oscillation experiments to date operate in a regime where $E \gg m$, in this regime the relativistic energy relation for neutrinos can be expanded as $E_k \simeq E + \frac{m_k^2}{2E}$, where $E = |p|$. Hence,

$$E_k - E_j \simeq \frac{m_k^2 - m_j^2}{2E} = \frac{\Delta m_{kj}^2}{2E}. \quad (2.22)$$

In addition, neutrino oscillation experiments do not measure the neutrino propagation time t . Instead, they measure the propagation distance, L , also known as the baseline. In the ultra-relativistic limit we can approximate $t \simeq L$ in natural units. As a result, Equation 2.20 can be approximated as:

$$P_{\nu_\alpha \rightarrow \nu_\beta}(t) = \sum_{kj} U_{\alpha k}^* U_{\beta k} U_{\alpha j} U_{\beta j}^* e^{-i \frac{\Delta m_{kj}^2 L}{2E}}. \quad (2.23)$$

Splitting the sum into its real and imaginary parts emphasises the possibility of CP-violation in neutrino oscillations. CP-violation occurs if the imaginary component of the matrix product is non-zero.

$$\begin{aligned} P_{\nu_\alpha \rightarrow \nu_\beta}(t) &= \delta_{\alpha\beta} - 4 \sum_{j>k} \text{Re}(U_{\alpha k}^* U_{\beta k} U_{\alpha j} U_{\beta j}^*) \sin^2\left(\frac{\Delta m_{kj}^2 L}{2E}\right) \\ &\quad \pm 2 \sum_{j>k} \text{Im}(U_{\alpha k}^* U_{\beta k} U_{\alpha j} U_{\beta j}^*) \sin^2\left(\frac{\Delta m_{kj}^2 L}{2E}\right). \end{aligned} \quad (2.24)$$

The third term here is responsible for CP violation in neutrino oscillations, the positive case corresponds to neutrinos and the negative case is for anti-neutrinos.

The probability of oscillation is therefore dependent on properties determined by nature, in the form of PMNS matrix elements and mass squared differences, and those which can be chosen by experiments, the distance travelled, L , and the neutrino energy, E . In a vacuum, the oscillation probability is only dependent on the magnitude of the squared mass difference between the neutrino mass eigenstates. It gives no information about the absolute masses of the neutrino eigenstates or their ordering. The question of the absolute neutrino masses cannot be answered in neutrino oscillation experiments. To get access to the absolute masses other experiments are required, e.g. direct mass measurements with tritium beta decay experiments such as KATRIN [27]. Neutrino oscillation experiments can give insight on the ordering of the neutrino masses, but to understand how the oscillations of neutrinos in matter must be considered.

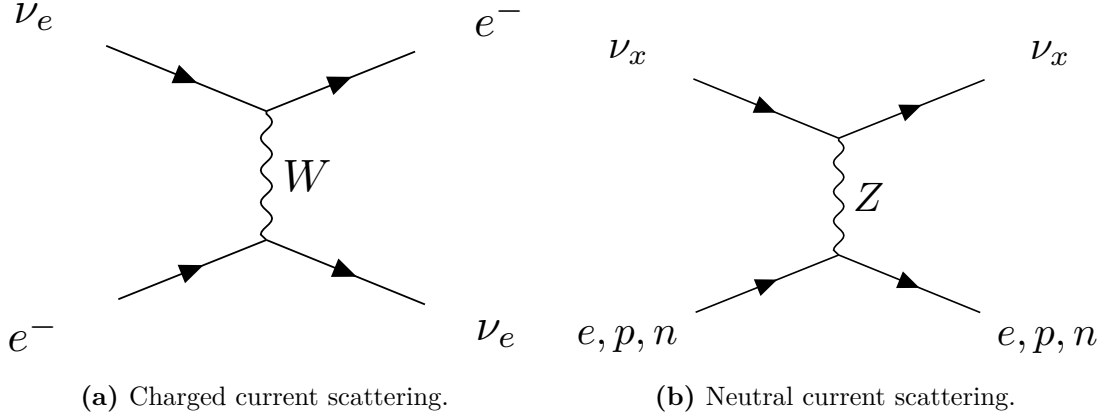


Figure 2.4: Feynman diagrams for neutrino scattering in matter.

2.3.2 Neutrino Oscillations in Matter

In real neutrino oscillation experiments, neutrinos travel through matter, whether it be the matter in a star or the earth's crust. Neutrinos propagating in matter are subject to an additional potential due to the interaction of the neutrinos with the electrons and nucleons in the medium. This interaction can significantly modify the flavour of the beam relative to oscillations in vacuum.

In matter neutrinos can scatter off particles by interacting with either the charged-current or neutral-current interactions as shown in Figure 2.4. These interactions give rise to additional effective potentials which the neutrinos experience while they are travelling,

$$V_{CC} = \sqrt{2}G_F N_e, \quad (2.25)$$

$$V_{NC}^f = \sqrt{2}G_F N_f g_V^f, \quad (2.26)$$

where G_F is the Fermi weak coupling constant, N_e and N_f are the number densities of electrons and other fermions respectively, and g_V^f is the vector coupling constant for a given fermion f .

Neutral-current scattering is independent of neutrino flavour meaning that the additional potential does not affect oscillations. However, the charged current potential is only present for ν_e , and therefore it will impact the mass eigenstates by different amounts depending on their relative ν_e component.



Figure 2.5: The two possible neutrino mass orderings. Left: normal ordering. Right: inverted ordering. Figure from [30].

A full description of the effects of matter on neutrino oscillations is beyond the scope of this thesis, although it is discussed at length in other sources such as [28]. For the purposes of this thesis it is sufficient to note that the propagation of neutrinos in matter changes the oscillations probabilities, and this must be taken into account by oscillation experiments.

One implication of the effects of matter on oscillations is that it introduces sensitivity to sign of the mass splittings [28], allowing experiments to determine the relative ordering of the neutrino masses. By considering the pattern of neutrino oscillations in the sun it is possible to determine that $\Delta m_{21}^2 > 0$ [29]. The sign of the remaining mass splitting, Δm_{32}^2 , remains unknown which leaves two possibilities for the ordering of neutrino masses. Normal ordering (NO), in which $m_3 > m_2 > m_1$, and inverted ordering (IO), where $m_1 > m_2 > m_3$, which are depicted in Figure 2.5.

2.3.3 Current Knowledge and Open Questions

At the time of writing the most widely accepted model of neutrino oscillations involves three neutrino mass eigenstates. In this model, the PMNS matrix is often parametrised in terms of three mixing angles θ_{12} , θ_{13} , and θ_{23} and three CP-violating phases δ_{CP} , α_1 , and α_2 :

$$U = \underbrace{\begin{pmatrix} c_{12} & s_{12} & 0 \\ -s_{12} & c_{12} & 0 \\ 0 & 0 & 1 \end{pmatrix}}_{\text{Solar}} \underbrace{\begin{pmatrix} c_{13} & 0 & s_{13}e^{-i\delta_{CP}} \\ 0 & 1 & 0 \\ -s_{13}e^{i\delta_{CP}} & 0 & c_{13} \end{pmatrix}}_{\text{Cross-mixing}} \underbrace{\begin{pmatrix} 1 & 0 & 0 \\ 0 & c_{23} & s_{23} \\ 0 & -s_{23} & c_{23} \end{pmatrix}}_{\text{Atmospheric}} \underbrace{\begin{pmatrix} e^{i\frac{\alpha_1}{2}} & 0 & 0 \\ 0 & e^{i\frac{\alpha_2}{2}} & 0 \\ 0 & 0 & 1 \end{pmatrix}}_{\text{Majorana}}. \quad (2.27)$$

Expressing the mixing matrix like this factorises the matrix into its components, which are responsible for oscillations in different regimes. The first component contains only θ_{12} which is dominant in Solar neutrino oscillations. The third component dominates in the mixing of atmospheric neutrinos, and is a function of θ_{23} . The final, element which is significant for neutrino oscillations is the second component, known as the cross-mixing matrix or reactor matrix. This component depends on the final mixing angle, θ_{13} and on one of the CP-violating phases, δ_{CP} . If δ_{CP} is non-zero then U will have complex components in off diagonal elements, leading to different probabilities for CP flipped oscillations, $P(\nu_\alpha \rightarrow \nu_\beta) \neq P(\bar{\nu}_\alpha \rightarrow \bar{\nu}_\beta)$. Discovery of this effect, which is known as CP-violation, is one of the major goals of the next generation of neutrino oscillation experiments.

The final matrix in the factorised version of the PMNS matrix is called the Majorana component. The CP-violating phases in this matrix cancel in the oscillation probability, and so they can't be measured in neutrino oscillation experiments. In fact, they only lead to physical effects if neutrinos are Majorana particles (i.e. if they are their own antiparticle). Other experiments are required to determine if neutrinos are Majorana particles, for example, neutrinoless double beta decay experiments such as CUORE[31], NEXT[32], and SNO+[33]. The

question of the nature of neutrinos has implications on neutrino mass generation, as mentioned in Equation 2.10.

A large number of neutrino oscillation measurements have now been made by solar, reactor, atmospheric, and accelerator neutrino experiments. When combined the results of these experiments give us our best estimates of neutrino oscillation parameters. The current combined results, from the 2018 Review of Particle Physics by the Particle Data Group [29], along with the major contributing experiments for each measurement are summarised below.

θ_{12}

The constraints on the solar mixing angle θ_{12} are dominated by a combination of data from solar neutrino experiments (e.g. SNO [21] and Super Kamiokande [34]) with data from the KamLAND experiment [24]. The current constraint,

$$\sin^2(\theta_{12}) = 0.297^{+0.017}_{-0.016}, \quad (2.28)$$

comes from a three neutrino fit to the solar and KamLAND data [35].

Δm_{21}^2

The best measurement of Δm_{21}^2 comes from the same combined fit to the solar neutrino and KamLAND data [35]. The measured value is

$$\Delta m_{21}^2 = (7.37^{+0.17}_{-0.16}) \times 10^{-5} \text{ eV}^2. \quad (2.29)$$

θ_{23} and Δm_{32}^2

There is a strong correlation between θ_{23} and Δm_{32}^2 and therefore their measurements are usually presented as a two-dimensional contour. Figure 2.6 shows a comparison of the world leading contours for $\sin^2(\theta_{23}) - \Delta m_{32}^2$, with the tightest error bands coming from long baseline accelerator experiments such as T2K, MINOS, and NO ν A [36–38]. The results are dependent on the neutrino mass ordering, based on a global three neutrino oscillation analysis [35],

$$\begin{aligned} |\Delta m_{32}^2| &= (2.46^{+0.04}_{-0.04}) \times 10^{-3} \text{ eV}^2 \quad (\text{NO}) \\ &= (2.50^{+0.05}_{-0.04}) \times 10^{-3} \text{ eV}^2 \quad (\text{IO}), \end{aligned} \quad (2.30)$$



Figure 2.6: The 90% confidence region contours for $\sin^2(\theta_{23}) - \Delta m_{32}^2$ from a number of the leading neutrino oscillation experiments [36–38]. The best fit point for the NO ν A experiment is shown as a black dot. [38]

and

$$\begin{aligned} \sin^2(\theta_{23}) &= 0.437 {}^{+0.033}_{-0.020} \quad (\text{NO}) \\ &= 0.569 {}^{+0.028}_{-0.051} \quad (\text{IO}). \end{aligned} \quad (2.31)$$

θ_{13}

Reactor neutrino experiments such as Daya Bay [39], Double Chooz [40], and RENO [41] have made the most precise measurements of θ_{13} . A three neutrino global fit to the reactor data gives [35]

$$\sin^2 \theta_{13} = (2.15 \pm 0.07) \times 10^{-2}. \quad (2.32)$$

δ_{CP}

While there are no accurate measurements of δ_{CP} there are some hints that it may be non-zero from long baseline accelerator neutrino experiments T2K and NO ν A. These limits are based on joint fits to four data samples: electron neutrino

appearance, electron anti-neutrino appearance, muon neutrino disappearance, and muon anti-neutrino disappearance.

The T2K experiment's joint fit shows an excess of electron neutrino events and a deficit of anti-electron neutrino events when compared to the predictions for $\delta_{CP} = 0$. This results in a preference for negative values of δ_{CP} with a 3σ confidence interval of $[-3.41, -0.03]$ in the case of normal neutrino mass ordering. The results of the T2K fit are shown in Figure 2.7 [42].

The NO ν A experiment has also performed joint fits to neutrino and anti-neutrino oscillation data, the results of the fit are shown in Fig. 2.8. As with T2K the normal mass ordering is preferred, however for NO ν A the full range of δ_{CP} is covered at 3σ highlighting the need for further study of CP-violation in neutrino oscillations [38].

Neutrino oscillations are currently the only measured effect that is not explained in the SM, and their observation proves that neutrinos are massive. However, the absolute mass of neutrinos is still unknown. The question of absolute neutrino mass, is one of a number of open questions in neutrino physics. At the time of writing, the main open questions in neutrino physics are:

- What are the absolute masses of the neutrinos?
- What is the mass ordering of the neutrino mass eigenstates?
- Is there CP violation in the neutrino sector?
- Are neutrinos Dirac ($\nu \neq \bar{\nu}$) or Majorana ($\nu = \bar{\nu}$) particles?
- Are there any sterile neutrino states?

2.4 Neutrino Interactions

To perform a neutrino oscillation experiment the composition of the beam needs to be measured, and the change in beam composition as a function of energy and distance travelled is analysed. In practice, this relies on measuring neutrino events and categorising them by flavour in order to compare the measurement

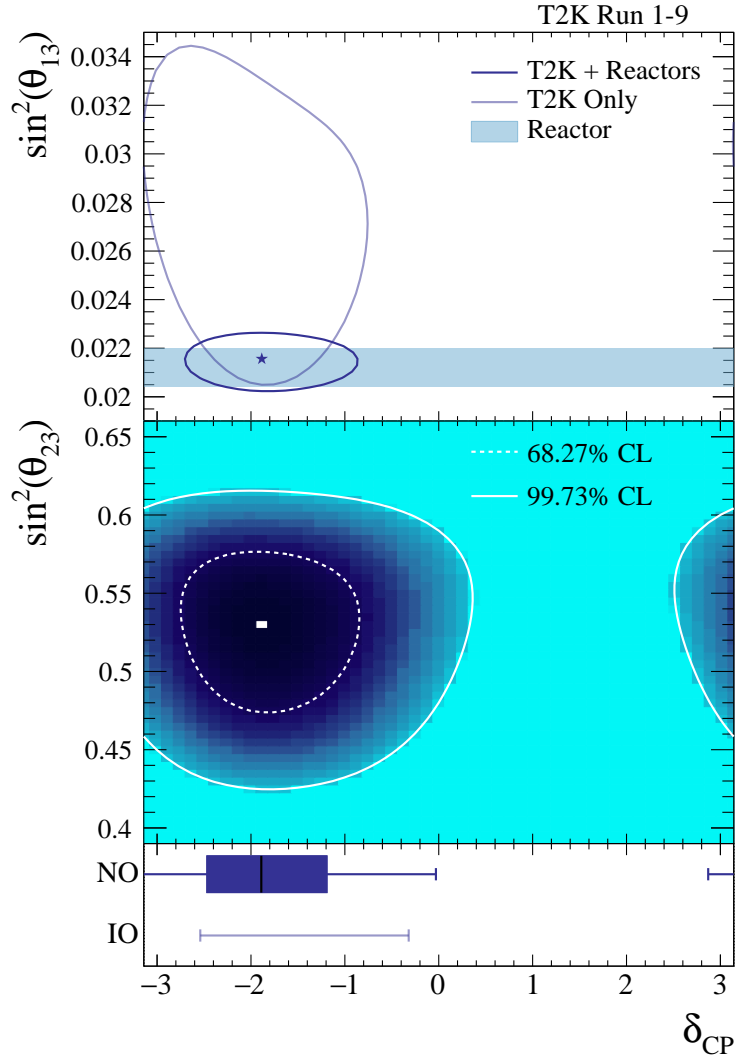


Figure 2.7: Confidence intervals for δ_{CP} from the T2K experiment [42]. Top: 68.27% confidence level contours for δ_{CP} versus $\sin^2 \theta_{13}$ under the assumption of normal ordering. Middle : Confidence intervals at the 68.27% and 99.73% confidence level for δ_{CP} versus $\sin^2 \theta_{23}$ from a fit to T2K and reactor data under the assumption of normal ordering. Bottom: Confidence intervals for δ_{CP} from a fit to T2K and reactor data for both the normal and inverted orderings. The vertical line in the shaded box shows the best-fit value of δ_{CP} , the shaded box shows the 68.27% confidence interval, and the error bar shows the 99.73% confidence interval.

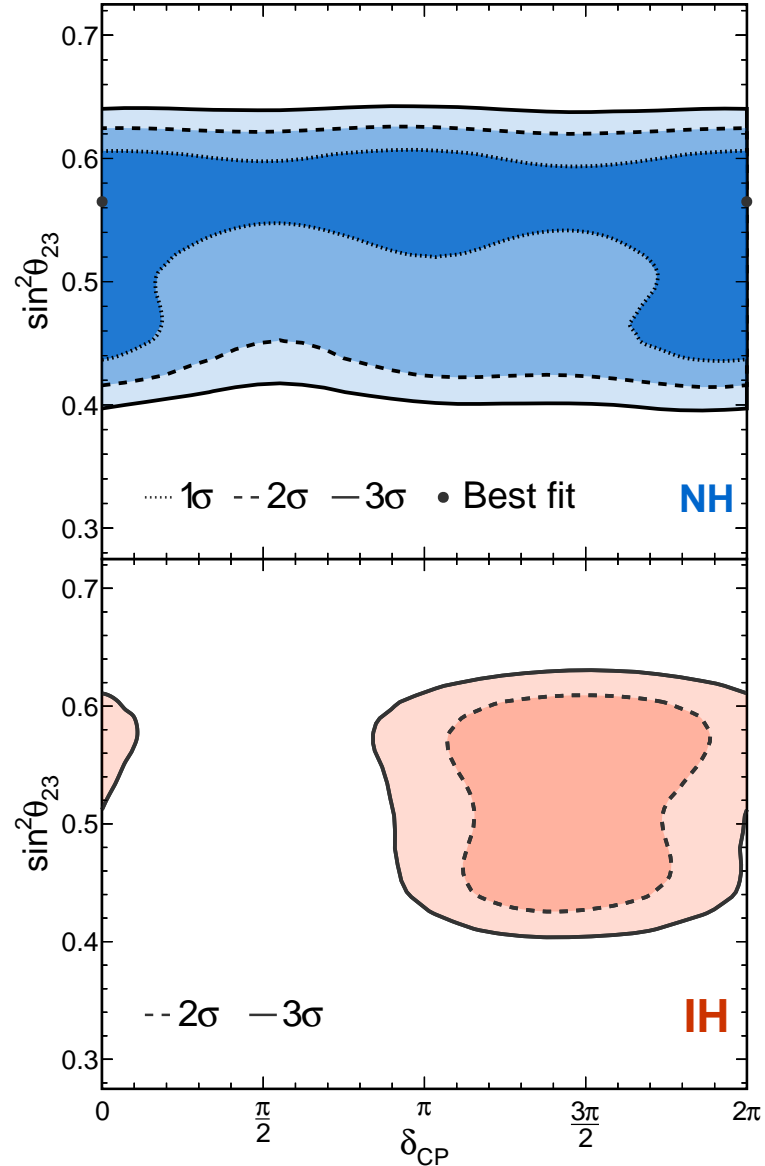


Figure 2.8: Confidence intervals for δ_{CP} from the NO ν A experiment [38].

Top: Confidence interval for δ_{CP} versus $\sin^2 \theta_{23}$ under the assumption of normal ordering.
Bottom: Confidence interval for δ_{CP} versus $\sin^2 \theta_{23}$ under the assumption of inverted ordering.

to prediction. However, because we only see the neutrinos that interact, we are actually seeing the results of a convolution of the neutrino beam composition with the neutrino interaction cross section. Therefore, it is important to understand neutrino interaction cross sections to make accurate oscillation predictions.

Broadly speaking there are two major types of neutrino interactions: charged–current (CC) and neutral–current (NC). CC interactions are usually used in oscillation experiments because they are the only type of interaction which allows the initial flavour of the neutrino to be determined. Some NC interactions, e.g. scattering from an electron, produce high energy leptons in the detector and, therefore, form an irreducible background which must be modelled as part of the experiments simulation.

The types of charged–current interactions available are further split into three main categories.

Quasi–elastic (QE)

A neutrino elastically scatters off an individual nucleon. Depending on the energy transfer, the nucleon may be liberated from the nucleus.

Resonance (RES)

A neutrino excites the target nucleon into a resonance, which then decays resulting in the possibility of mesons in the final state.

Deep Inelastic Scattering (DIS)

The neutrino has enough energy to resolve the individual quarks within the target nucleon, liberating the quark and resulting in a hadronic final state.

The cross sections for these processes vary as a function of neutrino energy, and they are each dominant in different energy regimes. Predictions and measurements of the charged–current cross section for ν_μ are shown in Figure 2.9, the three main components of the cross section are shown and the energy range relevant for DUNE is highlighted [43]. Within the energy range of the DUNE beam all



Figure 2.9: Muon neutrino cross section as a function of energy. Original figure from [43].

three of the major neutrino cross section components have a region in which they dominate, this means that understanding each of these cross sections is crucial for any neutrino oscillation measurement in DUNE.

The array of interaction modes available in DUNE means that there are many particles which can be produced in the final state; understanding the composition of the final state is essential to the neutrino oscillation analysis. Part of this thesis, Chapter 6, looks at the identification of charge deposits in a liquid argon TPC. The results provide input in the analysis of ProtoDUNE-SP data, and the methods used could be adapted and developed for application in the identification of neutrino interaction modes in DUNE.

2.5 Supernova Neutrinos

Supernovae are extremely violent explosions, which are undergone by certain types of stars at the end of their life. These explosions can emit on the order of 10^{46}

Joule of energy, and in certain cases, known as core-collapse supernovae, about 99% of this energy is carried away by neutrinos. Measurements of these neutrinos can provide insight into the mechanism involved in supernova bursts, as well as the study of neutrino masses [28].

2.5.1 Core-collapse Supernova Dynamics

Core-collapse supernovae occur in stars with masses of around 10–60 solar masses. These stars will have undergone all stages of nuclear fusion during their life, but since iron is the most tightly bond nucleus there is no fuel left to burn after it has been produced. At this stage the iron core of the star, which has a mass of around 1 solar mass, begins to collapse as the pressure produced by nuclear fusion is no longer enough to counter the force of gravity.

During the collapse of the core electron neutrinos are produced through electron capture on both nuclei and free protons.



At first, the mean free path of these neutrinos is much longer than the size of the core and the neutrinos leave the core carrying away their energy. This phase of the collapse is known as the infall phase, it lasts on the order of 10ms and releases neutrinos with energies of around 12–16 MeV.

Once the density of the core increases beyond around $3 \times 10^{11} \text{ g cm}^{-3}$ neutrinos become trapped in the core, as the cross section for coherent scattering becomes large enough to prevent neutrinos from passing through the core. Neutrinos are still being produced by capture processes at this point, but they are unable to leave the core.

The core-collapse comes to a sudden halt about 1 second after it began when the density of the inner core reaches that of nuclear matter. At this stage, the core settles into equilibrium as a proto-neutron star while a shock-wave caused by this sudden halt propagates out through the layers of the star. Behind the shock, neutrino production is accelerated as nuclei are dissociated and the free

protons capture electrons. Neutrinos begin to build-up behind the opaque shock. A few milliseconds after the bounce, the shock reaches a region of low enough density and becomes transparent, releasing the build-up of neutrinos in just a few milliseconds, this is known as the neutronisation burst.

One aspect of supernova dynamics which is still under debate is the so-called revival of the shock. As the shock dissipates through nucleon dissociation and neutrino emission it becomes weakened and eventually stalls around 100 ms after the initial bounce. At this time, known as the accretion phase, matter falls onto the collapsed core. If the shock cannot be revived a supernova will not occur. It is thought that neutrino flux produced in the proto-neutron star is able to revive the shock but the precise mechanics of this revival are still under debate. Studies have shown that the impact of spherically asymmetries might play an important role in allowing the burst to take place [44].

After the neutronisation burst the main remaining source of neutrino production comes from the proto-neutron star. Neutrinos of all flavours are produced in the core at a temperature of around 40 MeV. The release of neutrinos at this stage, known as the neutrino cooling phase, is significantly slower than that of the neutronisation burst and can last tens of seconds. During this phase, much like photons within a star, the neutrinos are mostly contained within the opaque environment of the proto-neutron star. They can only escape if they travel far enough from the core to a region where the opacity is sufficiently low. This region is called the neutrinosphere, it is different for neutrinos of different flavours, and for neutrinos and anti-neutrinos. The difference in the neutrinosphere for each flavour result in different energy distributions for each neutrino type, owing to the relative temperature of the star at the radius of the neutrinosphere,

$$\langle E_{\nu_e} \rangle \approx 10 \text{ MeV} \quad (2.35)$$

$$\langle E_{\bar{\nu}_e} \rangle \approx 15 \text{ MeV} \quad (2.36)$$

$$\langle E_{\nu_x} \rangle \approx 20 \text{ MeV} \quad (2.37)$$

where $\nu_x \in [\nu_\mu, \bar{\nu}_\mu, \nu_\tau, \bar{\nu}_\tau]$.

2.5.2 SN1987A

The first, and only, experimental observation of neutrinos from a supernova burst occurred in 1987. A small number of low-energy neutrino events were detected in coincidence with a supernova burst from the Large Magellanic Cloud, referred to as SN1987A. Three neutrino detectors reported an excess of low energy events in coincidence with the supernova: Kamiokande-II, IMB, and Baksan. These events are primarily produced by two types of interaction, inverse beta decay (IBD),

$$n + \nu_e \rightarrow p + e^+, \quad (2.38)$$

and elastic scattering,

$$\nu_e + e^- \rightarrow \nu_e + e^-. \quad (2.39)$$

For supernova neutrinos, the inverse beta decay cross section is significantly higher than that of elastic scattering, therefore, most events are likely to be due to inverse beta decay.

2.5.2.1 Kamiokande-II

Kamiokande-II was a water Cerenkov detector containing 2.1 kt of water. A significant increase in the rate of electron events with respect to background was observed in a 10 second window which is coincident with SN1987A [45]. Around 12 events were observed, their time sequence and amplitudes are shown in Figure 2.10. Unfortunately, due to an inaccurate detector clock, the absolute time of these events is only accurate to about one minute and therefore a time coincidence check with the other neutrino observations cannot be made.

2.5.2.2 IMB

IMB was another water Cerenkov detector, with a fiducial mass of 3.3 kt. They observed eight neutrino candidate events with energies in the range of 20–40 MeV within a six second window, the background rate was estimated to be around 2 events per day [46].



Figure 2.10: Measured supernova neutrino events from SN1987A in Kamiokande-II. Figure from [45].

2.5.2.3 Baksan

Unlike Kamiokande-II and IMB, the Baksan detector was a segmented liquid scintillator detector with a total mass of around 330 tons, however only a limited fiducial mass of around 200 tons was used for the supernova neutrino measurements. No excess above background could be observed by Baksan in isolation, however, when assisted by input from Kamiokande-II and IMB, a cluster of 5 events within a 10s window was observed which coincided with the measurements from IMB [47].

Since SN1987A significant progress has been made for both experimental and theoretical aspects of neutrino physics. Progress has been made in modelling supernova explosions, and the impact of neutrino oscillations on the supernova environment have been considered [48]. The current and next generation of neutrino experiments expect to measure thousands of neutrino events for a galactic supernova instead of tens. The flux of neutrinos at earth has three components ν_e , $\bar{\nu}_e$, and ν_x , the predicted energy spectra of each component is shown in Figure 2.11. Measuring the spectrum and time structure of a supernova neutrino burst could provide insights into the dynamics of supernovae, as well as neutrino physics.

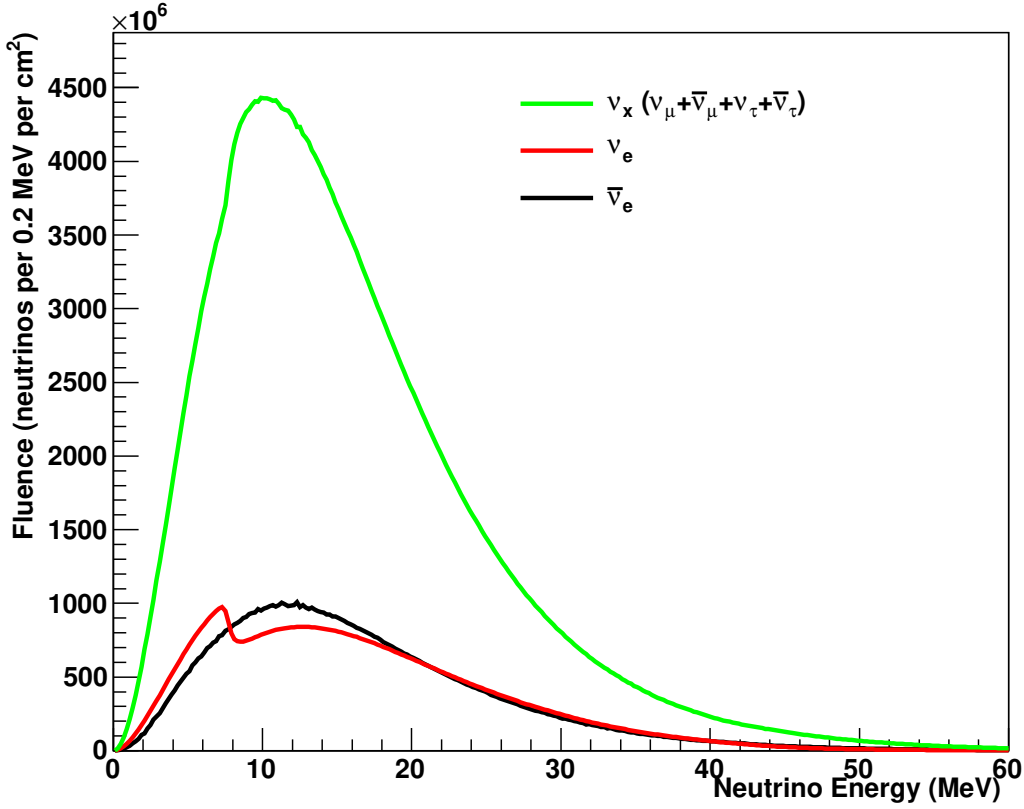


Figure 2.11: Supernova neutrino energy spectrum. Figure from [3].

2.5.3 Supernova Neutrino Prospects in DUNE

The current world leading supernova neutrino detector is Super-Kamiokande which expects to measure around 8000 events for a supernova at 10 kpc [49]. As with Kamiokande-II, these events would primarily be produced via inverse beta decay interactions on the protons within the water. As such Super-Kamiokande is mostly sensitive to the $\bar{\nu}_e$ component of the supernova neutrino flux. This is common amongst all water Cerenkov and scintillator based detectors, and therefore the majority of the current landscape of supernova neutrino detectors. The large charged-current cross section for ν_e on argon therefore makes DUNE a highly complementary detector to the other major supernova neutrino detectors, and DUNE offers a unique sensitivity to the neutronisation burst, which is primarily made up of ν_e .



Figure 2.12: Supernova neutrino cross sections in liquid argon. Figure from [50].

2.5.3.1 Supernova Neutrino Interactions in Liquid Argon

Liquid argon should bring a strong sensitivity to the ν_e component of a supernova neutrino burst, via the charged-current absorption of ν_e on ^{40}Ar ,

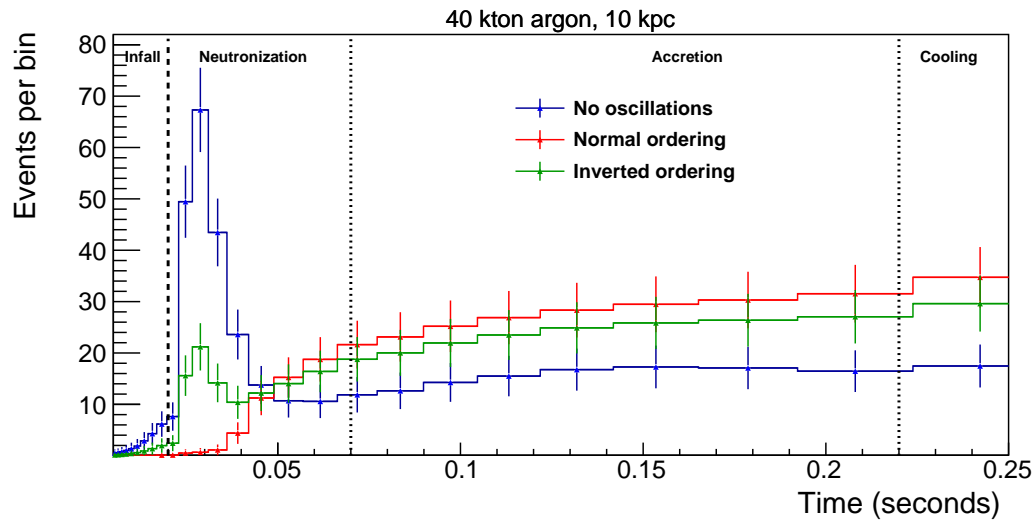


This interaction leaves an e^- and an excited K in the final state. In addition there are charged-current $\bar{\nu}_e$ interactions with argon, and elastic scattering interactions with electrons, which are available to neutrinos of all flavours. The dominant cross sections in liquid argon as a function of energy are shown in Figure 2.12 [50].

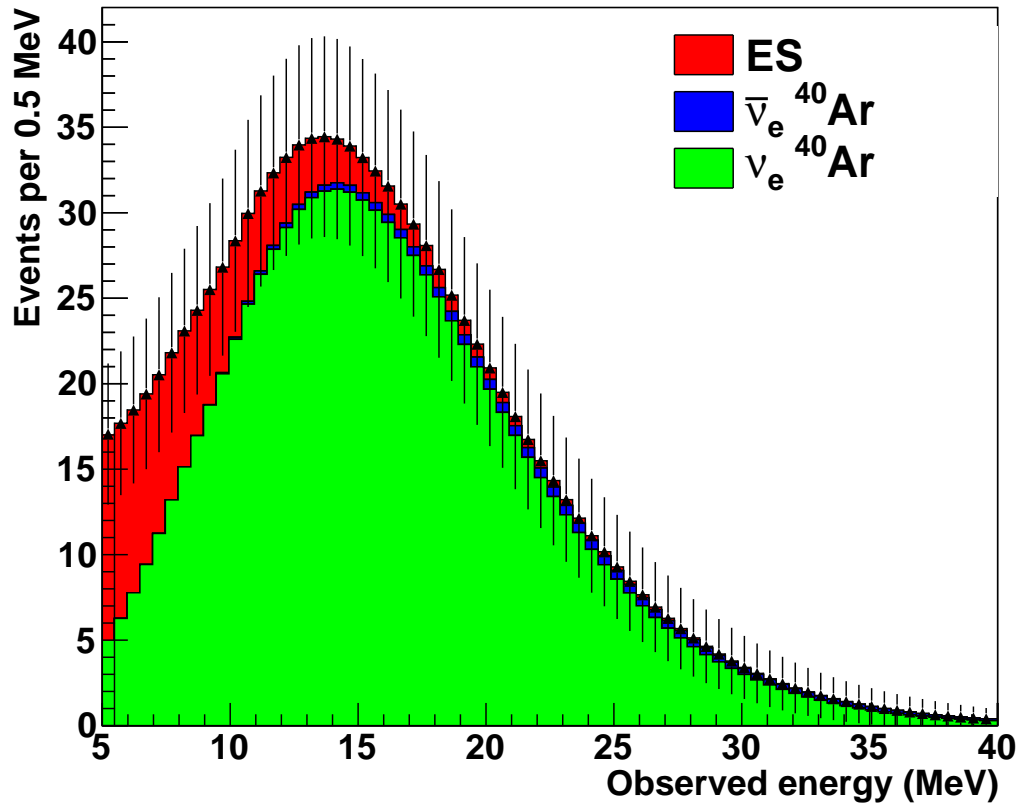
2.5.3.2 Supernova Neutrino Events in DUNE

For a 10 kpc supernova DUNE expects to observe roughly 3000 neutrino events, over a period of around 10 seconds. In DUNE this will show up as a sudden increase in the rate of low-energy electron events in the detector. Figure 2.13 shows the predicted time structure and energy spectrum for a simulated supernova event in DUNE [50]. The details of the rate and energy of these events as a function of time can hold potential insights into both neutrino physics and the dynamics of supernova bursts.

Detecting and reconstructing tens of MeV electrons is necessary to study supernova neutrinos, as can be seen from the observed energy spectrum for supernova neutrinos in Figure 2.13. There are significant challenges involved in this measurement from the detection of low energy activity, as well as the impacts of the ionisation geometry of tens of MeV on reconstruction. Effectively reconstructing electrons in the tens of MeV range is essential to improving our understanding of supernova neutrinos in DUNE. This is one of the subjects of this thesis, and is discussed in chapter 7 using the case of Michel electrons in ProtoDUNE-SP to benchmark the performance of low energy electron reconstruction in liquid argon time projection chambers.



(a) Observed event rate. Figure from [50].



(b) Observed energy. Figure from [51].

Figure 2.13: Supernova neutrinos predictions for a 10kpc supernova in DUNE.

3

The ProtoDUNE–SP Experiment

Contents

3.1	ProtoDUNE–SP in the Context of DUNE	36
3.1.1	Liquid Argon Time Projection Chambers	37
3.2	The ProtoDUNE–SP Detector	40
3.2.1	The Liquid Argon TPC	40
3.2.2	The Photon Detection System	42
3.3	The H4 beamline	44
3.4	The Cosmic Ray Tagger	46
3.5	The Data Acquisition System	47
3.6	Simulation	49
3.7	Reconstruction	50
3.8	ProtoDUNE–SP Online Monitoring System	56
3.8.1	Data Processing	57
3.8.2	Monitoring Web Interface	63

ProtoDUNE–SP is one of two prototypes for the DUNE far detector modules that has been operating at the Neutrino Platform at CERN since the summer of 2018. The experiment collected data from a charged particle beam for approximately 3 months before Long Shutdown 2 of the Large Hadron Collider. Since then a programme of cosmic ray data collection has been ongoing.

This chapter will outline the technical details of the ProtoDUNE–SP experiment. Section 3.1 will outline the role of ProtoDUNE–SP in the context of the DUNE experiment. This will be followed by a discussion of the main elements of the



Figure 3.1: The Deep Underground Neutrino Experiment. Figure from [52].

ProtoDUNE-SP detector systems and the H4 beamline, in Sections 3.2 and 3.3 respectively. The tagging of cosmic-ray muons for calibration is done by the Cosmic Ray Tagger which will be discussed in Section 3.4. Sections 3.6 and 3.7 will then discuss the simulation and reconstruction of ProtoDUNE-SP data. Finally Section 3.8 will cover details of the online monitoring system in ProtoDUNE-SP; as the primary developer and expert on the ProtoDUNE-SP online monitoring system during my time at CERN, the development and maintenance of this system represent a significant body of work over 12 months.

3.1 ProtoDUNE-SP in the Context of DUNE

The DUNE experiment will be a next generation neutrino physics and nucleon decay experiment consisting of three principal components; an intense broad band neutrino beam and precise near detector complex based at the Fermilab National Accelerator Laboratory near Chicago, and a far detector at Sanford Underground Research Facility in South Dakota, approximately 1300 km away from the neutrino source, as in Figure 3.1. The DUNE experiment identifies three primary scientific goals [50]:

- Perform a comprehensive programme of neutrino oscillation measurements including measurements of δ_{CP} , neutrino mass ordering, and θ_{23} .
- Search for proton decay in several decay modes.

- Measure neutrinos from a core-collapse supernova, if one occurs within our galaxy during the lifetime of the experiment.

In addition, the experiment hopes to fulfill a significant programme of secondary science goals:

- Other accelerator based neutrino physics, such as non-standard interactions, sterile neutrinos, and CPT violation.
- Measurements of neutrino properties using atmospheric neutrinos.
- Dark matter searches in both the near and far detectors.
- A programme of neutrino interaction physics studies in the DUNE near detector.

To achieve these goals DUNE has opted to base the near and far detector designs on the liquid argon time projection chamber (LArTPC) technology. The DUNE far detector will eventually consist of four LArTPC detectors each with 10 kt of active liquid argon mass. This technology will have never before been used on this scale, and therefore, there has been a significant programme of LArTPC research and development ongoing to validate and characterise the performance of the technology for DUNE.

3.1.1 Liquid Argon Time Projection Chambers

A LArTPC consists of a large volume of highly-purified liquid argon subject to an electric field. Charged particles traversing the liquid argon produce two primary energy depositions, a trail of ionisation electrons along their path, and prompt ultra-violet scintillation photons. After creation the ionisation electrons drift in the electric field toward the charge readout plane where they induce electrical signals. Liquid argon is transparent to its own scintillation light and therefore the scintillation photons can travel through the argon to be collected in a photon detection system. The LArTPC detection principal is illustrated in Figure 3.2.



Figure 3.2: LArTPC detection principle. Figure from [53].

The Role of Light in LArTPCs

The ionisation signals in a LArTPC are slow, it takes electrons milliseconds to travel from the cathode plane to the anode plane. In contrast, scintillation photons only take on the order of nanoseconds to reach the closest anode plane. This scintillation light plays an important role in the accurate 3D reconstruction of interactions in the LArTPC, it can be used to determine the time of an interaction to within a few nanoseconds.

In a LArTPC interactions play out much quicker than the detector is able to record them; as such each event actually integrates over a large number of interactions within the readout window. The true time, t_0 , of the interactions in the event cannot be reconstructed from the ionisation signals alone; by utilising the much faster scintillation signals the time of interactions can be calculated with much higher precision. This data can be combined with the arrival time of

drifting electrons to reconstruct the true drift distance, without an accurate t_0 the reconstructed drift distance will be too long.

The details of the charge readout and photon detection systems are specific to each detector, but broadly speaking LArTPC detectors can be split into two main categories: single-phase and dual-phase. In a single-phase detector the drifting ionisation electrons remain in the liquid argon and the signals are typically read out on three anode wire planes, although pixel readout systems have also been developed [TODO]. A dual-phase LArTPC contains an additional region of gaseous argon in which a high electric field, known as the extraction field, is applied to extract the ionisation from the liquid into the gas before it is amplified and collected on a pair of anode wire planes [52].

ProtoDUNE-SP is one of two large scale prototypes for the DUNE far detector modules, which focusses on the single-phase LArTPC technology. The DUNE far detector modules feature a modular design in which each module is built up of a number of identical components, ProtoDUNE-SP was designed to prototype the design of many of these components at a 1:1 scale, including the anode planes, cathode plane, and photon detectors. The ProtoDUNE-SP experiment has four primary goals, as outlined in the Technical Design Report [54]:

- Prototype the production and installation procedures for the single-phase far detector design.
- Validate the design from the perspective of basic detector performance; this can be achieved with cosmic-ray data.
- Accumulate large samples of test-beam data to understand/calibrate the response of the detector to different particle species.
- Demonstrate the long-term operational stability of the detector as part of the risk mitigation program ahead of the construction of the first 10 kt far detector module.

As such, ProtoDUNE-SP represents a significant milestone in the development of the far detector for the DUNE experiment. Its successful operation, both in a test beam and with cosmic rays, provides valuable data with which to understand reconstruction and analysis of the data that will be collected by the DUNE far detector.

3.2 The ProtoDUNE-SP Detector

The ProtoDUNE-SP detector is located at the Neutrino Platform at CERN along the H4 beamline. It is a single-phase LArTPC detector with a total liquid argon mass of 0.77 kt, making it the largest monolithic single-phase liquid argon TPC to be built to date. The TPC comprises the following major components, which are illustrated in Figure 3.3:

- A cathode plane constructed of modular Cathode Plane Assemblies (CPA).
- Two anode planes constructed of modular Anode Plane Assemblies (APA).
- A photon detection system (PDS) which is integrated into the APAs.
- A field cage (FC), beam plug, and high voltage systems (HV).
- Readout electronics and Data Acquisition System (DAQ).

The detector components are designed to be an almost exact replica of the final single-phase far detector modules, but the detector has an overall scaling factor of approximately 1 : 20 in terms of total liquid argon mass [54].

3.2.1 The Liquid Argon TPC

The ProtoDUNE-SP TPC has an active volume of 6 m (height) \times 7.2 m (width, drift direction) \times 7 m (length, approximate beam direction). The cathode plane at the center of the active width is flanked by two anode planes which define two 3.6 m drift volumes. The field cage around these two drift volumes helps to ensure a uniform electric field within the drift region.

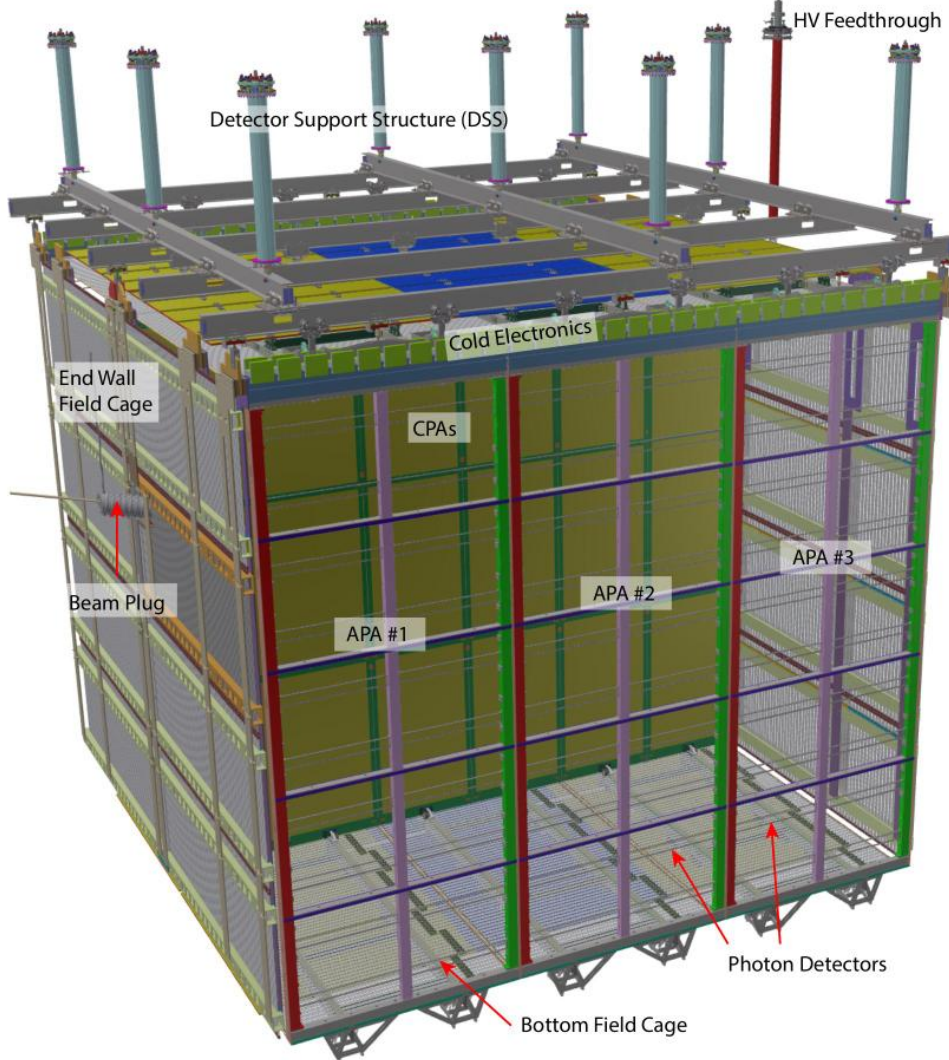


Figure 3.3: The main components of the ProtoDUNE-SP TPC. Figure from [54].

Each anode plane is modularly constructed from three APAs which have dimensions 6 m (height) \times 2.3 m (width). The APA frame holds three sets of parallel wires on the inward and outward facing sides, these are oriented at different angles to enable 3D reconstruction. The outer two sets of wires are induction wires, these are biased such that they are electrically transparent to the drifting ionisation. Ionisation passing the induction wires causes an induced bi-polar signal. The third set of wires are known as collection wires, these wires are not biased. When drifting ionisation approaches the collection wires it is absorbed producing a uni-polar signal. In ProtoDUNE-SP each set of induction wires contains 800 wires at a 4.67 mm spacing, and each set of collection wires contains 480 wires at a 4.79 mm spacing.

The wire planes from each APA are read out by electronics boards (FEMB) mounted on the APA frame; the FEMBs are submerged in the liquid argon and therefore also referred to as cold electronics (CE). A total of 2560 electronics channels are used to read out the data from each APA, with each readout window corresponding to 3 ms, which is 6000 time samples. The CE amplify, shape, and digitise the signals from the wires before transmitting them outside the TPC to the Warm Interface Boards (WIB). The WIBs collate the data from the CE boards and pass the data onto the Data Acquisition System (DAQ).

The cathode plane in ProtoDUNE-SP consists of an array of 18 CPA modules, 2 m (height) \times 1.2 m (width). The cathode plane is held at -180 kV to provide a 500 V/cm drift field in each of the drift volumes. The field cage surrounding the drift regions ensures that the electric field is uniform across the detector volume by providing the necessary electrical boundary conditions.

One area in which the design of ProtoDUNE-SP differs from the far detector is the inclusion of the beam plug. This is necessary to minimize interactions between the charged particle test beam and the cryostat before the beam enters the active region of the detector. A cylindrical beam plug, containing nitrogen gas, penetrates from the cryostat wall into the field cage at location of the incoming test beam.

3.2.2 The Photon Detection System

The Photon Detection System (PDS) in ProtoDUNE-SP is integrated into the APAs. Ten photon detector modules are embedded in each APA frame between the layers of wires on either side of the APA, as shown in Figure 3.3. Three types of photon detector module were tested in ProtoDUNE-SP, two very similar module designs based on coupling silicon photomultipliers to wavelength shifting bars, and a third novel design known as the ARAPUCA light trap. The operating principles of the two designs are illustrated in Figure 3.4.

The majority of the photon detector modules in ProtoDUNE-SP consist of wavelength shifting bars coupled to silicon photomultipliers (SiPM). Tetraphenylbutadiene (TPB) is used to shift the wavelength of the light from ultra-violet to blue



Figure 3.4: The operating principal of the photon detector modules in ProtoDUNE-SP. Figure (a) from [54]. Figure (b) from [55]

before the light is transmitted down the waveguide to the SiPMs. The main difference between the two nominal designs is in the wavelength of transmission within the waveguide; in one case the wavelength is transmitted at the blue wavelength produced by the TPB, in the other case the blue light from the TPB is first absorbed in the waveguide which then produces green light which is transmitted down the waveguide.

A small number of the photon detector modules in ProtoDUNE-SP feature a novel design known as an ARAPUCA light trap. In this design the photons are trapped in a small box through a sequence of wavelength shifting and optical filtering, significantly increasing the photon detection efficiency [56]. An ARAPUCA light trap consists of a box which is coated with a highly reflective surface, on one side of the box is the filtering window, and on the other a SiPM. Incoming ultra-violet photons are shifted to the blue spectrum before passing through a dichroic filter which has a tunable wavelength cut-off at which it transitions from being transparent to reflective. After passing through the filter the photons are shifted again, this time from blue to green, such that if they get back to the filter it is reflective. As such green photons can be trapped within the ARAPUCA until they come into contact with the SiPM, providing increased photon detection efficiency. Each ARAPUCA photon detector module in ProtoDUNE-SP features an array of

these traps arranged in a line across the width of an APA. 12 ARAPUCA light traps make up an ARAPUCA module, these are constructed from 16 so called cells, which are $5\text{ cm} \times 5\text{ cm} \times 1\text{ cm}$ boxes. Half of the light traps are made of one cell and the others being made of two cells joined together. Regardless of the number of cells, each ARAPUCA trap is read out by a single SiPM, making for 12 SiPMs per ARAPUCA module.

Unlike with the TPC electronics, there are no front-end electronics in the LAr volume for the PDS, the unamplified analogue signals are transmitted out of the cryostat before processing and digitisation. The light guide based photon detector module have 12 SiPMs which are read out in threes such that each module corresponds to 4 readout channels. The ARAPUCA modules are read out by one channel per SiPM, resulting in 12 channels per ARAPUCA module. The readout channels from each APA are processed by four so called SiPM Signal Processors (SSP), which are mounted on the top of the cryostat. After processing in the SSPs, the PDS data is passed onto the DAQ along with the TPC data.

3.3 The H4 beamline

The ProtoDUNE-SP experiment is located at the end of the H4 beamline at CERN, the location of the beamline with respect to the detector is illustrated in Figure 3.7. The beam has a mixture of particle types including hadrons, muons, and electrons, with momenta in the range 0.3–7 GeV. The momenta and composition of the beam can be varied, and several runs were taken across a range of particle compositions and beam momenta.

The H4 beamline is a tertiary beamline, which is produced when a secondary beam from the T2 primary target interacts with a secondary target. Particles from the secondary target are selected based on momentum and charge before travelling down the H4 beamline to ProtoDUNE-SP. A schematic of the beamline instrumentation (BI) and magnets in the H4 beamline is given in Figure 3.5.

By combining momentum measurements from the profile monitors with time of flight (TOF) and Cerenkov measurements the beam momentum and composition

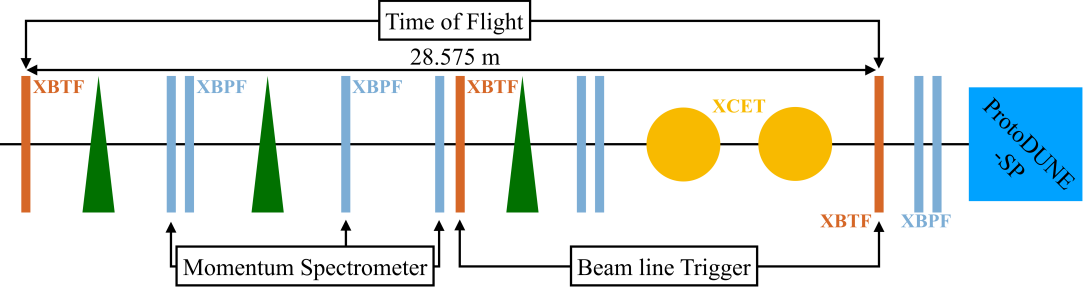


Figure 3.5: Schematic of the H4 beamline magnets and instrumentation. Figure from [57].

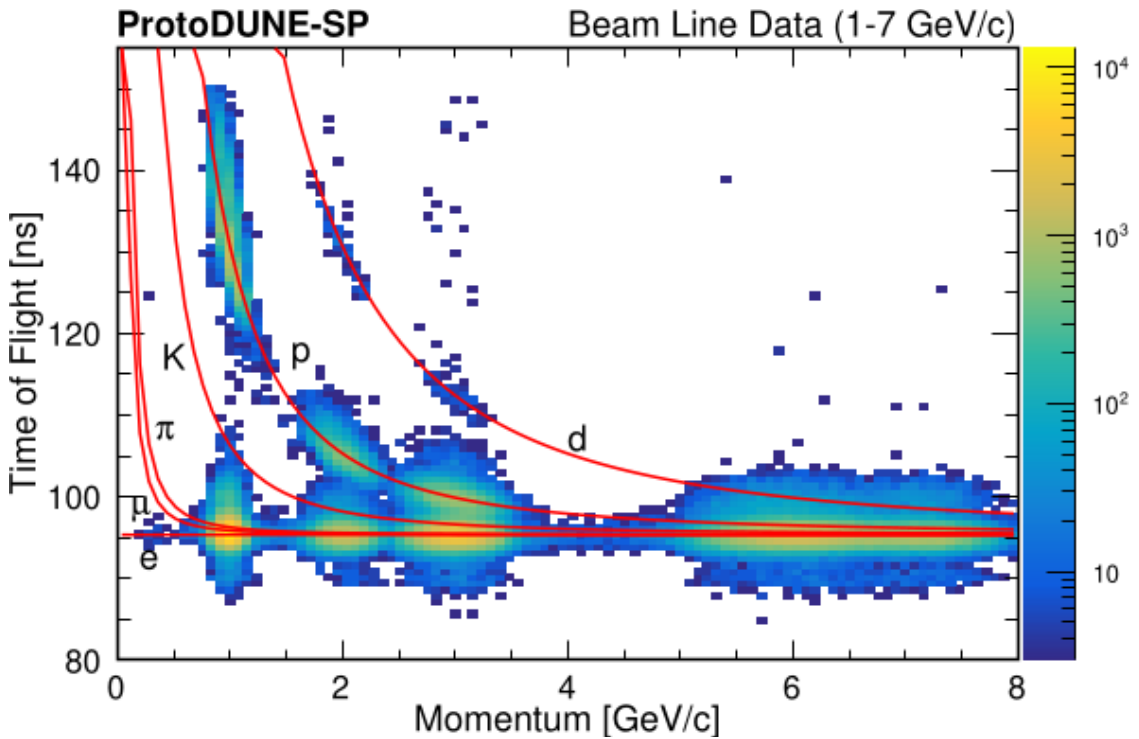


Figure 3.6: Time of flight vs momentum distributions from the H4 beamline instrumentation. Figure from [57]

can be measured. The predicted and measured distribution of TOF vs momentum for data from a number of runs at different momenta is shown in Figure 3.6. This information is used to trigger the detector during beam running, and is sent to the central trigger board for distribution to the detector components.

During the beam running period, a number of runs were taken with differing beam compositions and momenta. A summary of the collected beam data, as well as predictions of the particle composition from beamline simulations, is given

Momentum (GeV/c)	Recorded Triggers (10^3)	Expected Triggers (10^3)	Expected Pions (10^3)	Expected Protons (10^3)	Expected Electrons (10^3)	Expected Kaons (10^3)
0.3	269	242	0	0	242	0
0.5	340	299	1.5	1.5	296	0
1	1089	1064	382	420	262	0
2	728	639	333	128	173	5
3	568	519	284	107	113	15
6	702	689	394	70	197	28
7	477	472	299	51	98	24
All	4173	3924	1693.5	777.5	1381	72

Table 3.1: Summary of beam triggers in ProtoDUNE-SP. Data from [TODO].

in Table 3.1.

3.4 The Cosmic Ray Tagger

As a surface level detector with no overburden ProtoDUNE-SP measures a significant rate, on the order of 20 kHz, of cosmic ray muons, corresponding to an average of 60 muons per 3 ms readout window. These muons provide a useful source of calibration data in the form of long tracks and stopping muons. The Cosmic Ray Tagger (CRT) in ProtoDUNE-SP was installed on the upstream and downstream faces of the TPC to trigger the detector for cosmic-ray muons which travel parallel to the anode plane. In addition the CRT, can provide accurate timing information for any tracks which can be matched between the TPC and CRT.

The CRT consists of four parts, two upstream assemblies and two downstream assemblies, the locations of the CRT assemblies is illustrated in Figure 3.7. Each CRT assembly is constructed from overlapping scintillation counters, which cover an area 6.8 m high and 3.65 m wide. Scintillation strips of length 365 cm and width 5 cm are placed in perpendicular arrays to give two-dimensional reconstruction within each CRT assembly. By combining data from upstream and downstream CRT assemblies with a time coincidence requirement the trajectories of tracks can be reconstructed.



Figure 3.7: Location of the H4 beamline and cosmic ray taggers in relation to the ProtoDUNE-SP detector. Figures from [57].

3.5 The Data Acquisition System

Data from the TPC, PDS, and CRT in ProtoDUNE-SP are collated by the Data Acquisition system (DAQ). The DAQ distributes triggers, compresses and packages the data into events, and stores the data ready for future analysis. An overview of the ProtoDUNE-SP DAQ system is seen in Figure 3.8; there are four primary data flows in the system: TPC, PDS, CRT, and BI. Timing and triggering signals are distributed to the detector components by the timing board, which maintains a 50 MHz clock and receives $\sim 40\text{Hz}$ of triggers from the Central Trigger Board (CTB) based on data from the BI and CRT [54].

The ProtoDUNE-SP TPC contains a total of 15,360 wires spread across the six APAs, the wires are digitized at a rate of 2 MHz resulting in an overall data flow of around 480 Gb/s from the TPC electronics. An event in ProtoDUNE-SP corresponds to a continuous readout of the detector for 3 ms, resulting in 6000 samples from each wire; data is buffered such that the readout window can be opened 250 μs before the trigger time. Data from the TPC is received by



Figure 3.8: Outline of the data acquisition system in ProtoDUNE-SP. Figure from [54].

two systems, a system based on Reconfigurable Computing Elements (RCE) [58] handles the data from five APAs, while data from the sixth is received by a system based on Front-End Link Exchange (FELIX) cards, which have been developed by the ATLAS collaboration [59].

The software layer of the ProtoDUNE-SP DAQ is based on Fermilab's artdaq [60]. This component is primarily responsible for acquiring the data, packaging it, and storing it locally. Triggered events are queued and distributed to the board readers and event builders by the Data Flow Orchestrator. There are multiple board readers, which are each responsible for processing the data from specific hardware components. Details vary between specific board readers, but generally these processes are responsible for formatting the data from each component ready for aggregation. Data from the various detector components are aggregated by the event builders, which are responsible for assembling the completed events. After compression events have an average size of 60 MB. Artdaq is also responsible for the real-time monitoring of data quality via the online monitoring system, this system will be discussed in Section 3.8.

3.6 Simulation

Simulation and reconstruction of ProtoDUNE-SP data takes place in the LArSoft framework [61]. LArSoft is a software suite for simulating and reconstructing data collected by LArTPC detectors based on the art event framework from Fermilab [62]. LArSoft is under active use and development by a number of participating LArTPC based experiments, with each experiment making use of its core functionality as well as experiment specific code. The simulation and reconstruction of ProtoDUNE-SP data in the LArSoft framework will be discussed in Sections 3.6 and 3.7 of this chapter respectively.

Simulation in LArSoft is broken down into three sequential stages: generation, propagation, and detector simulation. The initial state particles are produced in the generation step, the propagation and interaction of these particles in the detector is simulated during the propagation step, finally the transport of energy depositions and simulation of detector effects are handled by the detector simulation phase.

As a surface based detector in a test beam, ProtoDUNE-SP is subject to three main sources of particles: beam particles, beam halo particles, and cosmic ray particles. The beam particle and beam halo flux in the vicinity of ProtoDUNE-SP was provided by simulations of the H4 beamline [63] based on two simulation frameworks, G4beamline [64] and FLUKA [65]. The cosmic ray flux in ProtoDUNE-SP is simulated using CORSIKA [66]. Finally, low energy radiological backgrounds in LAr are simulated, these include ^{39}Ar , ^{85}Kr , and ^{222}Rn .

After generation, the particles are allowed to propagate and interact in the detector geometry, including the cryostat, external systems, and experimental hall. This is simulated using GEANT4[67], which tracks particles in small steps; the step size, $300\mu\text{m}$, is chosen to be much smaller than the spatial resolution of the detector to allow for small-scale processes like showering to be accurately simulated.

Particles which propagate through the detector, during the propagation phase of the simulation, leave energy deposits in the form of ionisation electrons and scintillation photons. It takes 23.6 eV to ionise a single argon atom and around 19.5 eV to produce a single scintillation photon, as such a minimum-ionising particle

(MIP), which deposits around 2 MeV/cm in liquid argon, will produce tens of thousands of electrons and photons per cm.

The detector simulation is responsible for drifting the ionisation electrons towards the collection wires, propagating the simulated photons to the photon detectors, and simulating the response of the wires, SiPMs, and electronics to the signals. The sheer number of ionisation electrons and scintillation photons produced in a ProtoDUNE-SP event makes simulating the propagation of the full set of particles impractical and therefore LArSoft employs approximation techniques to predict the observed signals within a reasonable computation time. A number of detector effects are taken into account when simulating the electron drift: electron-ion recombination, transverse and longitudinal diffusion, electric field distortions, and electron capture on impurities.

When the ionisation and scintillation signals arrive at the active detector components, simulated waveforms are produced based on the induced signals produced in the detector components. These signals are converted into electrical signals by electronics simulation, which is completed in LArSoft. The electronics simulation includes simulation of electronics gain, noise, and analogue to digital conversion. The simulated waveforms produced by the ProtoDUNE-SP simulation are then compressed and stored ready for reconstruction.

3.7 Reconstruction

An event consists of a synchronised set of waveforms from all of the TPC channels, with each event corresponding to 3 ms or 6000 samples. The particle interactions within each event are reconstructed into objects like tracks and showers which can be used for physics analyses, this sections provides a brief summary of the steps involved in this reconstruction.

First, the TPC waveforms are passed through a set of filtering algorithms which are designed to reduce the noise on the waveforms, as well as to mitigate electronics effects such as sticky-codes and undershooting. An additional step known as a 2D deconvolution is applied to extract the original signal from the measured signal given

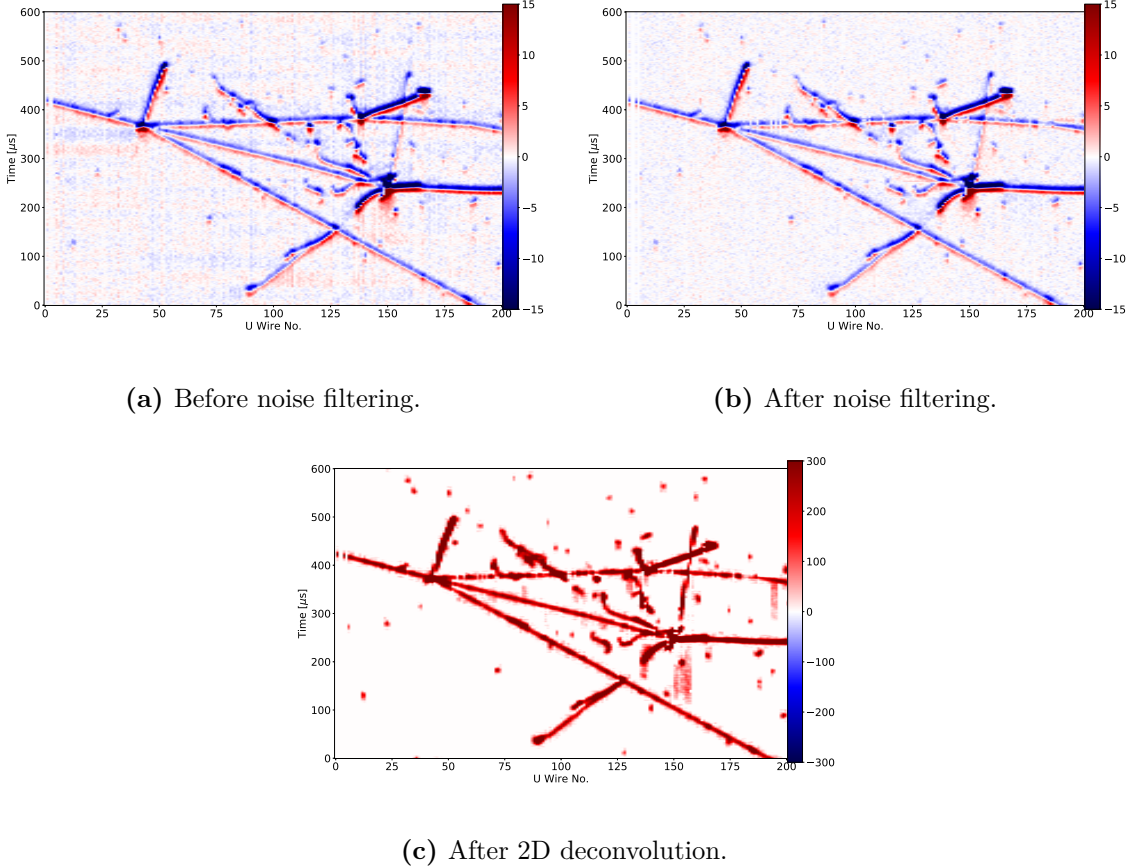


Figure 3.9: Example of noise filtering and 2D deconvolution in ProtoDUNE-SP data. Figures from [57].

a detector response function for the wire in question as well as neighboring wires, this method has been described in detail by the MicroBooNE collaboration [68]. An important side effect of the 2D deconvolution technique is that, after deconvolution, the bi-polar induction signals become unipolar, which simplifies hit tagging for these hits. An example of the noise filtering and 2D deconvolution techniques applied to a 7 GeV test beam event in ProtoDUNE-SP data is given in Figure 3.9.

Once the deconvoluted waveforms have been calculated, regions of interest (ROI) are defined, these are regions of high amplitude in which charge deposition is likely to have occurred. Reconstructed hits are found within each region of interest by fitting gaussian peaks to the peaks within the region; most hits consist of a single gaussian peak, however in busy regions of the detector multiple gaussian peaks may be used to fit a single pulse. Each reconstructed hit will have an associated peak time,

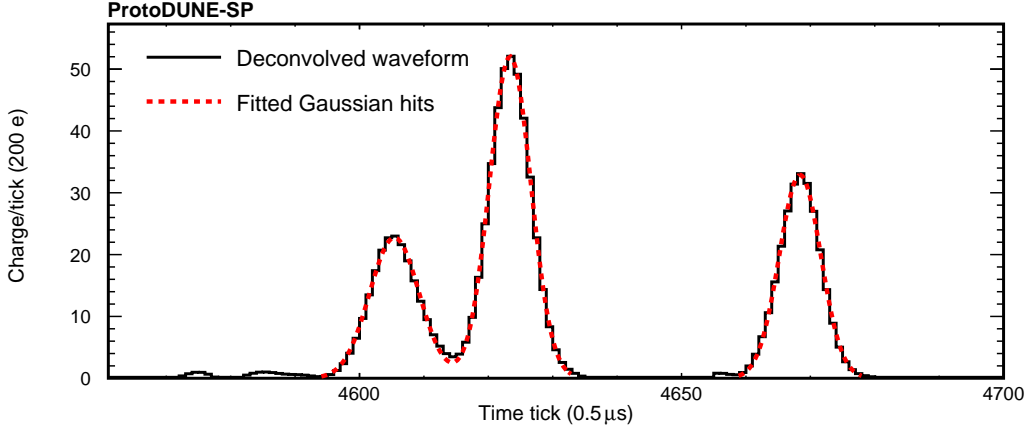


Figure 3.10: Reconstructed hits from ProtoDUNE-SP data. Figure from [57].

width, and integral, these objects form the basic input for the subsequent pattern recognition algorithms. An example of the reconstructed hits is shown in Figure 3.10.

Pandora [69] is the primary pattern recognition software used in ProtoDUNE-SP. It takes a multi-algorithm approach to reconstructing particle interactions in the detector, and has been successfully used by other LArTPC detectors, such as MicroBooNE [70]. Pandora handles the clustering of hits into 2D clusters, the matching of 2D clusters into 3D clusters, as well as the reconstruction of 3D objects like tracks and showers. Ultimately Pandora returns a tree of reconstructed Particle Flow Particles (PFParticles), each corresponding to a distinct track or shower, and connected through parent-daughter relationships, which define the particle flow in the interaction. Pandora reconstruction proceeds in two stages: a cosmic pass and a beam pass.

First the cosmic pass reconstructs the event with algorithms designed to reconstruct track-like particles. Track stitching algorithms can be used to predict the true interaction time for tracks during this stage. Any track which crosses either a CPA or APA will produce track segments on either side of the boundary, these segments point in the same direction but will have been displaced from each other in the drift direction based on the arrival time of the corresponding particle. The t_0 for that track is equal to half the time shift required to realign the two segments into a continuous track, a visual representation of this algorithm

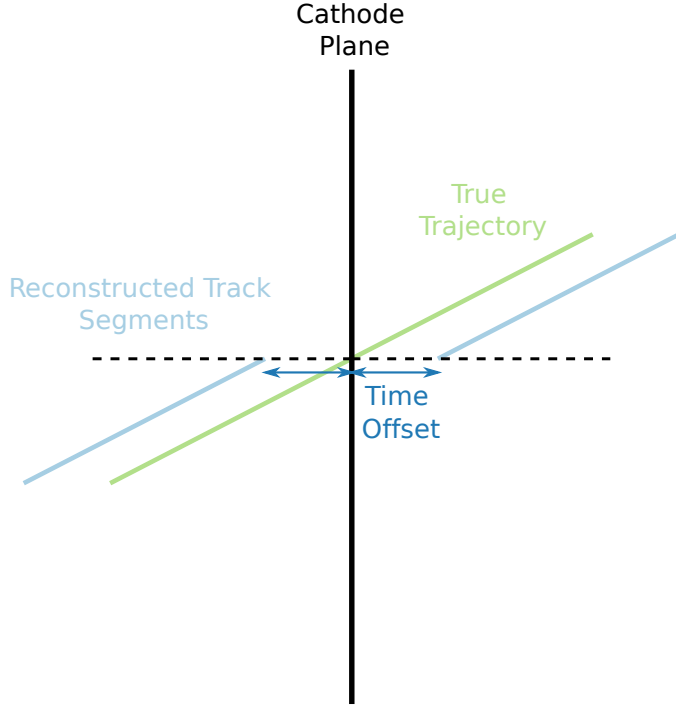


Figure 3.11: Diagram demonstrating the track stitching algorithm in ProtoDUNE-SP.

is shown in Figure 3.11. After the cosmic pass any clear cosmic-ray candidates are removed under the following conditions [57]:

- The particle travels through both the top and bottom of the detector.
- The assigned t_0 is inconsistent with the beam time.
- If no t_0 assigned, try $t_0 = 0$. If any hits are reconstructed with positions outside of the detector this track is inconsistent with the beam time.

Beam particle reconstruction considers only the hits that were not removed by being labelled as clear cosmic-rays. These hits are formed into 3D slices which contain all the hits from a single parent particle and its daughters. The slices are reconstructed under both the cosmic-ray and beam particle hypothesis, and a boosted decision tree (BDT) is used to determine whether a given slice is consistent with being a beam particle [TODO].

Under the beam particle hypothesis a more complex chain of algorithms is used to reconstruct a given slice, these algorithms are capable of reconstructing the

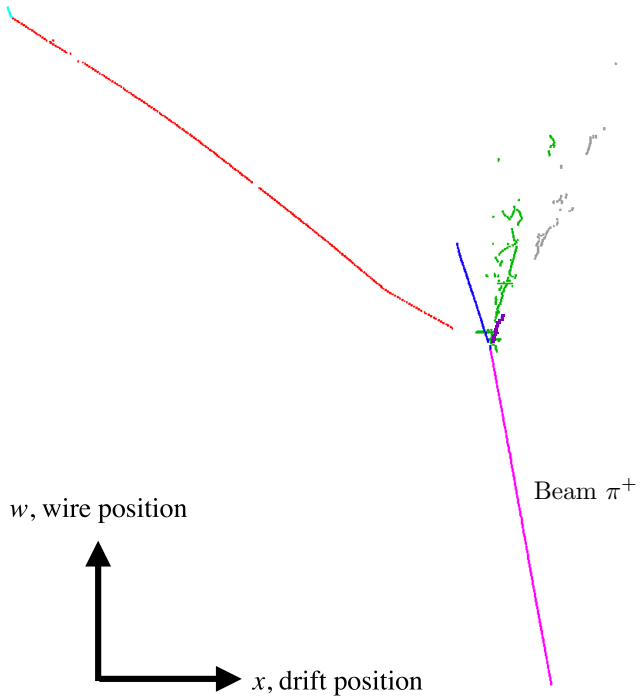


Figure 3.12: Reconstructed particle hierarchy from Pandora. Figure from [57].

particle hierarchies seen in the complex hadronic interactions from the ProtoDUNE-SP beam. These algorithms return the particle flow of the interactions in the form of PFParticles as well as the reconstructed interaction vertex for the primary beam particle. An example of the reconstructed particle hierarchy from a ProtoDUNE-SP beam event is shown in Figure 3.12.

As well as precise spatial reconstruction, LArTPCs provide excellent calorimetric information. To convert the measured charge of each hit into a reconstructed energy a number of spatial and dQ/dx dependent factors need to be taken into account. The reconstructed charge of each hit is given by the integrated area under the gaussian fit to that hit. The dx for each hit varies based on the direction of the track with respect to the wires, it is equal to the wire spacing divided by the sine of the angle between the wire and the 2D projection of the track onto the anode plane.

A number of factors affect the measured dQ/dx , these effects need to be corrected in order to recover the dQ/dx at the source of the ionisation. These factors are split into two parts in the ProtoDUNE-SP reconstruction:

- Corrections in the drift direction, X corrections. Examples include longitudinal diffusion, attenuation on impurities, and drift velocity variations.
- Corrections in the direction of the wire planes, YZ corrections. Examples include wire to wire response variations, and transverse diffusion.

Calibration factors are calculated for both sets of corrections by considering a sample of cathode crossing muons. The aim of these calibration matrices is to normalise the response over the TPC volume based on the median of the measured dQ/dx distribution in each location. The distribution is then normalised to the average value at the anode plane, where the effects of the X corrections are expected to be negligible. The corrected dQ/dx is given by

$$(dQ/dx)_{\text{corrected}} = N_Q C_{yz}(y, z) C_x(x) (dQ/dx)_{\text{reconstructed}}, \quad (3.1)$$

where N_Q normalises the median of the distributions to the median value at the anode, and C_{yz} and C_x are the calibration factors for the YZ and X corrections respectively.

The final step in energy reconstruction is to convert the corrected dQ/dx into a reconstructed dE/dx , this involves accounting for electron–ion recombination at the source. The modified box model is used to model the recombination correction, this model has been studied in a LArTPC by the ArgoNeuT experiment [71]. The reconstructed dE/dx is

$$\frac{dE}{dx} = \left(\exp \left(\frac{\frac{dQ}{dx}}{C_{\text{cal}}} \frac{\beta' W_{\text{ion}}}{\rho \epsilon} \right) - \alpha \right) \left(\frac{\rho \epsilon}{\beta'} \right) \quad (3.2)$$

where C_{cal} is a calibration constant used to convert ADC to electrons, W_{ion} is the work function of argon, ϵ is the local electric field, ρ is the liquid argon density, and $\alpha = 0.93$ and $\beta' = 0.212 \text{ (kV/cm)(g/cm}^3/\text{MeV}$ are the box model parameters as measured by ArgoNeuT. The calibration constant, C_{cal} is calculated by fitting the most probable value of the reconstructed dE/dx distribution as a function of range to the theoretical prediction for dE/dx vs range for a sample of stopping muons, as shown in figure 3.13.



Figure 3.13: dE/dx vs residual range for a stopping muon sample in ProtoDUNE-SP data. Figure from [57].

3.8 ProtoDUNE-SP Online Monitoring System

As well as monitoring the stability of the detector and DAQ systems, the quality of the collected data has to be constantly monitored. This assures the shifter that the data is of high quality, and prevents long runs of low quality data being collected. The online monitoring system (OM) is responsible for providing this quality assurance.

As shown in Figure 3.8, the OM is a part of the ProtoDUNE-SP DAQ system. The OM is responsible for processing the data and displaying the results to the shifter in the control room as soon as possible after the event was triggered. It consists of three main components:

- Analysis processes which decode and analyse the raw data from each detector subsystem.
- Merging processes which collate monitoring data from each subsystem.
- A web interface which displays monitoring data.

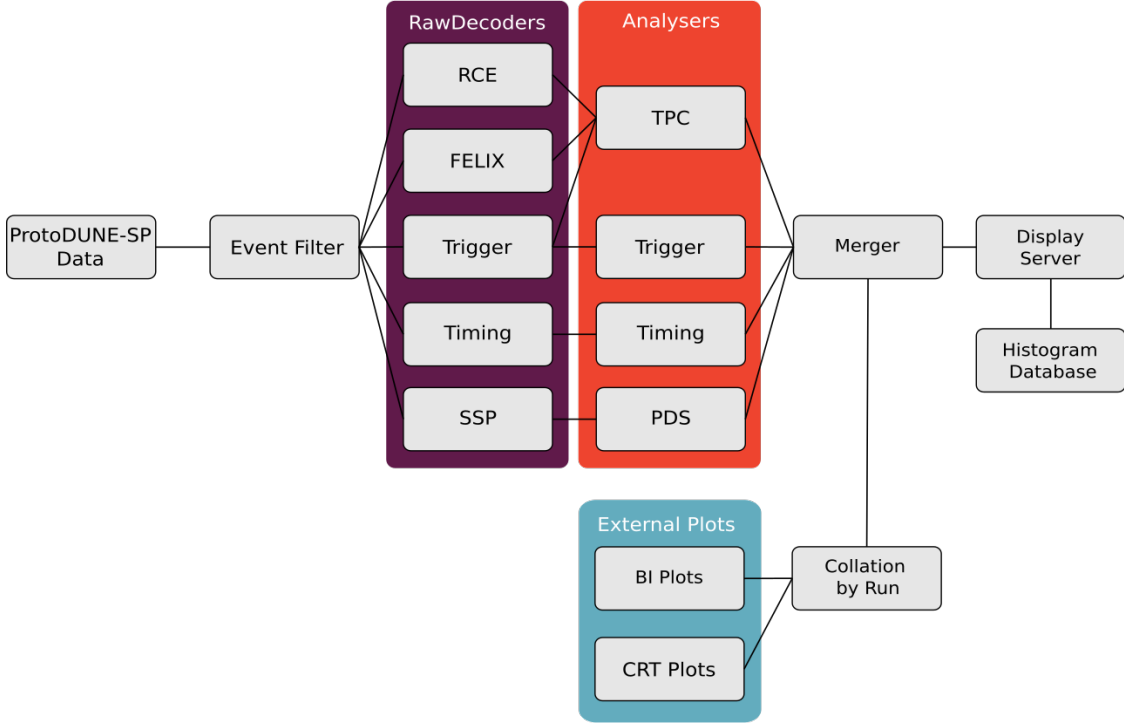


Figure 3.14: Data flow in the ProtoDUNE-SP online monitoring system.

An overview of the data flow in the OM is shown in Figure 3.14. Data from the detector is first filtered before being run in any OM processes. The data which is passed onto the OM processes is then split up and decoded by the relevant RawDecoder which reformats the data ready for analysis. A number of Analyser modules then make use of this data to make plots, which are merged along with plots from external systems, and sent to a web interface to be displayed in the control room. The following sections will provide a brief summary of these stages, as well as examples of the plots which are produced in the OM.

3.8.1 Data Processing

The data processing for the OM is based on Fermilab's art and artdaq software frameworks [60, 62], the only exception is the beam instrumentation data which is analysed outside of the OM system by the CERN beam group. The beam instrumentation plots are merged with the rest of the OM plots after data processing.

The first step of the data processing is event filtering, the main purpose of this step is to control the flow of data into the OM. Two types of filtering take place

sequentially; first a random filter is used to cut the data rate into the OM to a manageable level, then a second filter which aims to increase the likelihood that processed events were triggered by the beam instrumentation or cosmic-ray tagger. Different OM processes take different amount of processing time per event, therefore multiple filters are used which control the data rate into each process separately.

After filtering the events are ready to be processed. The data coming into the OM system is in its raw form, it arrives in small pieces known as Fragments which have to be decoded before they can be used by the OM. The RawDecoders are responsible for interpreting the headers and data streams from each detector component, and restructuring the data ready for processing. The details of the decoding vary based on the readout system under consideration; each readout system defines a class which details the contents of each fragment, the RawDecoders use the contents of this class to decode the fragments to prepare the data for processing.

After the data has been decoded it is ready to be analysed, this is done by a number of Analyser modules which analyse the data from different detector components and produce ROOT [72] plots as output. Details of the processing done for each detector component will be given below.

Time Projection Chamber

As the largest data source in ProtoDUNE-SP the TPC data was analysed in several small steps: basic data checks, pedestals and noise, Fourier analysis, and event displays. Examples of some of the plots produced by the TPC analysis are detailed below.

The basic data checks are intended to quickly spot any fundamental issues with the incoming data. An example of a basic check is to check which FEMBs are active in the monitored events, Figure 3.15a shows an example of the number of events recorded by each FEMB on APA 1 for a sample of 10 analysed events.

The pedestals and noise are continually evaluated by the online monitoring, this data is displayed in the control room and used later in the monitoring chain to flatten the background in the event displays. Basic hit removal is used to ensure

that the pedestals and RMS are only calculated in the regions of the readout corresponding to noise signals. The RMS of all channels can be represented on a single plot by arranging the channels into a 2D grid and displaying the RMS as the colour scale on a 2D histogram, an example of this plot is shown in Figure 3.15b.

To identify noise sources in the APA it is useful to study the Fourier transform of the signal distribution, this allows the frequencies to be identified and the Fourier distributions can be studied under different conditions to identify noise sources; the cameras in the TPC were identified as a noise source in this way. The OM therefore provides fast Fourier transforms (FFT) for each APA, an example of the FFT for a single FEMB is shown in Figure 3.15c.

Event displays display all the data from all the TPC readout channels simultaneously, and as such they provide the most general check of TPC performance in the OM. During the beam run of ProtoDUNE-SP a number of issues in the data were first identified in the event display, for example issues in the channel mapping and timing synchronisation. They are also particularly useful for checking that the beam trigger results in beam particles in the TPC. As a result a significant effort was made to make event displays available in the ProtoDUNE-SP OM system; in particular changes to the display server were required, these will be discussed later.

Event displays were offered for all views in all APAs, as well as a specific beam window event displays in each view, and stitched event displays for all of the APAs on each side of the TPC. As the slowest plot to make in the OM, only one set of event displays was made per OM output file; to maximise the number of beam particles in the event displays the trigger information was included during processing. An example of a beam window event display is shown in Figure 3.16; the timing synchronisation issue mentioned previously is visible here, this issue affects a single FEMB and is mitigated during offline reconstruction.

Photon Detection System

Similarly to the TPC data the PDS data is analysed for pedestal, RMS, and FFTs; in addition the raw waveforms for each channel are accumulated over a number

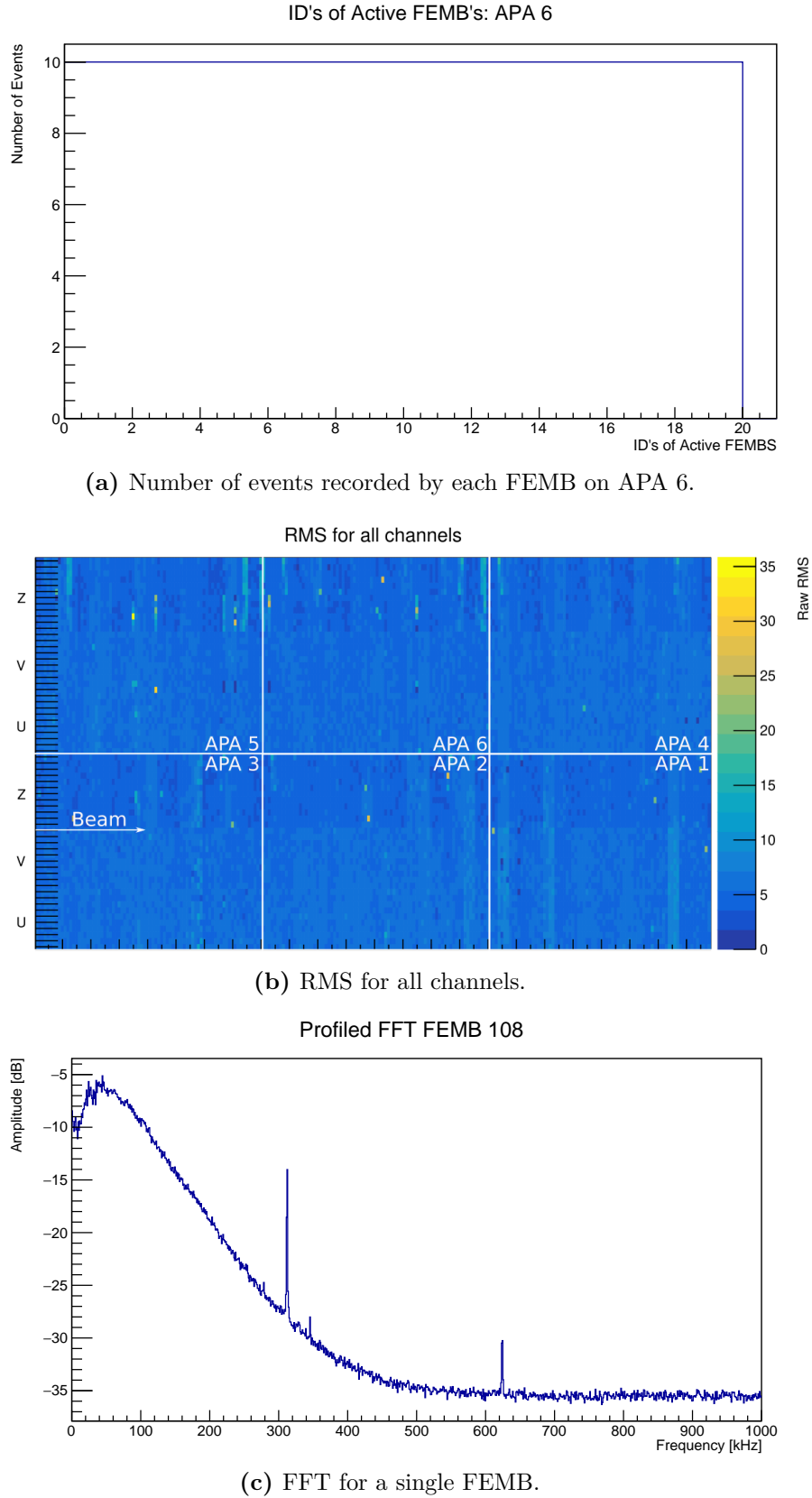


Figure 3.15: Examples of online monitoring plots for the TPC data.

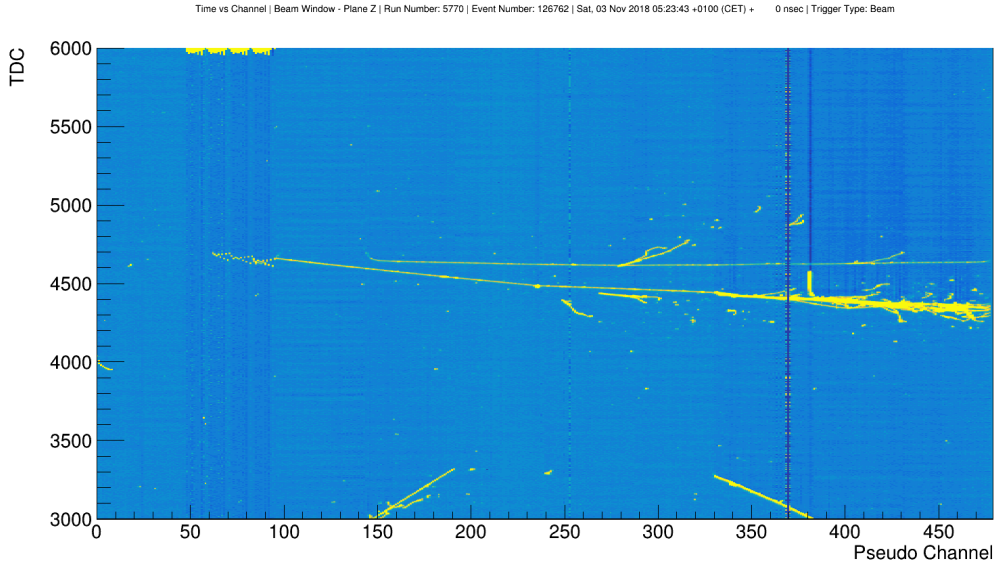


Figure 3.16: An example of a beam window event display from the ProtoDUNE-SP online monitoring system.

of events and displayed in the online monitoring. Examples of some of the PDS monitoring plots are shown in Figure 3.17.

Trigger and Timing

The trigger and timing systems share much of the same data, because the timing system is used to distribute the triggers from the trigger system, so their monitoring is related. Some examples of useful timing and trigger plots include time-stamp difference distributions, and trigger records. The time-stamp delta plots show the difference in time-stamp between consecutive events, this distribution can be used to monitor the stability of the trigger rate during triggered operation. Trigger records are 2D histograms which details of the time and type of trigger issued by the trigger board. Figure 3.18 contains examples of these two plots.

Beam Instrumentation

The beamline instrumentation was monitored by CERN, who produced beamline monitoring plots [63]. The plots were continually overwritten on a time schedule which was decoupled from the ProtoDUNE-SP running schedule, the OM was

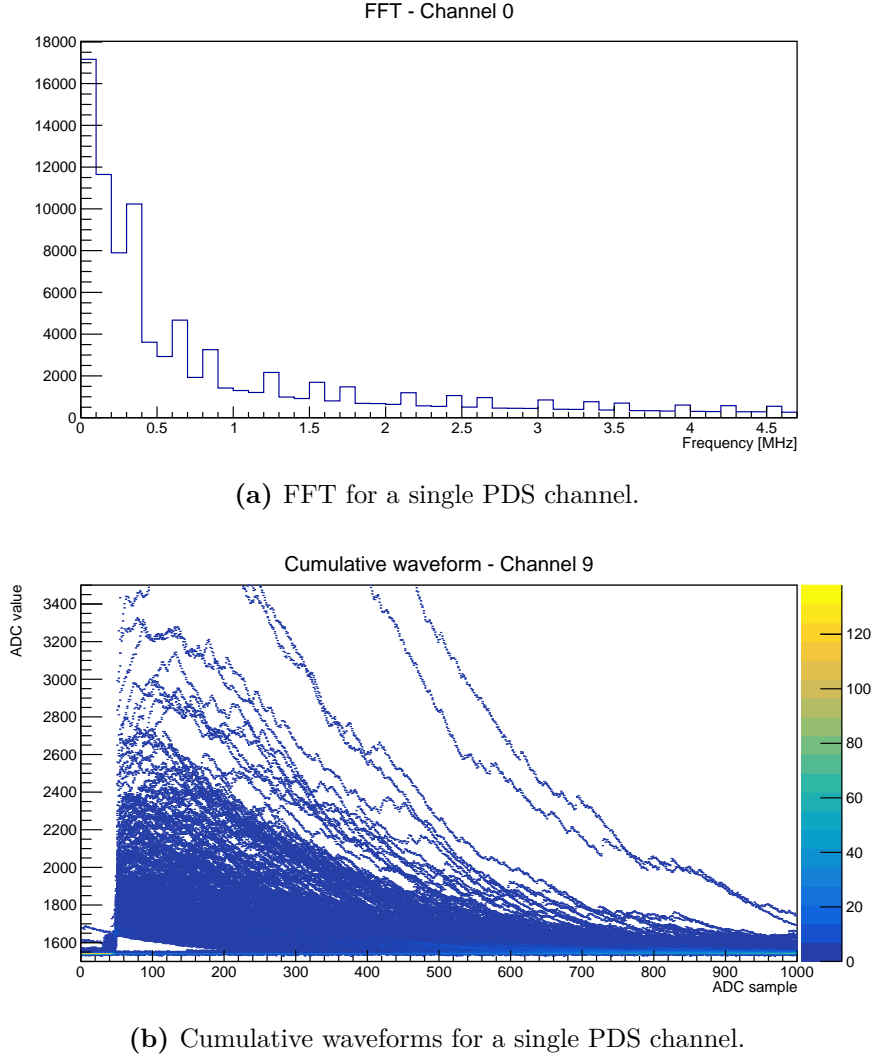


Figure 3.17: Examples of online monitoring plots for the photon detection system data.

responsible for collating the output of these plots in sync with the ProtoDUNE-SP run schedule, such that the collated beam information for each run could be monitored. After collation the beam instrumentation plots were merged with the rest of the OM plots. The beam instrumentation plots included momentum, and time of flight, examples of which are shown in Figure 3.19.

Cosmic Ray Tagger

A bug in the DAQ meant that the CRT was run separately during the main beam run. Therefore, the CRT data was analysed separately from the rest of the ProtoDUNE-SP systems and merged in the OM similarly to the beam instrumentation data.

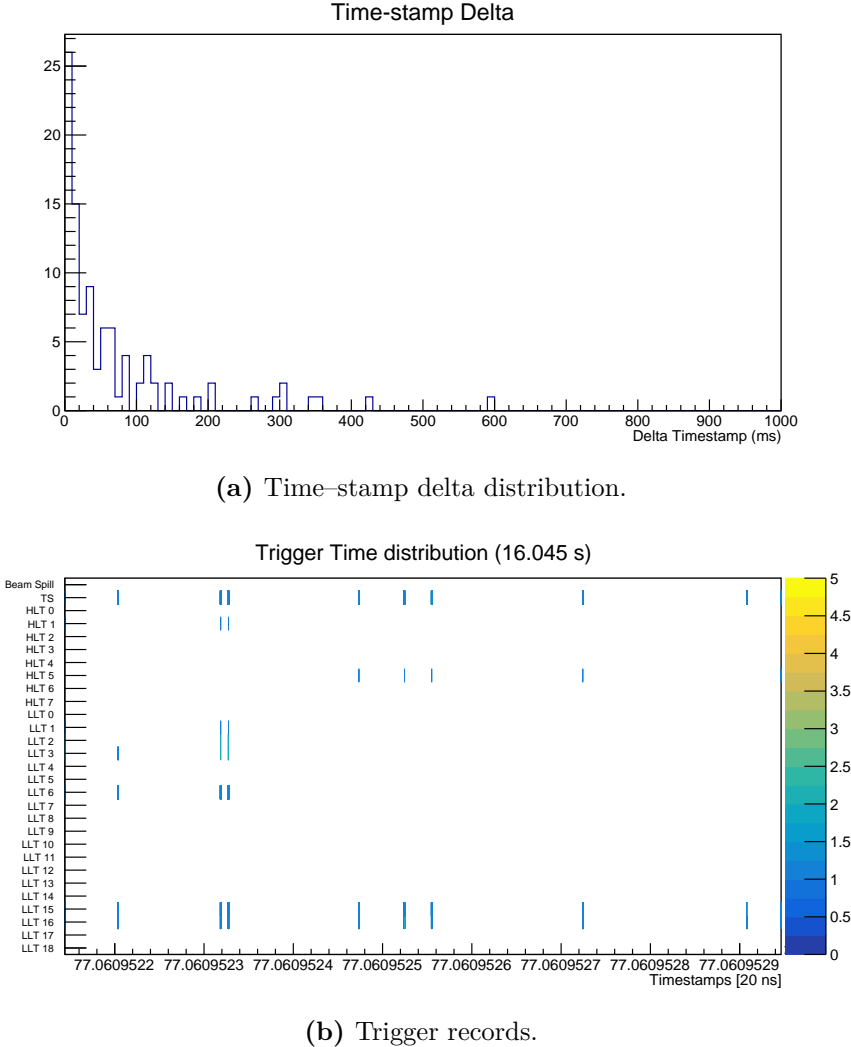


Figure 3.18: Examples of online monitoring plots for the timing and trigger data.

Some examples of CRT monitoring plots include plots of the rate of hits for each channel, and the mean ADC for each channel, these are shown in Figure 3.20.

3.8.2 Monitoring Web Interface

The plots from the data analysis are stored in a ROOT file on the ProtoDUNE-SP DAQ servers, this data is viewable from anywhere in CERN via a web interface which was adapted for ProtoDUNE-SP from LHCb’s Monet [73]. Monet consists of a Flask web application [74] which uses Bokeh [75] to render plots for display, ROOT [72] and NumPy [76] are used to process the monitoring data in preparation for display.

Two important modifications were made to Monet for ProtoDUNE-SP: efficiency

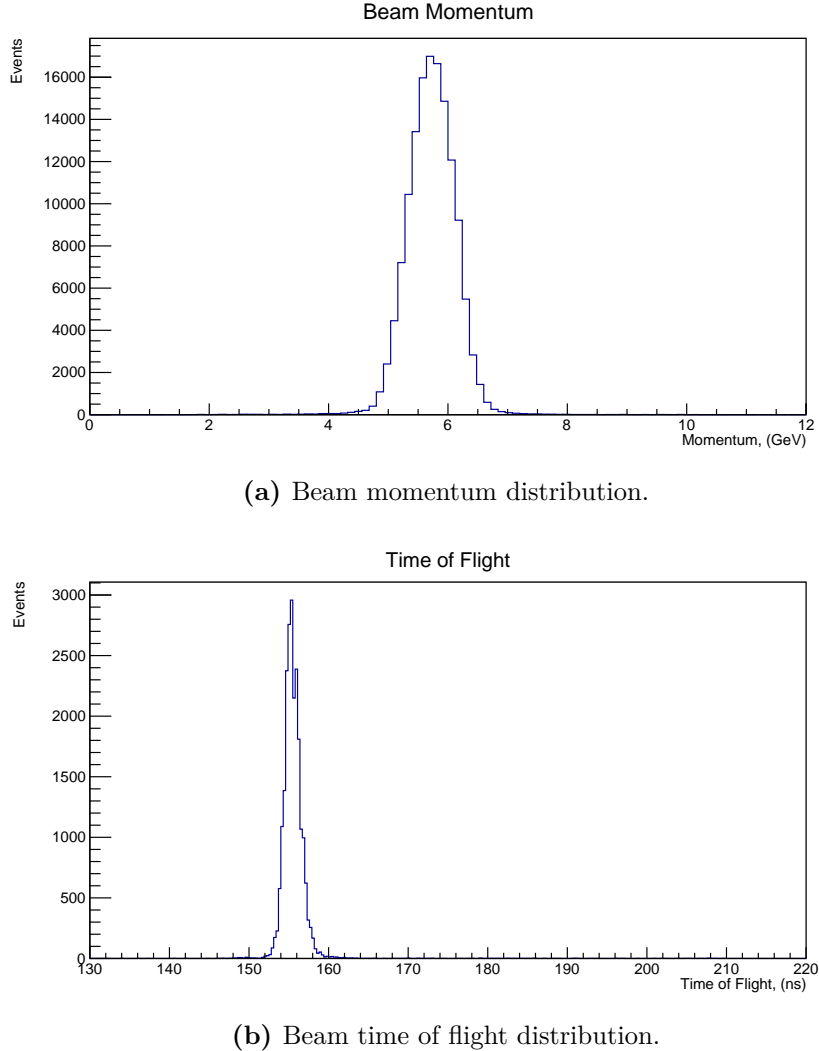


Figure 3.19: Examples of online monitoring plots for the beam instrumentation.

improvements which were required to handle the large amounts of data in the event displays, and the addition of a separate rendering server with additional capabilities.

The components of the web interface, and their connections, are outlined in Figure 3.21. When a user makes a request, which could be a request to open a new page of plots or a request to interact with a plot, the request is sent to the display server which decides what to do with it. Depending on the nature of the request the display server will then interact with the histogram database and/or the rendering server, before updating the plots and displaying them to the user.

The plots in the monitoring files are organised into pages in Monet. Each page can contain any number of plots which are organised into an array on the screen,

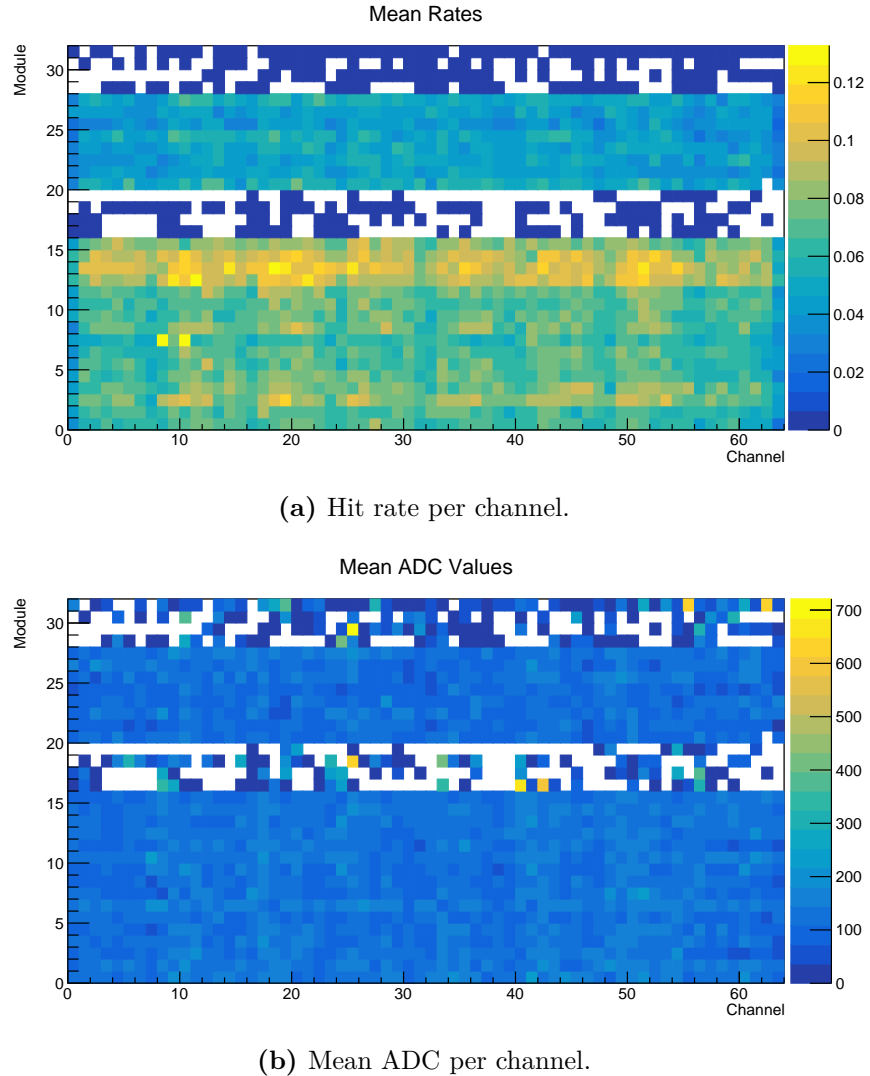


Figure 3.20: Examples of online monitoring plots for the cosmic ray tagger.

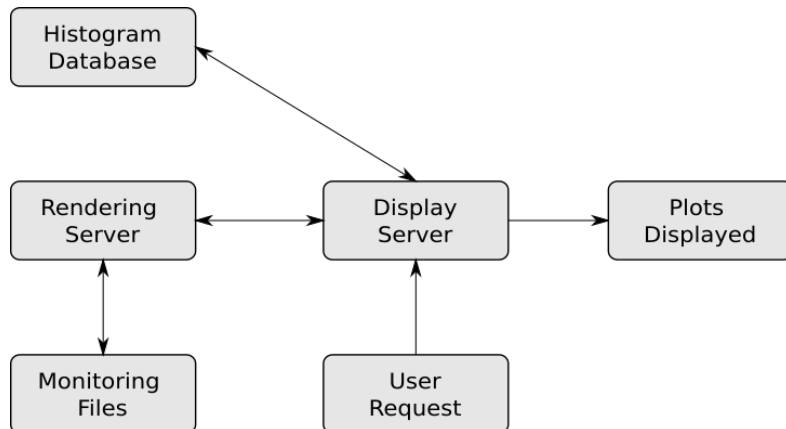


Figure 3.21: Data flow diagram for the web interface in the ProtoDUNE-SP online monitoring system.

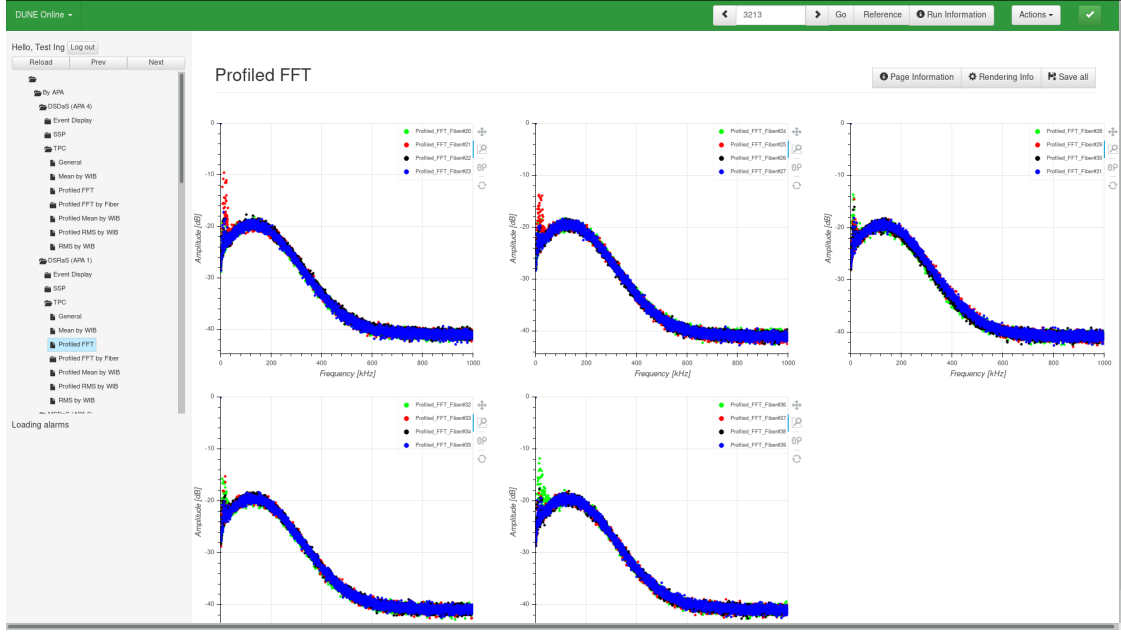
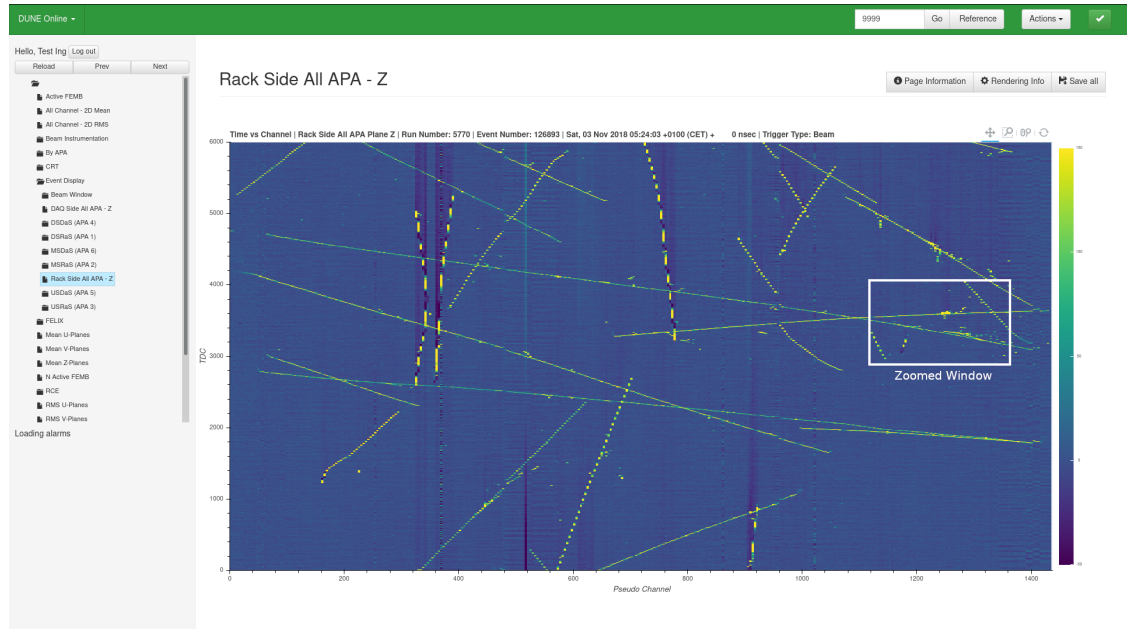


Figure 3.22: An example of an online monitoring page, profiled FFTs for APA 1.

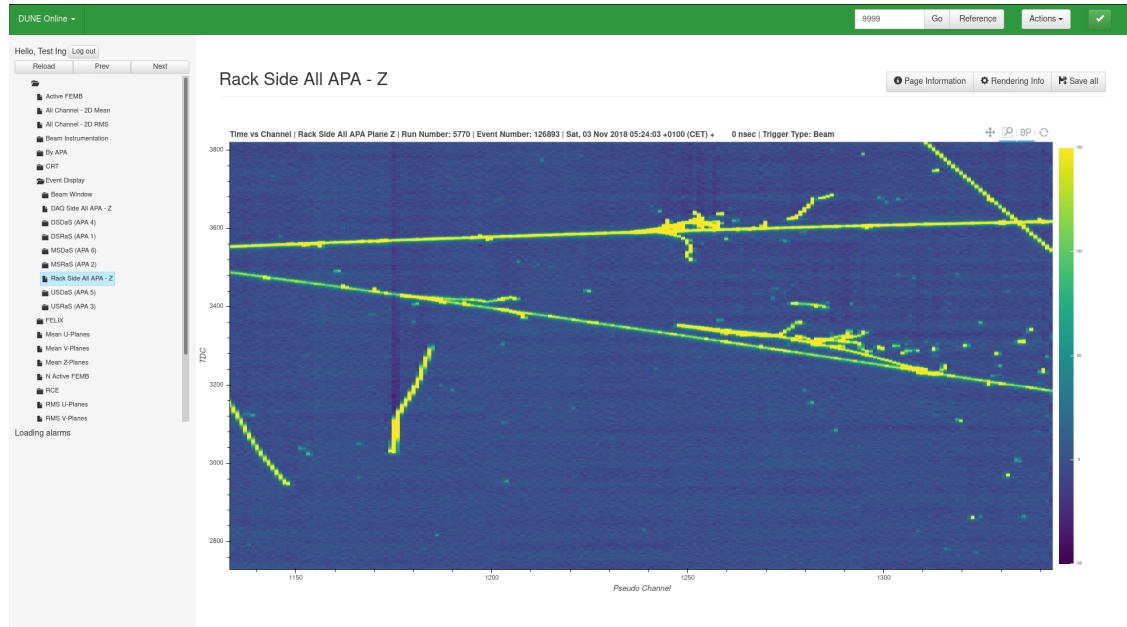
an example of this is shown in Figure 3.22. The histogram database is responsible for the details of each of these pages, this includes the plots on each page, their locations, and the relevant rendering options for each plot. When a new page is requested the display server requests these details from the histogram database before requesting the rendering server to render the plots.

The rendering server is responsible for rendering the plots from the monitoring ROOT files, it is capable of rendering all 1D and 2D ROOT plots. In LHCb’s Monet rendering is handled directly on the display server, however in ProtoDUNE-SP an additional rendering server was added. By separating the rendering processes onto their own server additional functionality was possible. The main advantage of the rendering server was that it enabled the OM to utilise a dynamic binning algorithm to scale the resolution of the displayed images in response to user interaction. This is mainly used for the event displays; the event display is initially loaded in a low resolution, but if a user is interested in a specific region of the event display then they can zoom in on the region of interest, which is then displayed at a higher resolution by the dynamic binning algorithm, as demonstrated in Figure 3.23.

The other significant modification to Monet was to modify the data handling to



(a) Full APA view. The white square represents the zoomed region in Figure 3.23b.



(b) Zoomed region.

Figure 3.23: Example of the dynamic binning algorithm in the ProtoDUNE-SP online monitoring system.

significantly improve the efficiency of data transfer to the renderer. When Monet was first adapted for ProtoDUNE-SP it was too slow to render some of the larger plots such as event displays, it would take minutes to render a single event display. By improving the efficiency of the data transfer from ROOT to Bokeh, the rendering time was reduced to around 4 seconds per event display.

In the ProtoDUNE-SP Technical Design Report [54], the proposed online monitoring system was described as being able to provide data quality assurance in real-time, in practice the response time is around one minute. During this time each set of plots will have contain data from 10 events, however, the event displays and TPC FFTs each contain data from one event. TODO: Should I include a discussion of possible improvements?

4

Electromagnetic Energy Loss in Liquid Argon

Contents

4.1 Electromagnetic Energy Loss in Matter	69
4.1.1 Energy Loss for Heavy Charged Particles	70
4.1.2 Energy Loss for Electrons	70
4.1.3 Energy Loss for Photons	73
4.1.4 Typical Interaction Signatures in ProtoDUNE-SP	76

The energy loss of particles in liquid argon has important implications for the reconstruction of different particles in a LArTPC, and will be relevant for the reconstruction algorithms developed in Chapters 6 and 7 of this thesis. This chapter will cover in more detail the theory of electromagnetic energy loss in liquid argon, highlighting the important features of the energy loss for muons, electrons, and photons.

4.1 Electromagnetic Energy Loss in Matter

In matter, charged particles lose energy through a number of small successive collisions with the electrons in the material, and by radiative processes which produce additional particles in the material. The relative importance of the collision

and radiative stopping power depends on the mass and the energy of the particle. For most particles, which are heavy compared to the electron, radiative energy losses are not important until very high energies, e.g. for a muon they are not important until momenta of around 100 GeV. However, radiative energy loss become important for electrons at tens of MeV [29]. As a result, different theories are used to describe the energy loss of heavy particles and electrons in matter.

4.1.1 Energy Loss for Heavy Charged Particles

For heavy particles such as muons at moderate energies, the mean rate of energy loss per unit distance is described by the Bethe equation,

$$-\left\langle \frac{dE}{dx} \right\rangle = K z^2 \frac{Z}{A} \frac{1}{\beta^2} \left[\frac{1}{2} \ln \frac{2m_e c^2 \beta^2 \gamma^2 W_{max}}{I^2} - \beta^2 - \frac{\delta(\beta\gamma)}{2} \right]. \quad (4.1)$$

The constants in this equation are detailed in reference [29]. Z and A are the atomic number and mass number of the medium, z is the charge of the scattering particle, W_{max} is the maximum energy transfer per collision, I is the average excitation energy, and δ is a density effect correction which is relevant in solids and liquids.

Three important features of the energy loss in the Bethe formula are the minimum ionising region, the relativistic rise, and the Bragg peak, these regions can be seen in Figure 4.1 which shows the dE/dx for muons in argon as a function of momentum.

Delta Rays

Another feature of the electromagnetic energy loss of heavy particles that impacts reconstruction in LArTPCs is delta rays. Delta rays are energetic electrons which are knocked out of their atoms when they collide with the heavy particle, in liquid argon detectors these electrons are seen as small electron tracks which protrude from muon tracks.

4.1.2 Energy Loss for Electrons

Electrons and positrons undergo different electromagnetic scattering processes in matter, Møller scattering and Bhabha scattering respectively [TODO]. These processes, which dominate electron and positron energy loss at low energies, have

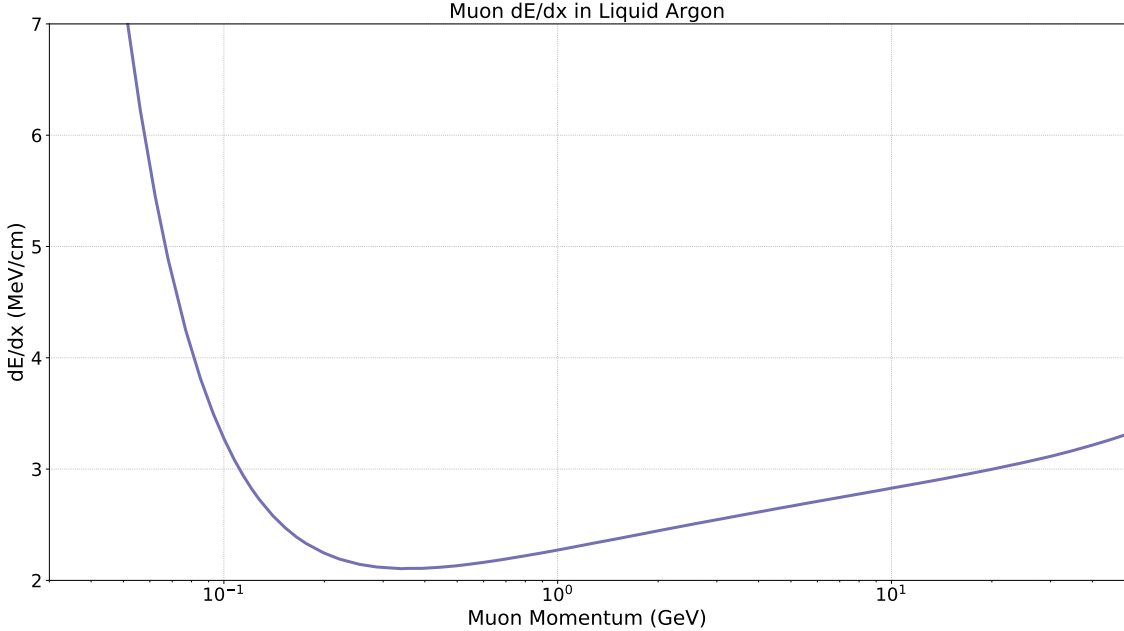


Figure 4.1: Stopping power as a function of energy for muons in liquid argon. Data from [77].

different cross sections which modify the energy loss in each case. At higher energies, radiative processes such as bremsstrahlung dominate. The two components of the electron stopping power are known as the collision stopping power and the radiative stopping power.

Collision Stopping Power

The collision stopping power of electrons and positrons is calculated with a similar method to the heavy particle stopping power, where individual collisions are considered in succession. The main difference in the calculations is the cross sections used in the calculations, for electrons the Møller scattering cross section is used, and for positrons Bhabha scattering is considered. Due to the electrons and positrons having the same mass as their targets, the maximum energy transfer in a single collision, W_{max} , is the total kinetic energy. However, this value is halved for the case of electrons, due to the convention of calculating the stopping power for the final state electron with higher kinetic energy.

The stopping power based on Møller scattering of electrons gives,

$$-\left\langle \frac{dE}{dx} \right\rangle = \frac{1}{2} K \frac{Z}{A} \frac{1}{\beta^2} \left[\ln \frac{m_e c^2 \beta^2 \gamma^2 \{m_e c^2 (\gamma - 1)/2\}}{I^2} + (1 - \beta^2) - \frac{2\gamma - 1}{\gamma} + \frac{1}{8} \left(\frac{\gamma - 1}{\gamma} \right)^2 - \delta \right],$$

while Bhabha scattering, which governs the positron stopping power, gives,

$$-\left\langle \frac{dE}{dx} \right\rangle = \frac{1}{2} K \frac{Z}{A} \frac{1}{\beta^2} \left[\ln \frac{m_e c^2 \beta^2 \gamma^2 \{m_e c^2 (\gamma - 1)\}}{2I^2} + 2 \ln 2 - \frac{\beta^2}{12} \left(23 + \frac{14}{\gamma + 1} + \frac{10}{(\gamma + 1)^2} + \frac{4}{(\gamma + 1)^3} \right) - \delta \right],$$

where the terms have the same meanings as in Equation 4.1 [29].

Radiative Stopping Power

Above a few tens of MeV, electrons lose most of their energy through the emission of bremsstrahlung photons. Detailed discussion of the energy loss due to bremsstrahlung emission is beyond the scope of this thesis, detailed discussions are provided by [29, 78]. Here, we discuss a simplified model which highlights the important factors relevant for the work in this thesis.

At high energies, where the radiative energy loss is dominant, the energy of the electron can be approximated as an exponential decay over a length scale known as the radiation length, X_0 ,

$$E = E_0 e^{-x/X_0}.$$

In this approximation, the energy loss per unit distance due to bremsstrahlung is,

$$-\left(\frac{dE}{dx} \right)_{brem} = \frac{E}{X_0}.$$

The radiation length, X_0 , can be parametrised as,

$$\begin{aligned} \frac{1}{X_0} &= 4\alpha r_e^2 \frac{N_A}{A} \left\{ Z^2 [L_{rad} - f(Z)] + Z L'_{rad} \right\} \\ f(Z) &= \alpha^2 Z^2 \left[\frac{1}{1 + \alpha^2 Z^2} + 0.20206 - 0.0369\alpha^2 Z^2 \right. \\ &\quad \left. + 0.0083\alpha^4 Z^4 - 0.0002\alpha^6 Z^6 \right], \end{aligned} \tag{4.2}$$

where L_{rad} and L'_{rad} are the so-called radiation logarithms, which depend on the atomic number of the material [78].

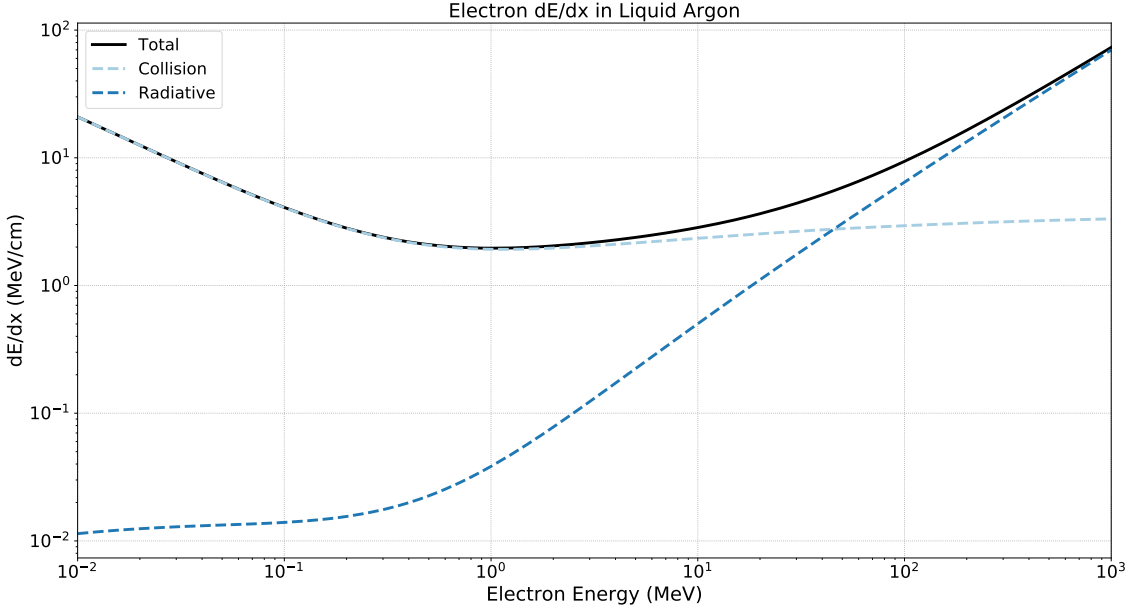


Figure 4.2: Stopping power as a function of energy for electrons in liquid argon. Data from [80].

Critical Energy

The critical energy is often defined as the energy at which the collision and radiative stopping power are equivalent, other definitions are also used, such as the definition by Rossi, the energy where the ionisation loss per radiation length is equal to the electron energy [79]. Rossi's definition is equivalent to using the approximate dE/dx calculated above[29]. The value of the critical energy has important implications for reconstruction algorithms, because different approaches are often required above and below the critical energy.

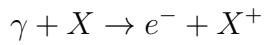
The critical energy is slightly different for electrons and positrons, in liquid argon they are both around 32 MeV, based on the Rossi definition [77]. This can be seen in Figure 4.2, which shows the total electron stopping power in liquid argon, in addition to the collision and radiative components which make up the total stopping power.

4.1.3 Energy Loss for Photons

A number of processes contribute to the energy loss of photons in matter, brief descriptions of the main processes are given below.

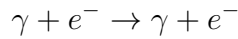
Photoelectric Effect

The photoelectric effect occurs when a photon collides with an atom, X, the photon is absorbed and electron is emitted from the atom. As a result, the atom is ionised.



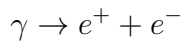
Compton Scattering

Compton scattering occurs when a photon scatters incoherently from an electron within an atom. The electron is typically liberated from the atom, and the photon loses some of it's energy.



Pair Production

Pair production is the production of an electron positron pair, in the vicinity of an external electric field. During this process, the photon is destroyed to produce the electron positron pair. In matter, the electric field could be provided by either the electrons in the atom, or the nucleus of the atom.



The cross section for these effects vary as a function of photon energy. The cross sections for each process in liquid argon, as well as the total photon cross section, are given in Figure 4.3. The Compton scattering cross section is dominant from around 0.1 MeV to 10 MeV, after which the pair production cross section dominates.

Photon Mean Free Path

The mean free path of a photon is defined as the distance travelled by the photon before it interacts with the material. The mean free path for photons has two main components for photons in the MeV range, which are due to Compton scattering and pair production. The mean free path is given by $\lambda = 1/(n\sigma)$, where n is the number density of targets and σ is the cross section per target. The contribution to the mean

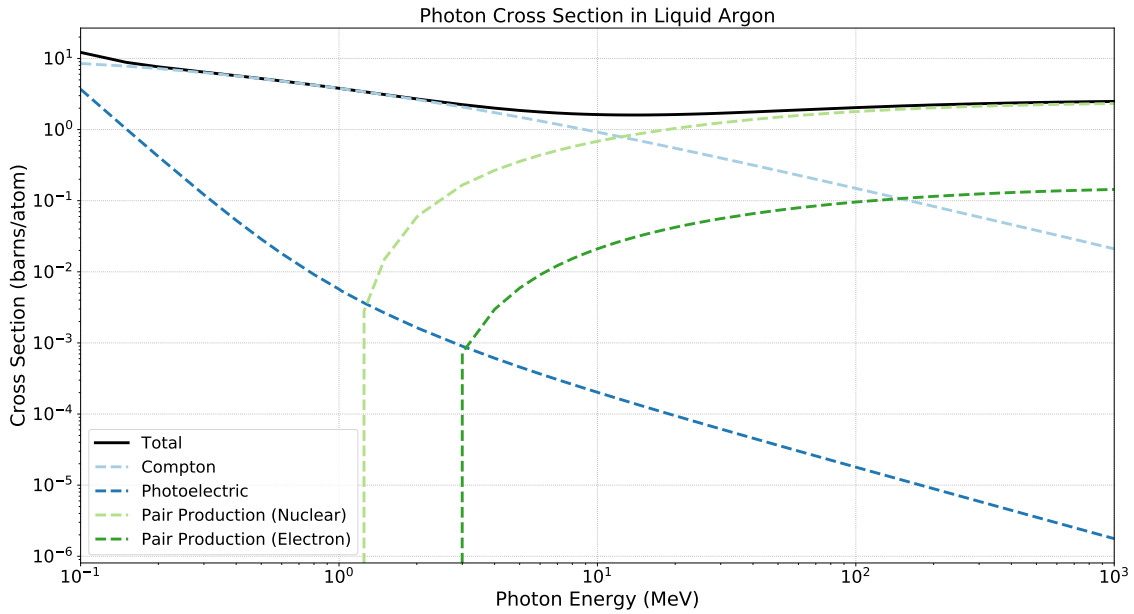


Figure 4.3: Photon interaction cross sections in liquid argon. Data from [81].

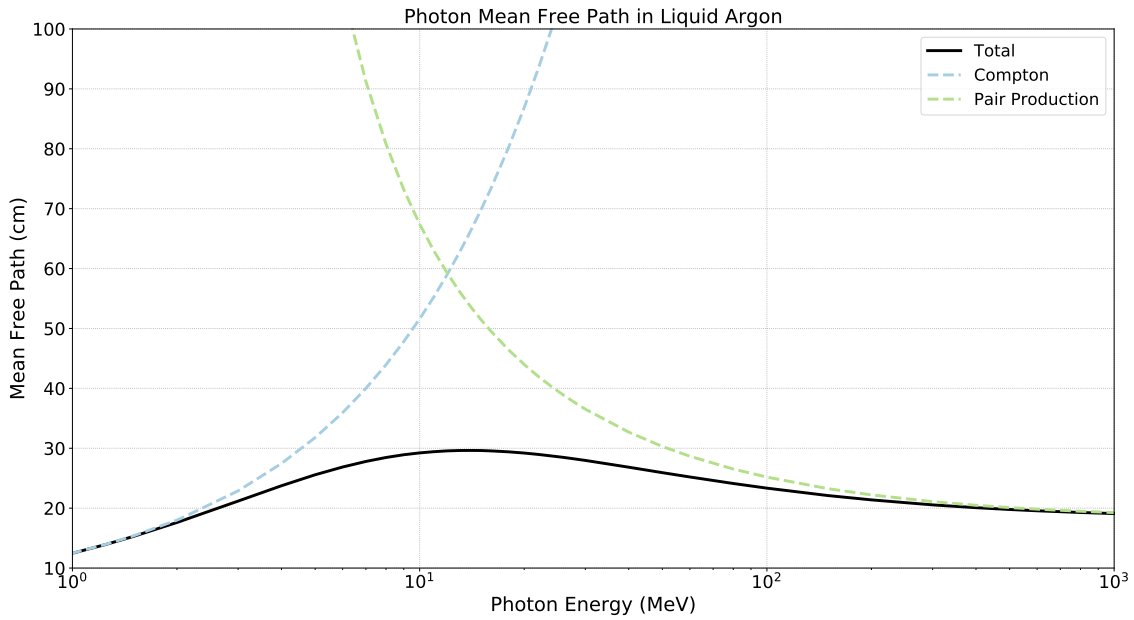


Figure 4.4: Photon mean free path in liquid argon. Data from [81].

free path from pair production is related to the radiation length for electrons, X_0 from Equation 4.2, by $\lambda_{PP} = (9/7) X_0$ [29]. The mean free path for photons in the MeV range is shown in Figure 4.4, along with the main contributing cross sections.

4.1.4 Typical Interaction Signatures in ProtoDUNE–SP

As a result of the differences in energy loss which depend on particle species and energy, different particles leave distinct signatures in the detector. Figure 4.5 shows the typical signatures of four types of interaction in a liquid argon TPC for events from ProtoDUNE–SP data.

The most common interaction in ProtoDUNE–SP is that of a cosmic ray muon, seen in Figure 4.5a. Muons, and other heavy particles, leave long tracks in the detector which deposit around 2.1 MeV/cm in the minimum ionising region. Alongside muon tracks, relatively high energy electrons, known as delta rays, are occasionally produced. Delta rays can be seen as electron activity along the length of the muon track.

Electrons in ProtoDUNE–SP have two distinct signatures, which depend on the energy of the electron. For high energy electrons, with energies above around 300 MeV, radiative energy loss dominates and showers are produced, an example of an electron shower can be seen in Figure 4.5b. These showers are the result of a cascade of electrons, which are produced by a chain of bremsstrahlung photons and electron positron pairs.

At energies in the tens of MeV range electrons have a different signature, which consists of a small electron track accompanied by a number of small ionisation energy deposits due to radiated photons. A common source of these electrons in ProtoDUNE–SP are Michel electrons, which are the electrons produced when a muon decays at rest in the detector. An example of a typical Michel electron event is shown in Figure 4.5c. The Michel electron is accompanied by the incoming Muon in the image, which cannot be separated in the ionisation signal due to the slow drift of the ionisation.

As with electrons, photon interactions in liquid argon have two distinct signatures at high and low energies. Low energy photons are typically produced by the interactions of low energy electrons in the liquid argon, such as the Michel electron interaction in Figure 4.5c. When these photons interact they produce small isolated

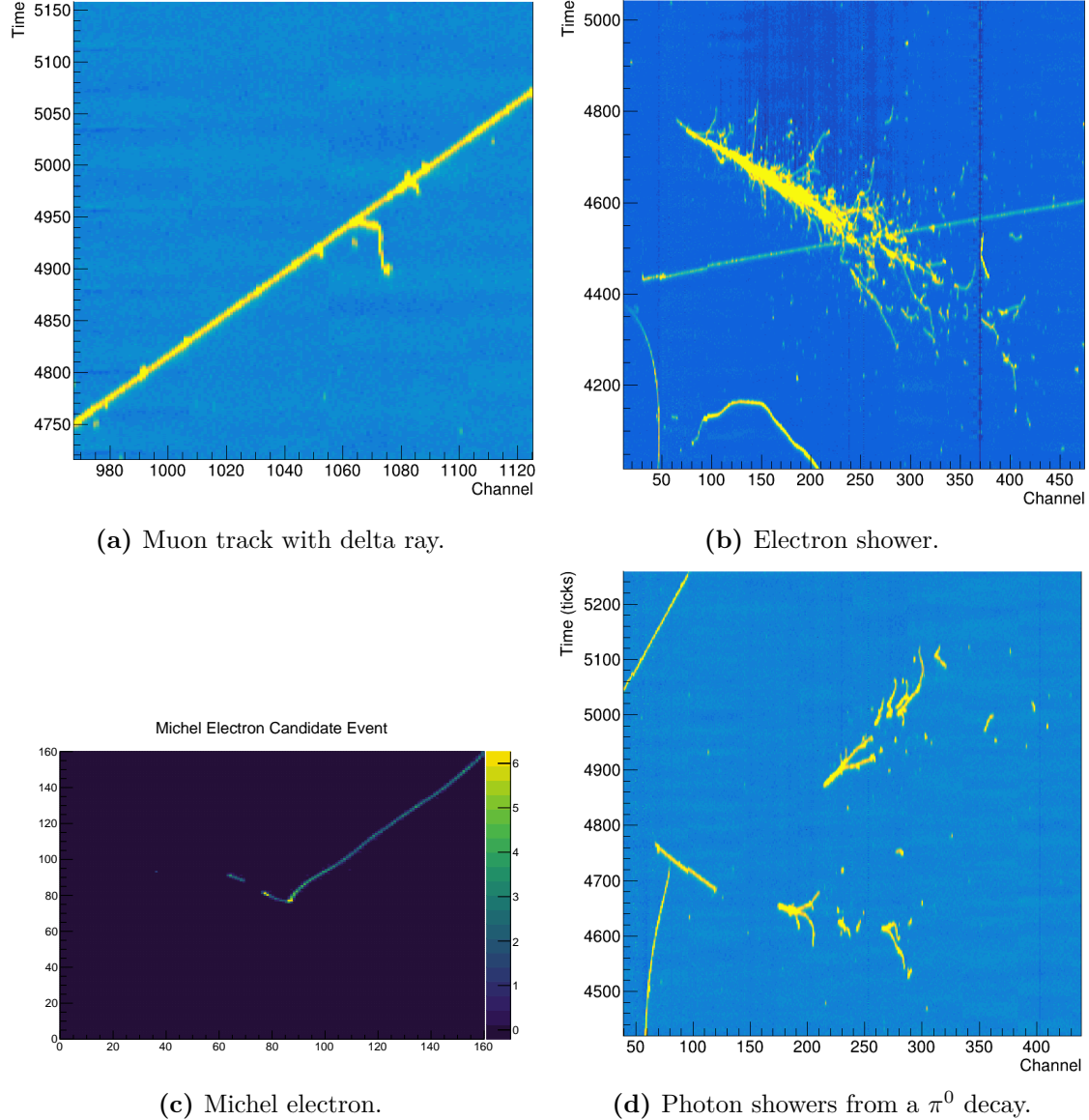


Figure 4.5: Typical particle interactions in ProtoDUNE-SP for different particle species.

energy deposits, which are created by the ionisation caused by the Compton scattered electron or electron positron pair.

At high energies, photons produce similar interactions to high energy electrons, which produce electromagnetic showers in the liquid argon. There is a slight difference in the dE/dx in the first few cm of these showers which can allow for electron and photon showers to be distinguished [82]. A common source of photon showers in ProtoDUNE-SP are π^0 decays, shown in Figure 4.5d, which produce a pair of photons.

5

Neural Networks

Contents

5.1	Artificial Neural Networks	79
5.1.1	Convolutional Neural Networks	81
5.1.2	Residual Neural Networks	83
5.2	Supervised Learning	84
5.2.1	Backpropagation	84
5.2.2	Batch Normalisation	84
5.2.3	Regularisation	84

Machine Learning (ML) is a field of research which studies algorithms which can learn to make predictions from data, i.e. predict a set of output variables, given a set of input variables. The algorithms typically take the form of a multivariate function, which is used to predict the output [83].

ML algorithms are often classified into four groups based on two distinctions: regression or classification, and supervised or unsupervised. The first distinction is based on the nature of the output distribution expected from the network; regression algorithms are designed to predict the outputs of a continuous function, whereas classification algorithms aim to separate data into groups. The distinction between supervised and unsupervised algorithms is based on the outputs used during training; in a supervised algorithm the true output is known, and the network's goal is to

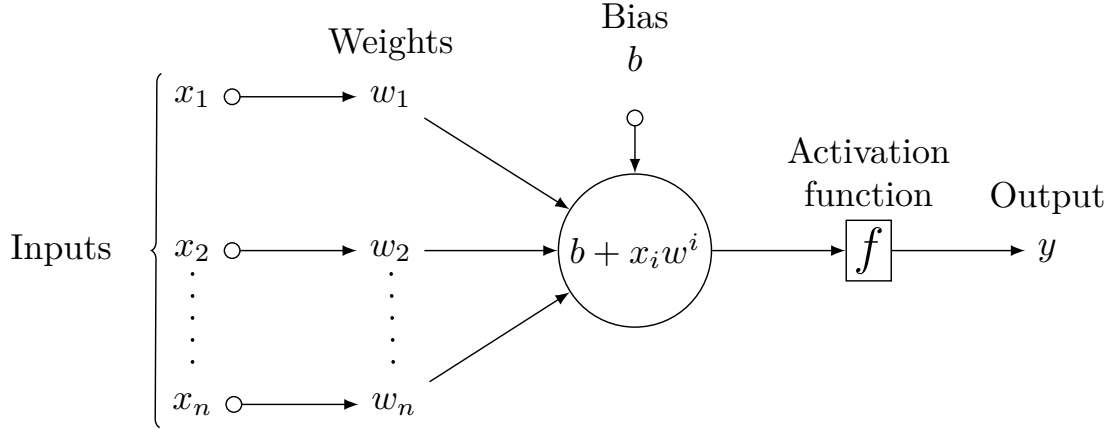


Figure 5.1: Graphical representation of an individual neuron in an artificial neural network.

predict the true output, while in an unsupervised algorithm the output is unknown, and the networks goal is to extract meaningful structure from the data.

Chapters 6 and 7 of this thesis describe two examples of the application of Neural Networks (NN) for event reconstruction in LArTPC data. These algorithms are classification algorithms based on the supervised learning approach. This chapter will not provide a full survey of the available ML techniques, instead it will briefly describe the theory behind NNs, as well as providing details of the techniques used in the subsequent chapters.

5.1 Artificial Neural Networks

Artificial neural networks (ANN) are a class of ML algorithm that draw inspiration from biological neurons. An ANN consists of a set of nodes, along with a set of connections between those nodes. The set of nodes and connections is often referred to as a graph or architecture. The nodes in the graph take the form of artificial neurons, which pass a number of inputs through an activation function to produce a single output, as depicted in Figure 5.1. The output of each neuron is either distributed to subsequent neurons in the network, or it is part of the output of the network.

One of the most widely used ANNs is the multi-layer perceptron (MLP)[83]; this class of network consists of at least three layers of nodes: an input layer, one or

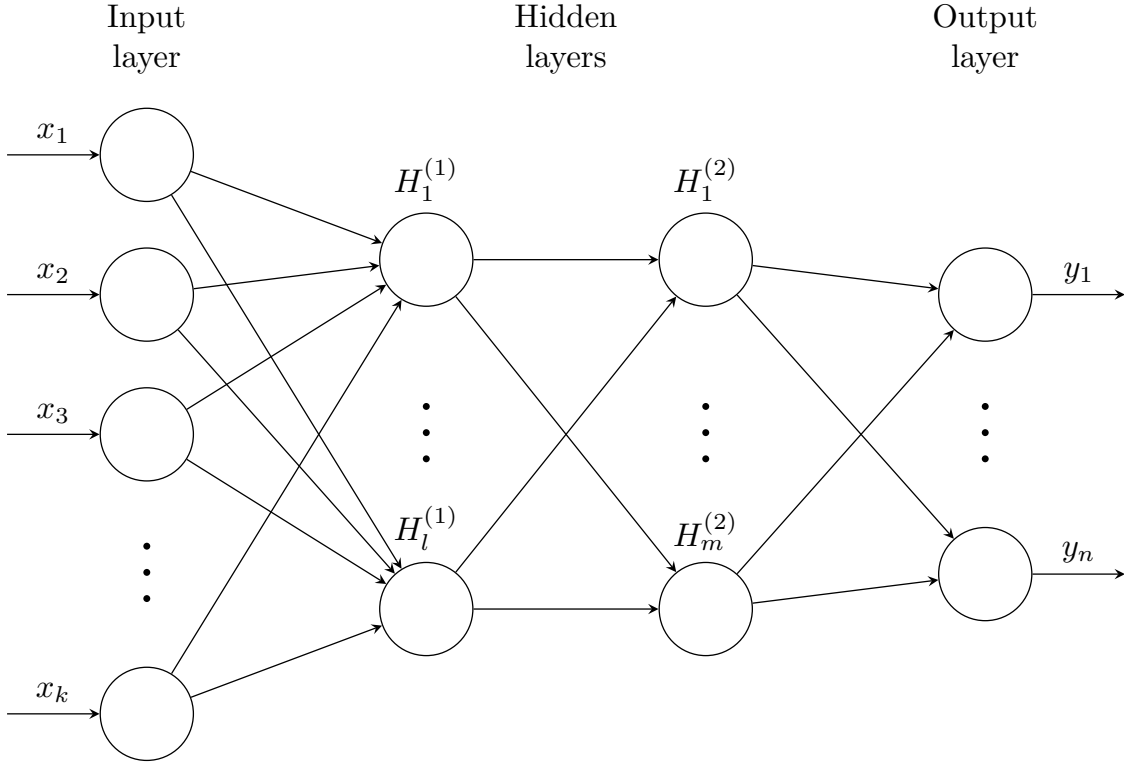


Figure 5.2: A graphical representation of a multi-layer perceptron.

more hidden layers, and an output layer. The layers are connected in a feedforward configuration, such that the graph of nodes contains no cycles. The layers of an MLP are often fully connected or dense, meaning that the output of every node is connected to the input of every node in the next layer of the network. An example of a fully connected MLP, with two hidden layers, is shown in Figure 5.2.

Each node receives input from nodes in the previous layer, and uses the inputs to calculate a response function. For the i^{th} node in the j^{th} layer of a network,

$$z^{i,j} = \mathbf{w}^{i,j} \cdot \mathbf{x}^{j-1} + b^{i,j}$$

where $z^{i,j}$ is the response function, $\mathbf{w}^{i,j}$ is the weights vector, $b^{i,j}$ is the bias, and \mathbf{x}^{j-1} is the input vector from the previous layer. This response function is usually passed through a nonlinear activation function, f , to produce the output from the node, y , which is part of the input for the next layer,

$$(\mathbf{x}^j)_i = y^{i,j} = f(z^{i,j}).$$

Some common choices for the activation function are the sigmoid function, the hyperbolic tangent, the rectified linear unit (ReLU), and the softmax function [84–86].

$$\begin{aligned}
 f(x) &= \frac{1}{1 + e^x} && \text{(Sigmoid)} \\
 f(x) &= \frac{e^x - e^{-x}}{e^x + e^{-x}} && \text{(Tanh)} \\
 f(x) &= \max(0, x) && \text{(ReLU)} \\
 f(x) &= \frac{e^{x_i}}{\sum_j e^{x_j}} && \text{(Softmax)}
 \end{aligned}
 \tag{5.1}$$

In the softmax function, the index i indicates the current node, and the index j includes all nodes in the current layer. This construction ensures that the outputs from a softmax layer sum to one, and as such this unit is commonly used in categorisation tasks when the output must belong to one of a given set of categories. The benefits and drawbacks of these common activation functions will be discussed later in this chapter, when we will discuss modifying weights with the backpropagation algorithm.

The weights and biases of the nodes in an MLP can be adjusted to make accurate predictions of data. For a classification task, there are typically as many output nodes as there are classes, with output values in the range zero to one. The output value of a classification network, quantifies how well the image represents each class, based on the networks prediction. In principle, MLPs are able to approximate any function to arbitrary precision with a single hidden layer [87]; however, there is no limit on the number of nodes required in order to achieve a good approximation. In practice, networks with additional hidden layers can reach the required precision with fewer nodes than a network with a single hidden layer, but there are diminishing returns with more than a few hidden layers [83, 84].

5.1.1 Convolutional Neural Networks

An extension of the MLP with considerable success, particularly in image classification tasks, is the convolutional neural network (CNN) [86, 88, 89], which addresses

some of the drawbacks of the traditional MLP. In particular, when evaluating data with a high dimensional input, having a fully connected network architecture leads to a large number of neurons and high computational cost. In addition, for spatially correlated data, such an architecture does not take into account the local spatial structure of the data, instead focussing on all the data at once. A CNN attempts to resolve these issues by exploiting the local spatial structure of the data.

In a CNN the singular input neurons of a traditional MLP are replaced by convolutional kernels. A convolutional kernel is a matrix containing a set of weights, which are multiplied pixel-by-pixel with small regions of the input image. The convolution operator is defined as,

$$(x * y)_i = \sum_{j=-\infty}^{\infty} x_j y_{i-j}, \quad (5.2)$$

where x and y are discrete sequences. In the machine learning context, y represents the image, and x the convolutional kernel, which is defined to be zero beyond the finite size of the filter. The convolution operation is applied to all pixels in the input image, which are replaced by the resulting convolution in the next layer of the network. Many convolutional kernels are used in each layer of the network, each producing an output image which is passed to the next layer.

Convolutional kernels are sometimes referred to as feature detectors, which emphasises the fact that each kernel identifies a given feature in the data, based on the weights in the kernel matrix. The output image from each kernel is known as a feature map, reflecting the fact that they represent the spatial distribution of the features learned by a given feature detector.

Pooling

The use of images as network input typically drastically increases the number of input parameters for a network, when combined with a large number of convolutional filters this can lead to a dramatic increase in the computational cost of training a network. Pooling [89] is a downsampling technique designed to reduce the number of parameters in the network, and therefore reduce the computational cost

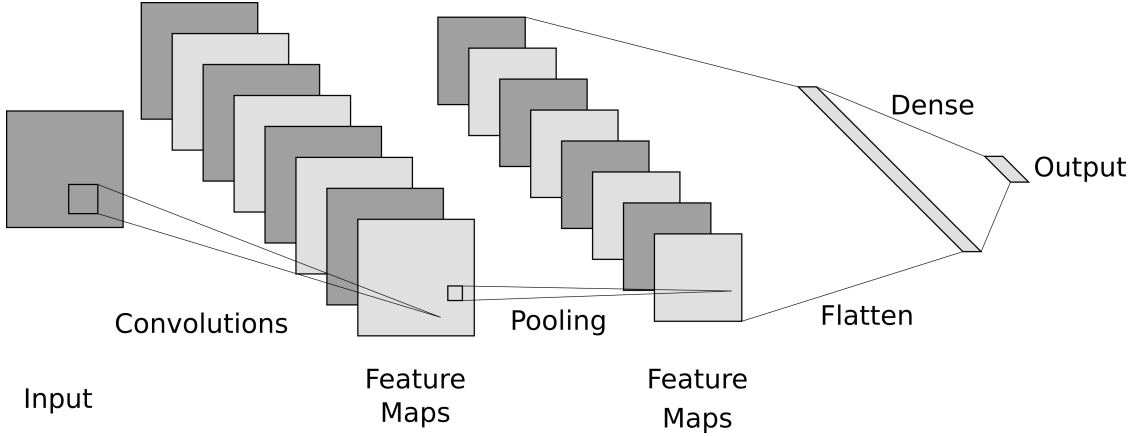


Figure 5.3: A graphical representation of a convolutional neural network. Figure generated with [90].

of making predictions. In a pooling algorithm the input data from each $m \times n$ region of the input data is downsampled to a single value, the downsampled image is used as the input for the next layer of the network. Two common pooling algorithms are max pooling and average pooling; in max pooling the maximum value from within the downsampling region is used, whereas average pooling uses the average value from the region.

While convolutions are able to extract features from the data, they typically are not able to make predictions in the desired format for classification tasks. Therefore, after convolutions, data is typically flattened and passed through one or more dense layers in order to produce the classification prediction. A graphical representation of a typical CNN architecture is shown in Figure 5.3, it includes convolutional, pooling, and dense layers.

5.1.2 Residual Neural Networks

[91]

5.2 Supervised Learning

5.2.1 Backpropagation

5.2.2 Batch Normalisation

5.2.3 Regularisation

Dropout

Early Stopping

6

Charge Identification with Convolutional Neural Networks

A major problem faced by the next generation of neutrino experiments is the correct categorisation of particle interactions within the detector. Typically identifying the underlying type of a neutrino interaction involves determining the lepton content of the final state particles; as such it is important to be able to distinguish muons from electrons, or more generally tracks from showers.

This chapter will describe an approach for hit classification in LArTPCs using machine learning techniques. A brief theoretical overview of neural networks will be presented in section 6.1, including a discussion of convolutional neural networks and their application to pattern recognition. Section 6.2 will detail an approach to hit classification in LArTPCs based on tagging the source of energy depositions with a convolutional neural network. The performance of this approach will be analysed with ProtoDUNE-SP simulation and data in sections 6.3 and 6.4 respectively.

6.1 Neural Networks

An artificial neural network (ANN) consists of a set of nodes, together with a set of connections between those nodes. The nodes in the graph take the form of an artificial neuron which passes a number of inputs through a nonlinear activation

function to produce a single output. In an ANN the connections provide a mechanism for taking the output of a given node and using it as the input for a subsequent node. This structure of nodes and connections provides a very flexible framework, the basis for a number of machine learning algorithms which utilise this flexibility to learn the structure of complex data sets.

In order for an ANN to make accurate predictions based on data, the weights and biases between each set of neurons must be tuned such that the outputs of the network match those expected for a given input. In supervised learning [92], the loss, a measure of the difference between the truth and the output of an ANN, can be used to learn the appropriate values of the weights and biases using the method of gradient descent. The loss is computed and its gradient as a function of the weights and biases can be calculated with the back-propagation algorithm [93]; the loss is then minimised based on the gradient calculated with back-propagation. This process can be repeated until the loss function reaches an acceptable level or stops decreasing.

One of the most widely used ANN's is the multi-layer perceptron (MLP) [92]; this class of networks consists of at least three layers of nodes: an input layer, one or more hidden layers, and an output layer. These layers are connected in a feed-forward configuration such that the graph of nodes contains no cycle. Traditionally, the layers are also fully connected such that the output of each node is connected to the inputs of all nodes in the next layer. These networks are able to approximate any function to arbitrary precision with a single hidden layer [87]; however, there is no limit on the number of nodes required in order to achieve a good approximation. In practice networks with additional hidden layers can reach the required precision with fewer nodes than a network with a single hidden layer [84].

ANN's provide a flexible tool for a variety of pattern recognition tasks but there can be issues with their training and use. Typical issues with ANN's include a risk of slow learning due to vanishing gradients for typical sigmoid activation functions and a high risk of over-training due to the large number of free parameters. In

particular, over-training can lead to poor generalisation of the network for real world examples, despite excellent performance when evaluated on the training sample [92].

An extension of the MLP with considerable success, particularly in image classification tasks, is the convolutional neural network (CNN) [86, 88]. When evaluating data with a high dimensional input, having a fully connected network architecture leads to large numbers of neurons and high computational cost. In addition, for spatially correlated data such an architecture does not take the local spatial structure of the data into account. A CNN attempts to resolve these issues by exploiting the local connectivity of the data; single input neurons are replaced by convolutional kernels which are evaluated on small regions of the input. These convolutional kernels are evaluated over all valid locations in the input producing feature maps which describe the spatial distribution of the features which each kernel has learned to identify. Each set of feature maps can then be used as an input for either convolutional layers or fully connected layers.

Convolutional kernels provide a local translation invariant evaluation of features within the data; with this method low level features are identified first and their spatial distribution can then be exploited to identify higher level structure in the data [88]. This makes these networks ideal for pattern recognition in images, where common features can be located anywhere in the image. The high spatial and calorimetric energy resolution of LArTPC detector data make these algorithms an ideal candidate for classification of the data, and successful applications on CNNs have been achieved in ongoing neutrino experiments [94, 95]. The remainder of this chapter will detail a use of CNNs to identify low level features in LArTPC data.

6.2 Hit Identification with Convolutional Neural Networks

As well as in neutrino event classification, effective track shower separation has important applications throughout DUNE’s physics programme; defining pure calibration samples such as minimum ionising muons and π_0 decays is crucial for understanding the energy response of the DUNE detector. Each of these samples

has a unique topology, but the first step in identifying many of these samples is the same: defining tracks and showers which can be combined to give the final state. To do this collections of hits have to be clustered and identified as track or shower objects. Here we will present a method for classifying the ionisation source of hits, a label is then associated with each hit, and subsequent reconstruction and analysis algorithms can use this when defining data samples.

Aside from track and shower objects, a useful calibration sample with a unique topology in LAr is the Michel electron. At typical Michel electron energies the ionisation energy loss of electrons in LAr undergoes a transition from collision dominated to radiation dominated, as such Michel electrons typically have a combined topology with a short track-like component and a few small radiated energy depositions. Due to the unique topology of these interactions, Michel electrons were chosen as a unique category for hit classification.

A CNN was used for hit classification, the network was trained to predict $\{p_t, p_s, p_e, p_m\}$, the probabilities for track, shower, empty, and Michel classifications respectively. The empty category is included to ensure that the network doesn't learn to assign a track-like or shower-like tag to empty or noisy regions of the data. Since the Michel electron category has overlap with the track and shower categories, the Michel electron probability is decoupled from the other probabilities which are constrained to sum to one.

Training data was built using simulations of the ProtoDUNE-SP detector in the LArSoft framework [61]; cosmic ray simulations were combined with simulations of the ProtoDUNE-SP beam for peak beam energies in the range 1–7 GeV and both positive and negative beam polarity. The input was formed of small patches of the raw detector readout in each plane, 48 wires in total were considered around the central energy deposition and an equal number of bins were formed in the drift time coordinate by averaging the ADC values over time such that the distance scale was equal in both coordinates. The truth for each training sample was obtained from the simulation by associating the measured ionisation energy depositions to the corresponding simulated particle. In total ~ 26 million input patches were produced,

figure 6.1 shows example patches for each label type, and details of the number of each patch type in the training, validation, and test data sets are given in table 6.1.

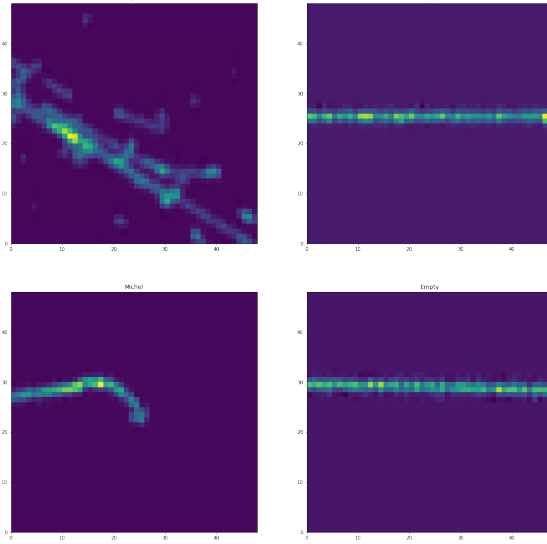


Figure 6.1: Example input patches for each label. Clockwise from top-left: Shower, Track, Empty, Michel.

Patch Type	Shower	Track	Empty	Michel
Training	13,493,982	9,727,604	2,517,882	731,456
Validation	734,673	562,038	141,388	42,727
Test	764,659	518,805	139,987	39,674

Table 6.1: Summary of the number of samples with each truth label in the training, test, and validation data sets.

The network architecture was designed to provide the best performance possible given constraints on running time; since the CNN is part of the low level reconstruction chain and it must run over a large number of candidate images for each event, run time for each event is required to be $O(10)$ s. While better classification performance was achieved with deeper networks, the best performance while achieving the running time goal was achieved with a relatively shallow network consisting of one convolutional layer followed by two dense layers; it is reasonable to assume that with improved computational resources, e.g. evaluation with GPU's, the performance of the classification could be improved within the time constraints.

The TensorFlow library was used to design and train the CNN, with the TensorBoard visualisation suite being used to monitor training [96]. The final

network architecture used is shown in figure 6.2; the 48×48 pixel input images are passed through a single convolutional layer with $48 5 \times 5$ filters; the output feature map is passed onto a pair of dense layers with 128, and 32 nodes respectively. Leaky rectified linear units are used as activation functions throughout the hidden layers [85]. These units are more computationally efficient than sigmoid like functions as well as providing a non-vanishing gradient for all inputs, avoiding saturation in learning. The output of the network is split into two branches; a three-way softmax function is used to constrain the joint probability for track, shower, and empty to sum to one, and a sigmoid function is used for the output of the Michel electron classifier. Finally, regularisation is achieved with the dropout algorithm [97]; in each iteration of the training weights have a probability p to be set to zero while the remaining weights are scaled by a factor $1/(1-p)$. With this approach, each training iteration uses only a random sample of the available nodes and as such nodes cannot co-adapt. The resulting network is a model average of each possible sub-network.

The network was trained using stochastic gradient descent (SGD) with the total loss being the weighted sum of the losses for the two output branches, $L_{tot} = 0.1 \cdot L_{tse} + L_m$, where the Michel classifier is given higher precedence due to the smaller training data set available for the Michel output. In order to speed up the learning process and converge on an optimal model, both the momentum and decay algorithms were used; momentum reduces oscillations of the weights during learning, while the decay of the learning rate allows for rapid learning during early stages of SGD and increased precision as the model converges [92]. Learning metrics were monitored during training using TensorBoard. The losses for each branch as well as the total loss for the validation data set are given in figure 6.3 as a function of the training epoch. The validation losses remain stable giving an indication that regularisation with dropout was successful in preventing overfitting of the training data. However, the validation set loss does not increase significantly after the first couple of epochs and so the training could have been terminated sooner with this network architecture. The final losses measured with the test data set are given in table 6.2.

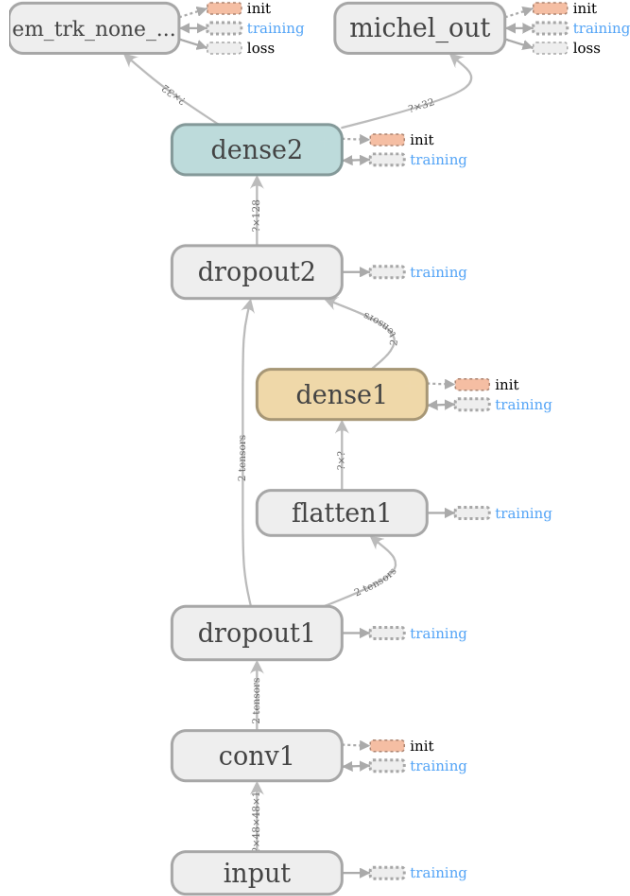


Figure 6.2: Network architecture used for hit classification, visualisation from the TensorBoard library.

Loss Type	L_{tot}	L_{tse}	L_m
Loss Value	0.033	0.155	0.017

Table 6.2: Test set losses after full training process.

6.3 Performance on ProtoDUNE–SP Simulation

The performance of the hit tagging was evaluated with reconstructed events in the ProtoDUNE–SP detector from the latest simulation samples; in the simulations, the detector was simulated under a number of different conditions, specifically including the space charge effect (SCE) [98] and excluding it. The hit tagging was trained on a part of the simulated data set which included the SCE and, as such, the samples

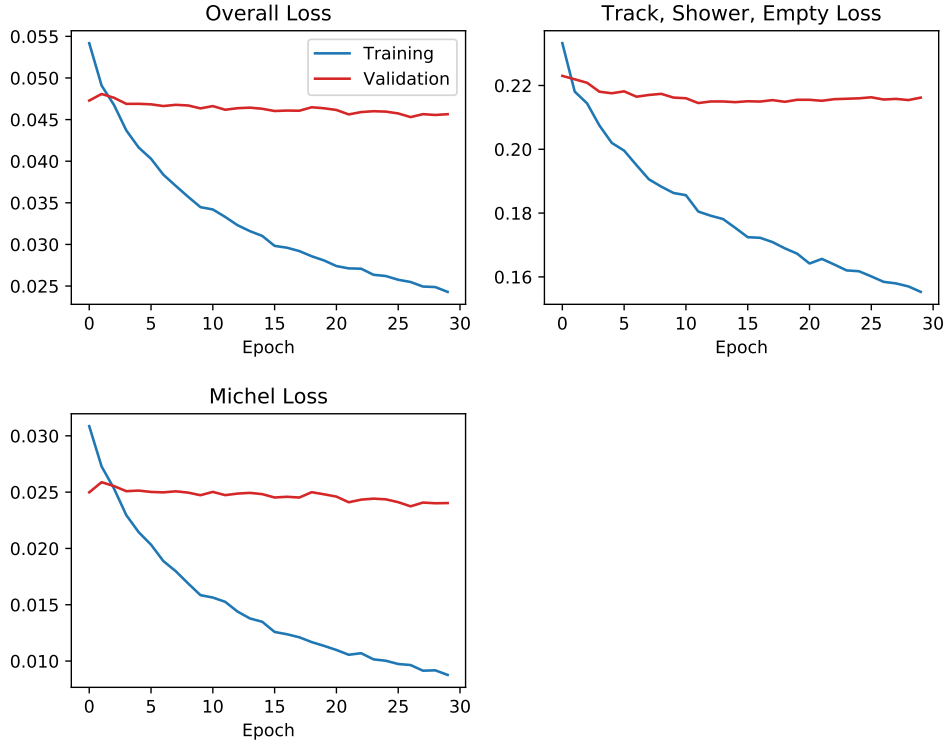


Figure 6.3: Evolution of the validation and training set losses during the training process.

without the SCE can be used as a validation that the network is robust to SCE differences between the simulations, and hence between the simulations and the data.

The distributions of the shower like classifier output for true shower hits and all other hits are given in figure 6.4; a strong separation between track and shower hits is observed. The shower classification threshold was optimised based on the F1 metric. This metric is defined as the harmonic mean of the precision and recall of a classifier and optimising with this score will ensure that both precision and recall will be high in the final classifier; for use cases where neither precision or recall is favoured, the F1 metric can be used to optimise for the best overall performance. The value of the F1 metric as a function of threshold is also shown in figure 6.4; the score peaks at a threshold of 0.72 with a value of 0.863 corresponding to a precision of 0.863 and a recall of 0.863.

Figure 6.5 gives the distributions of the Michel classifier output for true Michel electrons and all other hits. The large difference in sample size between the Michel electron and other hits in this sample means that despite high recall by the Michel

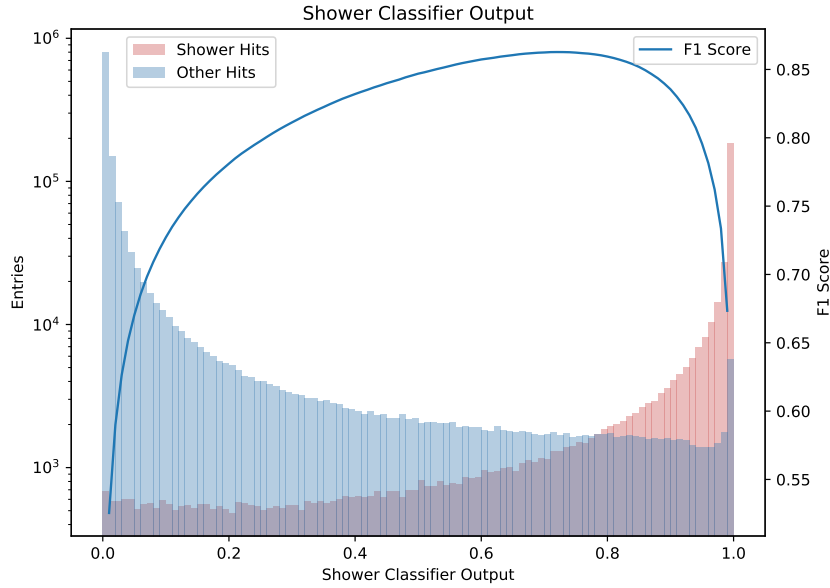


Figure 6.4: Shower classifier output distributions for true showers, and all other hits. Threshold optimisation was done using the F1 score metric which is also plotted.

electron classifier, low precision is achieved. In chapter 7 we will see that despite the low performance of the classifier for individual hits, a pure sample of Michel electron events can be selected by clustering hits with high Michel electron scores. This is due to the fact that the simple hit by hit classification test does not account for spatial correlations between Michel tagged hits.

Finally, the overall performance of each classifier was evaluated using the receiver operating characteristic (ROC) curve [99]; ROC curves are a test of the classification ability of a binary classifier. The curves show a comparison of the true positive rate and the false positive rate of the classifier as a function of the classification threshold chosen for the classifier. Figure 6.6 shows the ROC curves for the shower and Michel classifiers; the locations of these curves in the top left corner of the plots show that both have excellent performance as classifiers. In addition, the ROC curves show good agreement between the SCE on and SCE off data sets, showing that the classifiers are robust to changes in the SCE model should it differ between data and simulation. It is worth noting that the ROC curve only accounts for classification rates within each true sub-sample, it cannot account for the difference

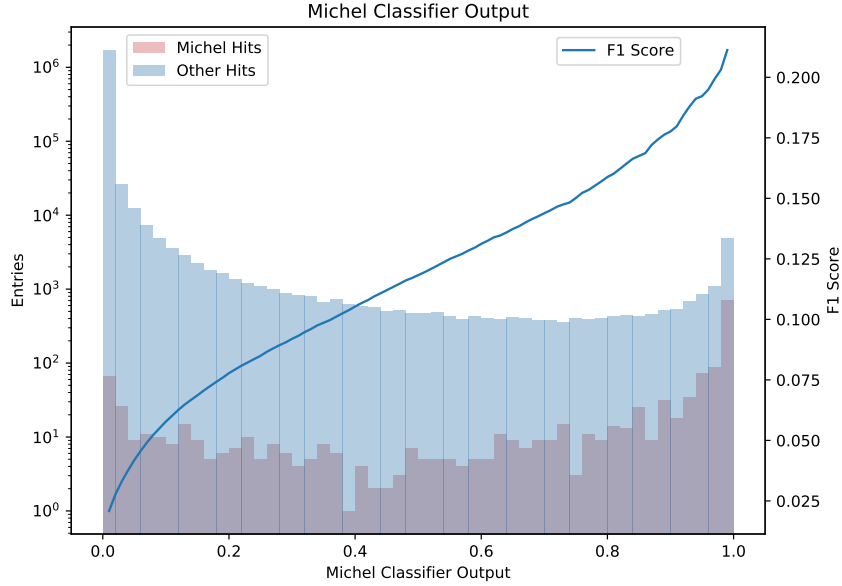


Figure 6.5: Michel classifier output distributions for true Michel electrons, and all other hits. Threshold optimisation was initially done with the F1 score metric, the threshold was modified when combined with a clustering algorithm, see chapter ??.

in sample size between the Michel electron sample and all other hits, and thus the ROC curve is a more instructive metric for the shower classifier where the size of the true and false samples are of a similar magnitude.

6.4 Validation and Performance on ProtoDUNE–SP Data

For validation on real ProtoDUNE–SP data two approaches were used: visual validation with event scans and cross validation with the output of the Pandora reconstruction framework [69]. Data from ProtoDUNE–SP run number 5387 was used for the validation; the data for this run was taken under stable operating conditions with a peak beam energy of 1 GeV.

Hand scans of the events show qualitatively that performance on the data is good. Figure 6.7 shows an example of the track like classification of hits in a real event. We can see that for hits along the tracks the classifier produces a large output score, and for shower like activity in the event the score is low, as we expect.

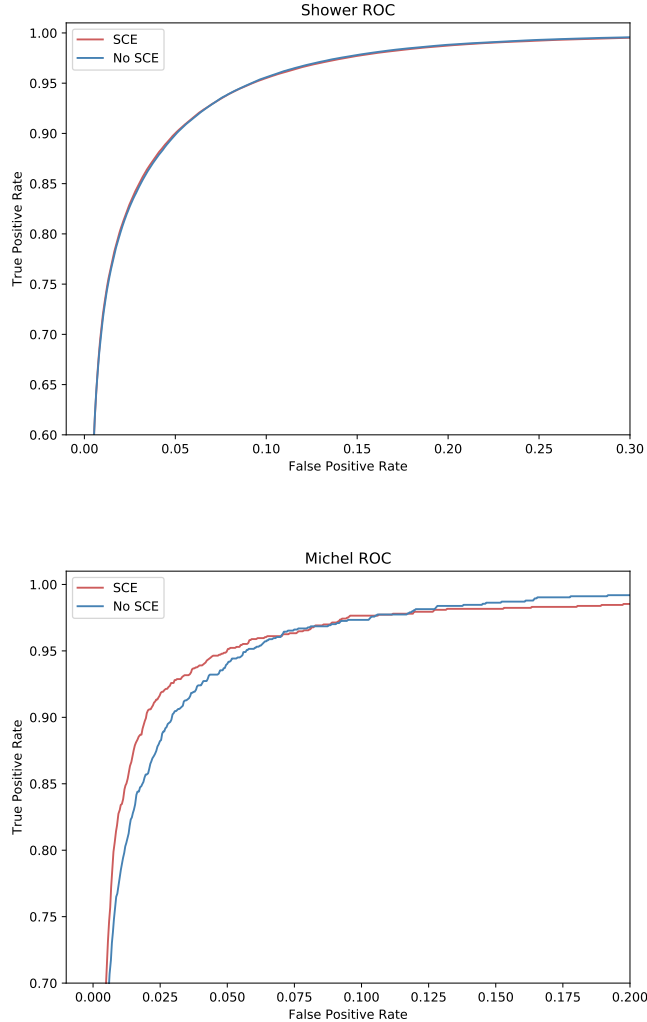


Figure 6.6: ROC curves for the shower (top), and Michel (bottom) classifiers. ROC curves for simulations including and excluding the SCE are included.

In particular the classifier is able to identify that hits which are adjacent to the track, delta rays, are from scattered electrons.

The Pandora reconstruction framework is the primary reconstruction used by the ProtoDUNE-SP experiment; for a more quantitative validation of the performance of the hit tagging algorithm, the hit tagging output can be compared to the reconstructed objects produced by Pandora. After the ProtoDUNE-SP data has been reconstructed, all of the reconstructed hits will have been clustered into either track or shower objects. As such the comparison of a hits CNN output with the type of reconstructed object it belongs to is a test of the agreement between the

CNN approach and the Pandora reconstruction algorithms. The Michel electron performance cannot be validated in this way due to a lack of tagged Michel electron objects in the Pandora output. Therefore, hand scanning of events is the primary validation of the Michel electron classifier and will be discussed in chapter 7.

The first test performed was the comparison of the CNN output distributions for hits in both Pandora tracks and Pandora showers, the corresponding distributions are given in figure 6.8 for both data and Monte Carlo; a strong correlation between the reconstructed Pandora objects and the associated CNN score can be seen in both cases, however the correlation is stronger in Monte Carlo than in data. The discrepancy between Pandora and the CNN is still being understood, differences between the data and simulations impact the performance of both algorithms. Figure 6.7 shows reconstructed hits labelled according to whether they agree or disagree with Pandora, we can see that for long tracks the agreement is good while smaller objects tend to disagree, with the CNN typically assigning a shower like classification but Pandora reconstructing them as a track. Work to understand the discrepancy between the CNN score and Pandora is ongoing.

This chapter has presented work on the development of a hit classification algorithm for LArTPCs based on CNNs; the performance of this approach for track–shower separation has been evaluated with ProtoDUNE–SP simulation and reconstruction, demonstrating good performance. This hit tagging framework is designed such that it can be utilised throughout the LArSoft reconstruction chain and is complementary to other reconstruction algorithms in the framework; chapter 7 will detail an example use of the hit tagging output: Michel electron event selection. Additional plans for this chapter are detailed below.

- Understand the difference between data and MC when comparing the CNN to Pandora.
- Test network robustness to other detector effects in simulation.
- Retrain networks with future simulations, including data driven models of detector effects.

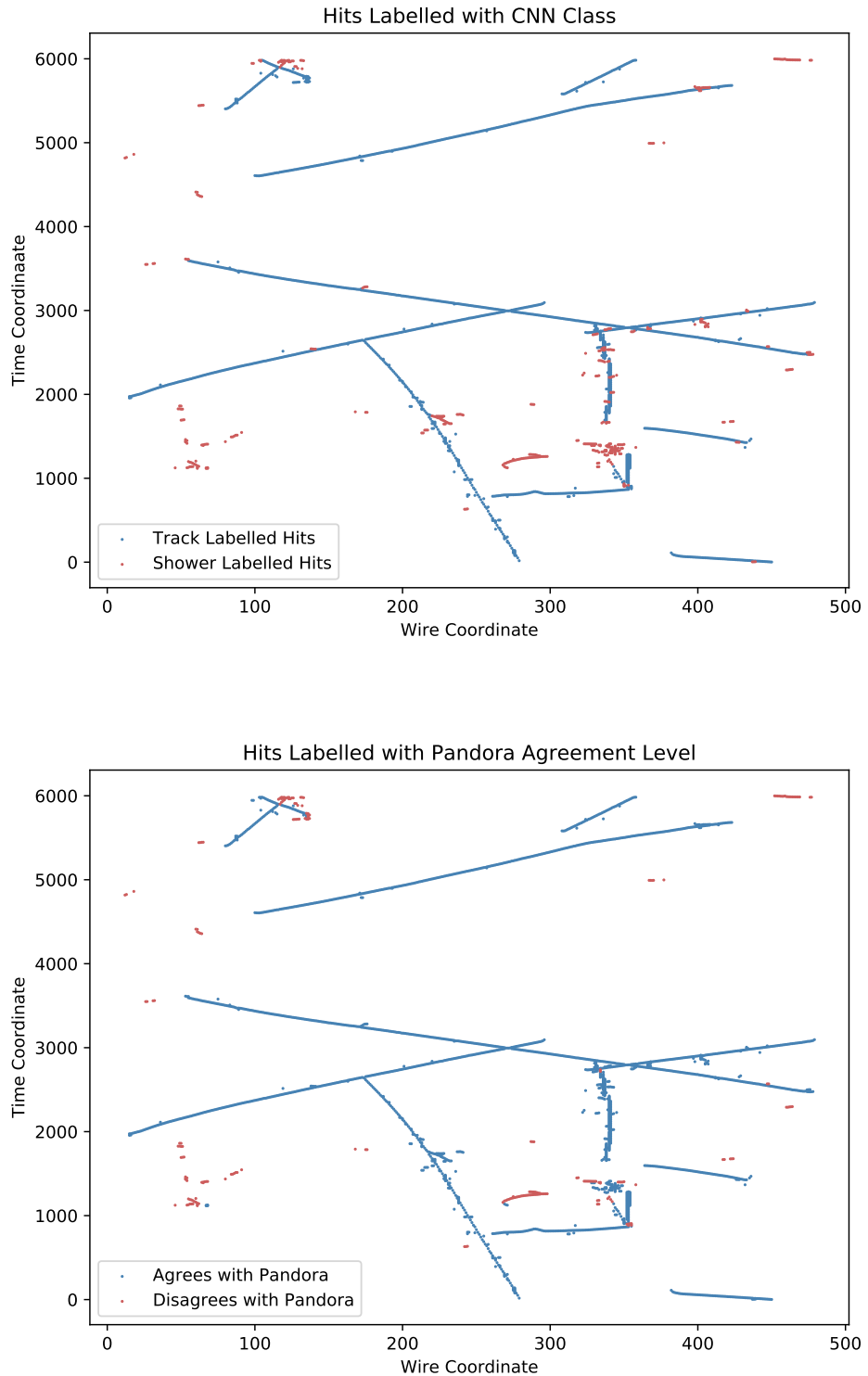


Figure 6.7: Reconstructed hits from ProtoDUNE-SP run number 5387 labelled with CNN classification (top), and Pandora agreement level (bottom).

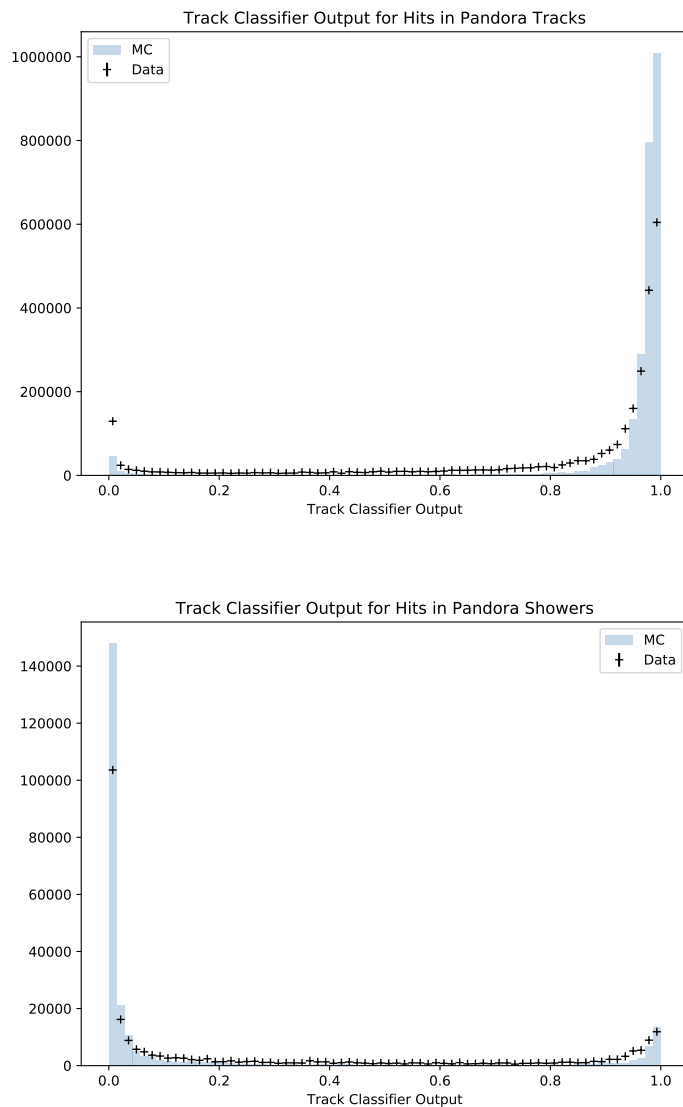


Figure 6.8: Output distributions for the track classifier on reconstructed Pandora objects.

7

Study of Michel Electrons in ProtoDUNE–SP

Contents

7.1	Michel Electrons in Liquid Argon	100
7.2	Michel Electron Event Selection	104
7.3	Michel Electron Energy Reconstruction	109
7.3.1	Michel Electron Hit Tagging with U-Nets	109
7.3.2	Michel Electron Reconstruction	111
7.4	Conclusions	122

Studying electrons in the tens of MeV energy range can provide valuable input into reconstruction techniques and energy uncertainty for the measurement of astrophysical neutrinos from supernova bursts. Understanding the response of LArTPC detectors to electrons in this range will be important for any large scale LArTPC experiment wishing to study supernova bursts. At these energies electron interactions have large contributions from both ionisation energy loss and radiative energy loss and therefore they have a unique signature which is neither track-like or shower-like. Low-energy electrons therefore require unique reconstruction algorithms to maximise the overall reconstruction performance. This chapter will discuss an approach to low-energy electron reconstruction in LArTPC detectors based on the use of convolutional neural networks and semantic segmentation.

Michel electron events from ProtoDUNE–SP will be used to test the performance of this technique and to provide an estimate of the energy uncertainty of LArTPC detectors for low-energy electrons.

[Chapter outline.](#)

7.1 Michel Electrons in Liquid Argon

Michel electrons are produced when a muon decays at rest. This decay gives rise to a characteristic energy spectrum which has a sharp cut-off at around 50 MeV, corresponding to half the muon mass. In matter it is also possible for μ^- to be captured on nuclei before they decay, this causes a broadening of the Michel electron spectrum for these events. A comparison of the Michel electron energy spectrum for free μ^+ and captured μ^- is given in Fig. 7.1. The capture process occurs roughly 70% of the time for negative muons in liquid argon and therefore in ProtoDUNE–SP the observed energy spectrum is a combination of the two processes in roughly equal quantities.

As discussed in chapter 4, the energy loss for electrons in liquid argon passes from an ionisation dominated regime to a radiation dominated regime in the tens of MeV region. The crossover point for this transition occurs at around 45 MeV, very close to the peak of the Michel electron spectrum. This leads to a unique signature for Michel electrons in liquid argon detectors, a short ($\sim 5\text{cm}$) track segment is surrounded by a number of small radiated energy deposits. Figure 7.2 shows an example of a Michel electron candidate from ProtoDUNE–SP data, along with labels of the key features.

One of the main challenges for Michel electron reconstruction in liquid argon is to successfully associate the radiated energy depositions back to the initial Michel electron once they have produced ionisation in the detector. Photons have a radiation length of around 20–30 cm in liquid argon which is many times larger than the size of the typical track-like part of the event, around 5 cm. Fig. 7.3a shows the spectrum of radiated photons from Michel electron events in ProtoDUNE–SP simulation alongside the photon multiplicity as a function of Michel electron

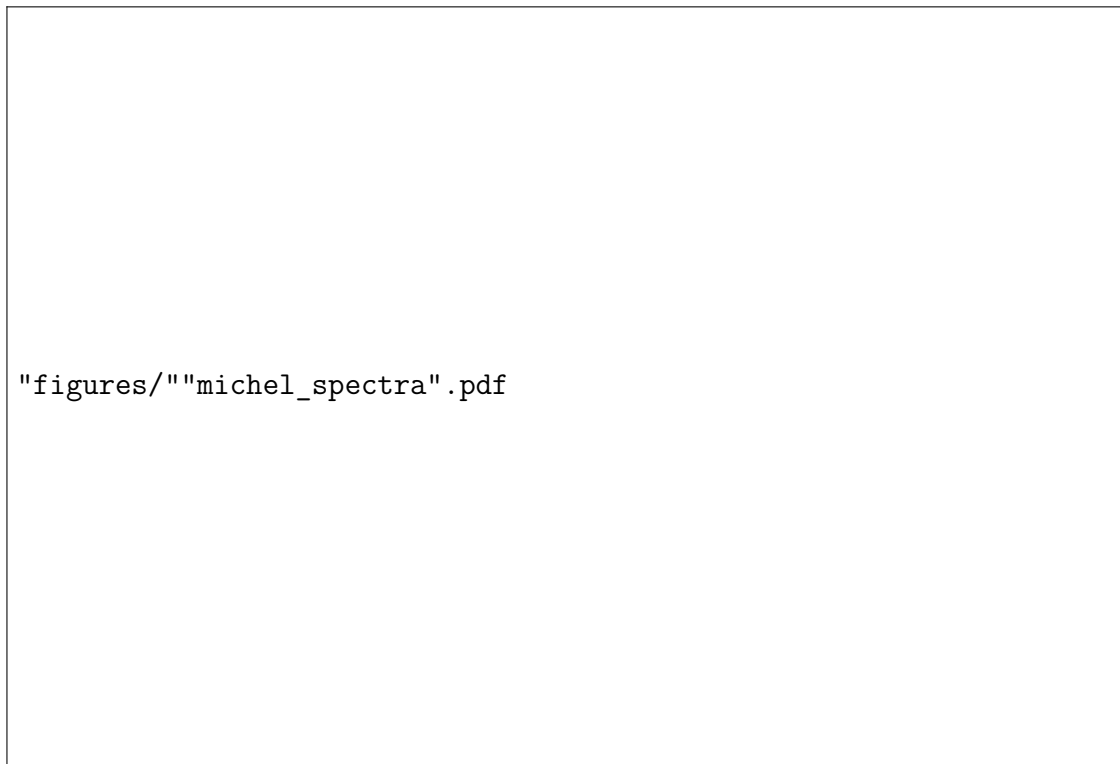


Figure 7.1: Michel electron energy spectra in liquid argon. (a) free muons. (b) muon capture at rest.

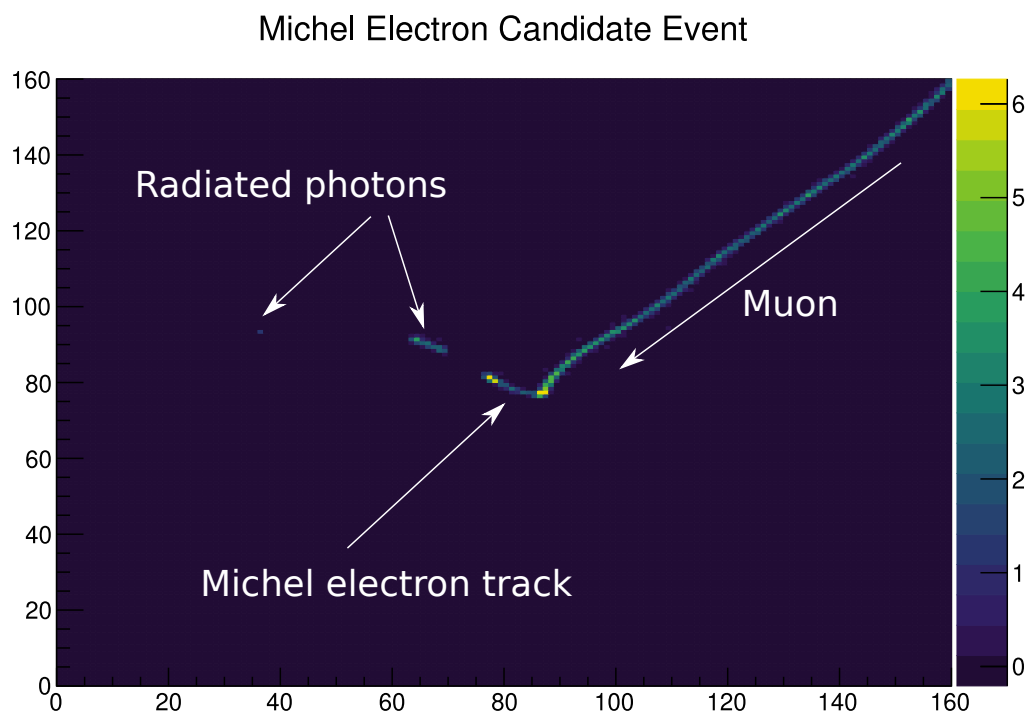


Figure 7.2: Michel electron candidate event from ProtoDUNE-SP data.

energy. While most of the radiated photons only carry a small fraction of the Michel electrons energy, in some cases a single radiated photon can carry a significant fraction of the electron energy. In addition, around the peak of the Michel electron spectrum (~ 45 MeV) there is a high photon multiplicity and a large spread in the multiplicity distribution. The combination of these effects leads to a significant spread in the fraction of radiated energy for Michel electron events.

Paragraph + figure on fraction of energy lost to radiation.

The energy which is lost into radiated photons is only visible once the photons interact in the argon to produce secondary electrons which then ionise the argon. These secondary electrons are scattered over large angles and distances in the detector when compared to the short Michel electron track, the spatial distribution of secondary electrons is shown in Fig. 7.4. TODO, analysis.

To highlight the impact of the radiated energy deposits we can consider the results of perfect energy reconstruction in two cases:

- Only considering the Michel electron track.
- Considering all ionisation energy within some radius and angle of the Michel electron track.

Fig. 7.5 illustrates the considerable increase in energy collected if radiated energy is considered, the distribution is significantly narrower and much more energy is recovered when considering the energy deposited within a cone of height 40cm and angle 30 ° of the Michel electron vertex. The average energy recovered is increased from TODO % to TODO % and the spread is reduced from TODO % to TODO %.

TODO, figure and paragraph for energy fraction vs radius.

The MC study presented here highlights the importance of radiated energy deposits in Michel electron and other low-energy electron events. Based on these results it is clear that to minimise energy uncertainties for these events it is important to maximise the amount of energy collected from radiated photons. The rest of this chapter will discuss an algorithm which was developed to tackle this problem, and its application on Michel electron events in ProtoDUNE-SP data.

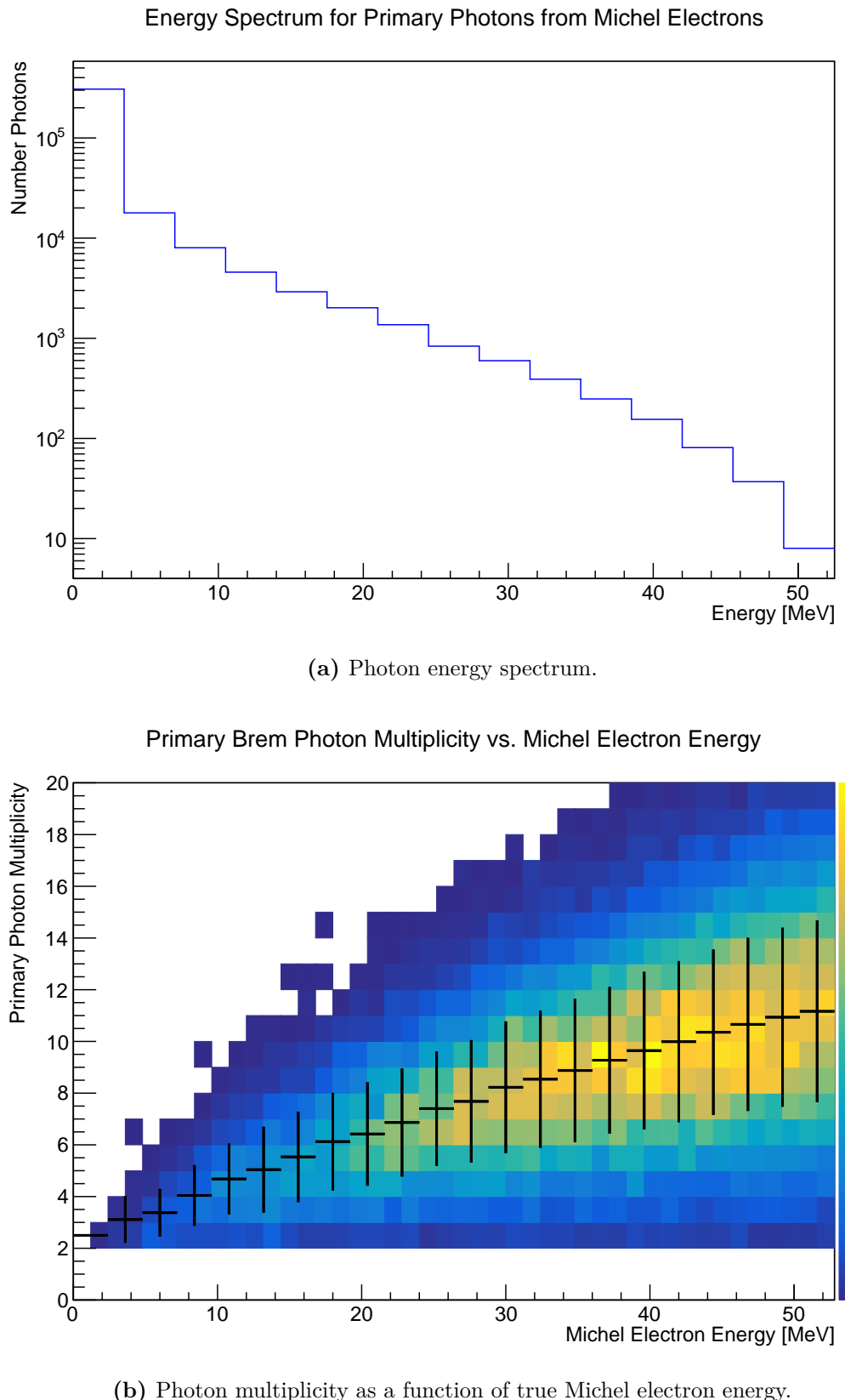


Figure 7.3: Properties of radiated energy deposits from Michel electrons in ProtoDUNE-SP simulation.

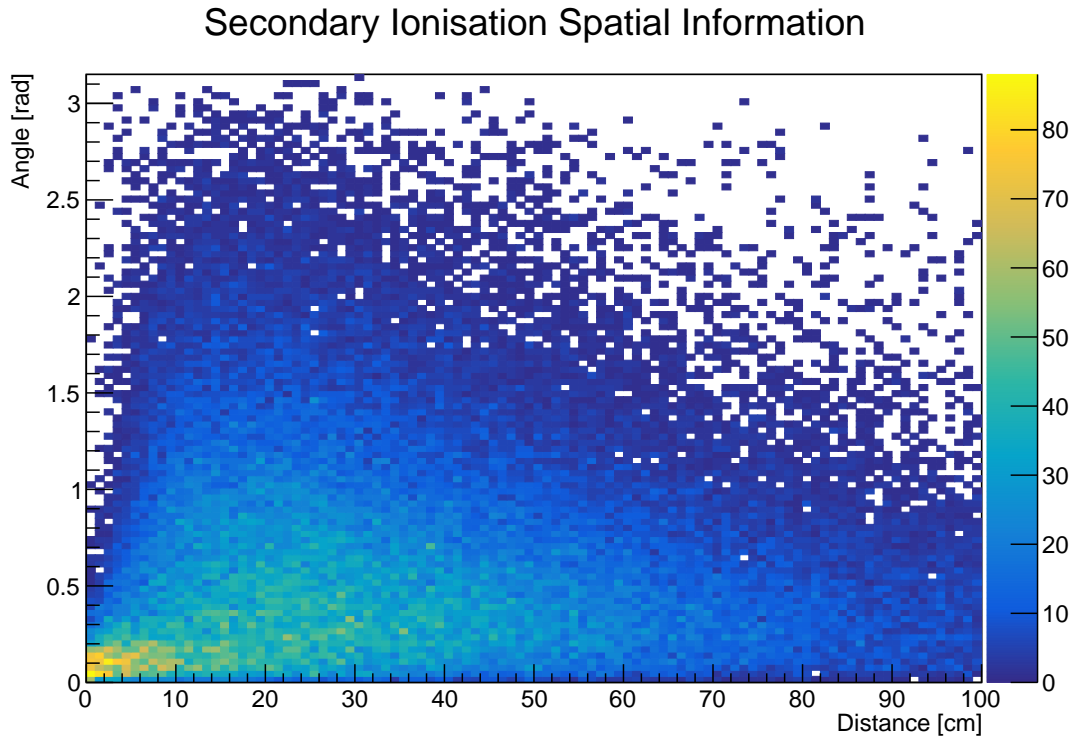


Figure 7.4: Spatial distribution of radiated ionisation deposits.

7.2 Michel Electron Event Selection

In order to select Michel electrons in ProtoDUNE-SP data, an event selection algorithm was developed based on combining the results from the hit tagging CNN from the previous chapter with clustering performed by the main ProtoDUNE-SP reconstruction framework, Pandora. The performance of the Michel electron classifier in isolation are discussed in the previous chapter.

The event selection algorithm proceeds in the following steps:

1. Start with all primary tracks from Pandora.
2. Define a set of Michel electron candidates from the list of all daughters of the track.
3. Find the best Michel electron candidate from the list of Michel electron candidates.

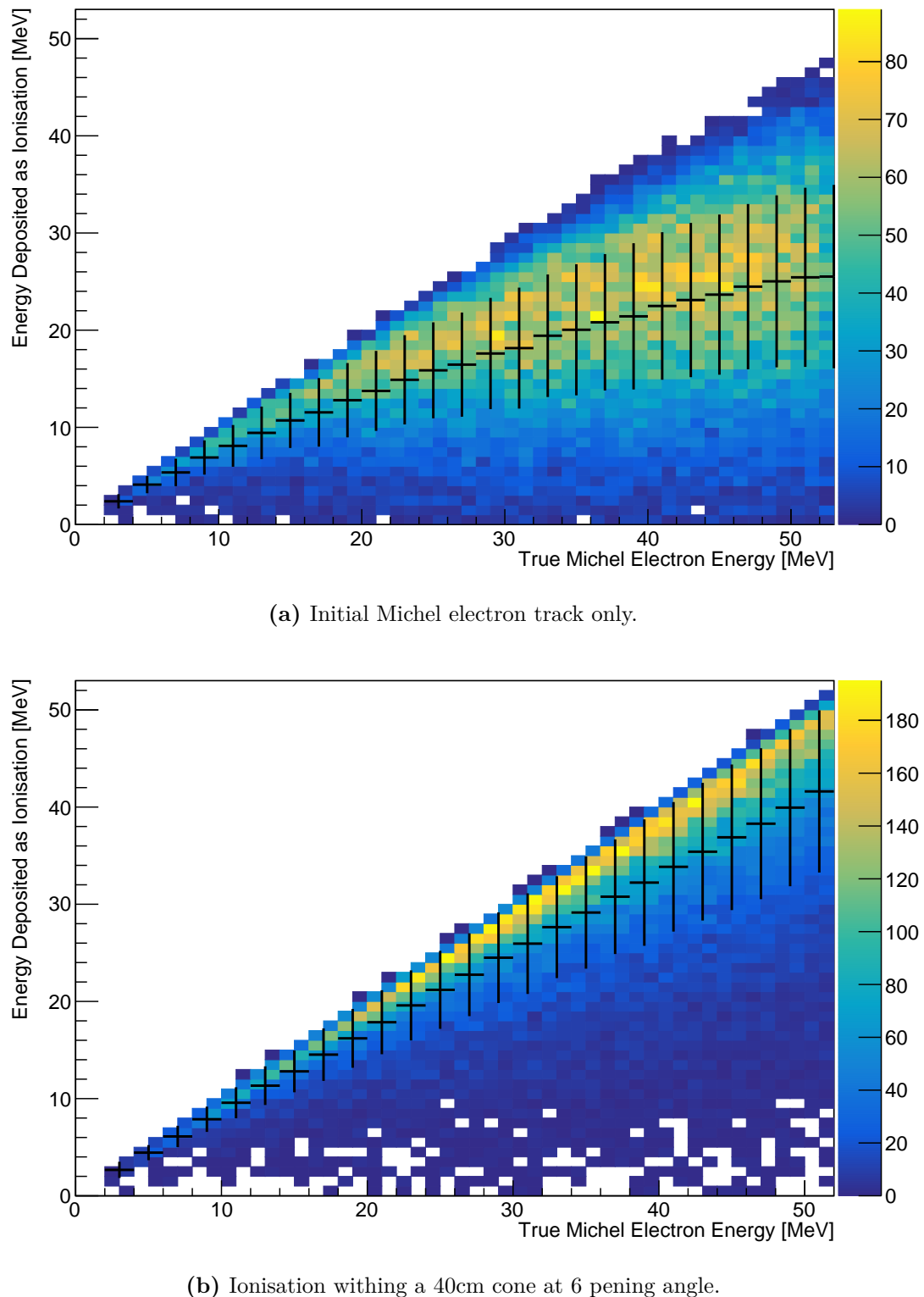


Figure 7.5: Available ionisation energy vs true Michel electron energy.

```
"figures/""frac_v_radius".pdf
```

Figure 7.6: Fraction of Michel electron energy collected vs collection radius.

4. Select events where the best Michel electron candidate passes the event selection cuts.

In the first step the initial sample of muon candidates is defined. All tracks from the Pandora reconstruction chain which have been labelled as primary tracks are considered.

The second step defines a set of Michel electron candidates for each track in the sample. A Michel electron candidate is any daughter of the primary Pandora track which satisfies the following conditions:

- Starts within 5 cm of the primary track endpoint.
- Contains a minimum of 5 hits on the collection plane.

In the third step the Michel electron candidates are analysed in order to define the best Michel electron candidate for each track. The best Michel electron candidate is the Michel electron candidate with the largest fraction of Michel-like hits based

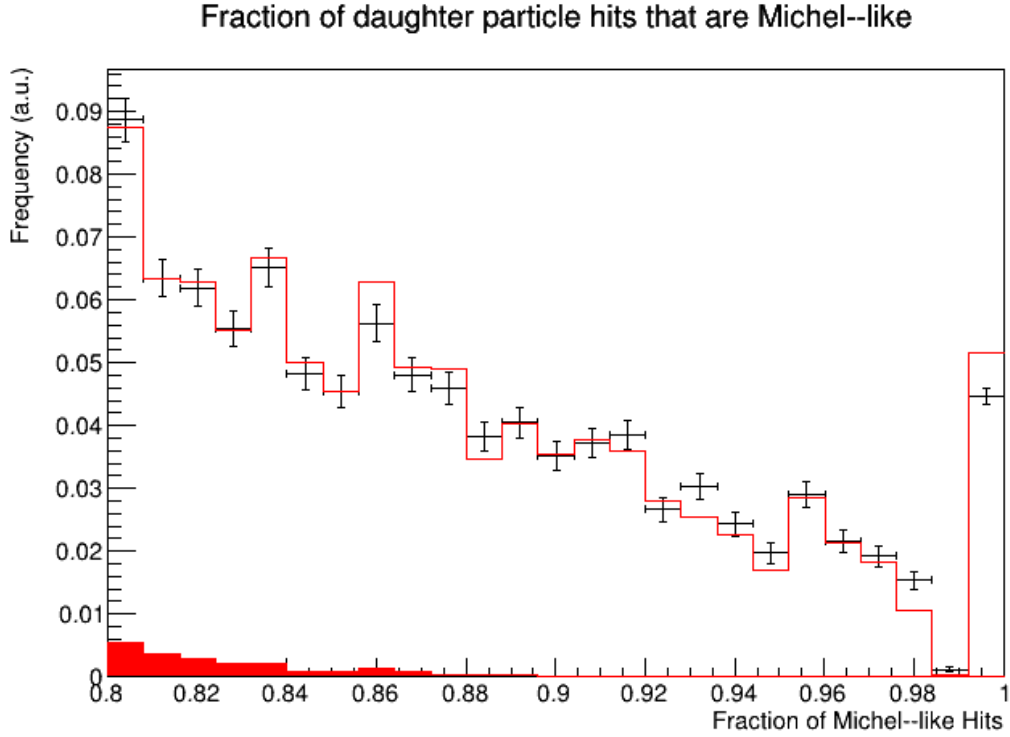


Figure 7.7: Fraction of Michel–like hits in the best Michel electron candidate.

on the output of the Michel electron score from the CNN with a threshold of 0.9.

In the case of a tie the Michel electron candidate with the most hits is chosen.

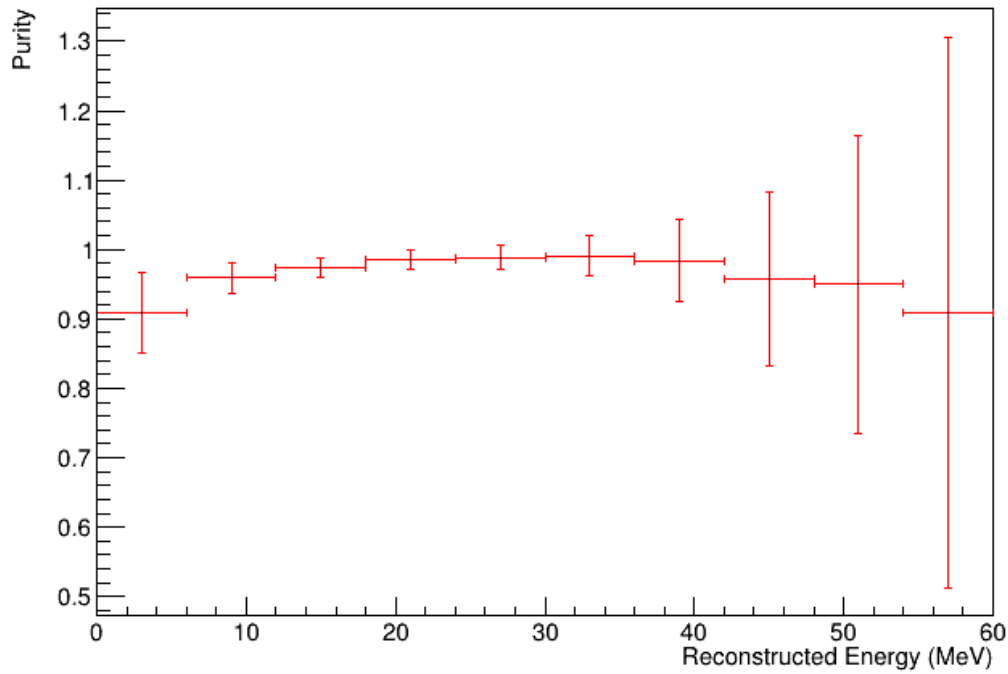
The fourth step is the final decision, which is based on the fraction of Michel like hits in the best Michel electron candidate. Figure 7.7 shows a comparison of the fraction of Michel–like hits for the best Michel electron candidate in ProtoDUNE–SP data and simulation. [TODO, analysis of fig.](#) Events are selected if the best Michel electron candidate is made up of more than 80 % of Michel–like hits then it is selected as a Michel electron candidate.

Based on this algorithm Michel electron events are selected with an average purity of [TODO %](#) and an average efficiency of [TODO %](#) in ProtoDUNE–SP simulation. Figure 7.8 shows the distribution of event selection efficiency and purity as a function on Michel electron energy. [TODO, analysis and figure.](#)

[TODO, muon kinematic distributions.](#)

```
"figures/""eff_v_energy".pdf
```

(a) Purity vs True Michel electron energy.

Event Selection Purity vs Reconstructed Energy

(b) Efficiency vs True Michel electron energy.

Figure 7.8: Purity and efficiency of Michel electron event selection as a function of energy.

7.3 Michel Electron Energy Reconstruction

To reconstruct the energy of Michel electrons in liquid argon the relevant hits must first be selected. Once the hits are selected the ionisation energy deposited by each hit is then reconstructed, the reconstructed energy of the Michel electron is the sum of the reconstructed energy of all relevant hits. In this section we will detail a hit selection algorithm based on a type of convolutional neural network called a U-Net, which returns hit selection maps for the Michel electron energy reconstruction. This algorithm is used to select Michel electron hits with a high purity and efficiency, the resulting reconstructed energy spectrum is used to estimate the energy resolution of ProtoDUNE-SP for electrons in the tens of MeV range.

7.3.1 Michel Electron Hit Tagging with U-Nets

A U-Net is a type of convolutional neural network which is designed to perform semantic segmentation of images [TODO]. In semantic segmentation the goal of the network is to return a map of pixels which correspond to the areas of interest; the output of the network is the same dimension as the input with a one-to-one correspondence between input pixels and output pixels. The architecture used for the hit selection algorithm is shown in Fig. 7.9. During the first half of the network architecture the resolution of the output is decreases, this is analogous to many conventional CNN's and during this phase the network learns about the content of the image. The second phase of the architecture allows the U-Net to rebuild the locations of different features within the initial image, this is achieved by passing the details of previous layers to the network as the resolution of the output map is slowly increased back to the original resolution [TODO].

TODO: improve the architecture description.

In the Michel electron case, the goal of the network is to return a map of all ionisation energy deposits which come from the Michel electron, this includes the initial track and any secondary deposits from radiated photons. The inputs and outputs are two dimensional images of the location of reconstructed hits centered on the selected Michel electron. The amplitude of each input pixel is given by

the integrated charge of any reconstructed hits within the pixel. For the outputs the pixels have an amplitude of 1 if they contain a Michel electron hit, and 0 otherwise. Only data from the collection plane is used because there is a higher signal to noise ratio on these wires.

Intersection-over-union was used as the loss function for the U-Net. This loss is defined as

$$\text{IOU}(A, B) = \frac{|A \cap B|}{|A \cup B|} \quad (7.1)$$

where A is the set of all selected hits, and B is the set of all true hits. This loss rewards the network for selecting as many correct hits as possible (high intersection), while penalising it for selecting more hits than it needs to (high union). The IOU score lies between 0 and 1, with a score of 1 corresponding to a perfect match between the two sets and therefore perfect hit tagging in our Michel electron case.

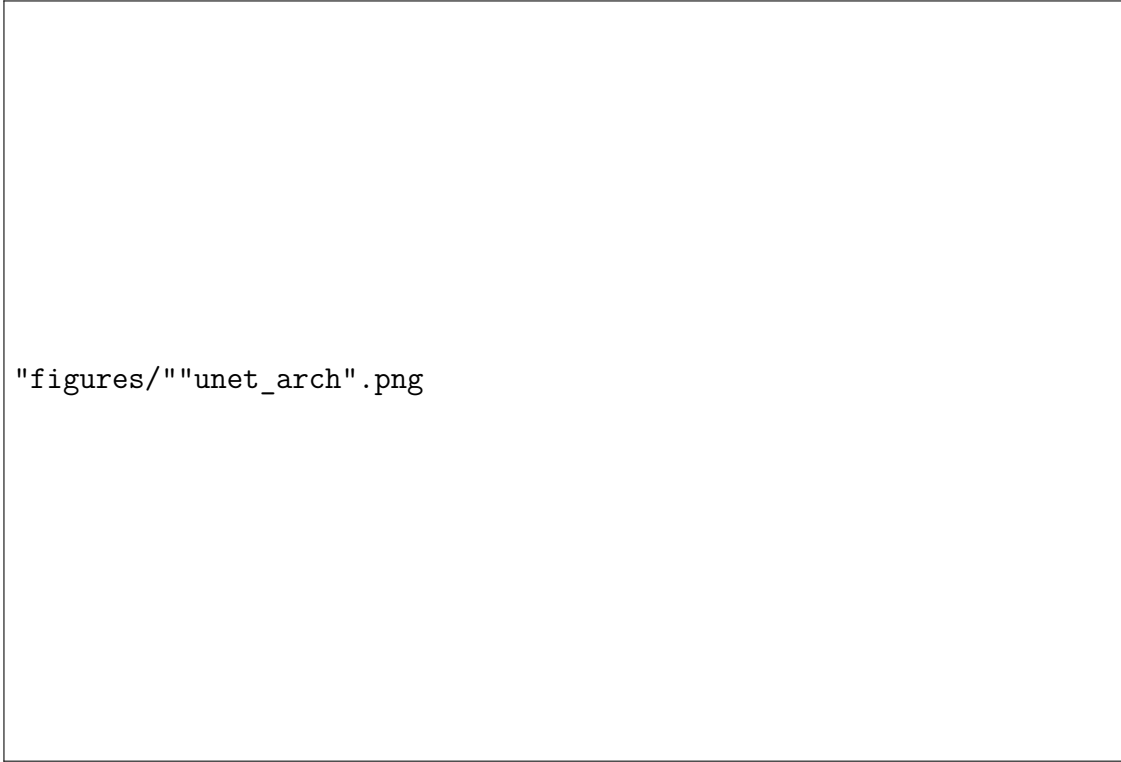
The network architecture used for the Michel electron reconstruction is shown in Figure 7.9. The network consists of a repeating structure which contains the following key components:

- Convolutional layers in the form of inception units.
- Pooling layers for downscaling.
- Residual connections and up-sampling.

FIXME. Description. As with the hit tagging CNN from the previous chapter, both dropout and early-stopping are implemented to prevent over-fitting.

The datasets for the training process were generated from a full simulation of the ProtoDUNE-SP detector under beam operation including both cosmic ray and beam particles. The images produced contain the location and integrated charge for each hit within the image window. The training data is split into training, test, and validation sets in the ratio 80:10:10. In total around 40,000,000 images were generated for the training stage.

As with the hit tagging CNN from the previous chapter, the training and validation scores were monitored throughout training using TensorFlow. The



"figures/""unet_arch".png

Figure 7.9: CNN architecture used to select ionisation energy deposits.

weights of the network were saved after each epoch, and the final weights were those from the epoch before the epoch when the validation score first decreased. Figure 7.10 shows the evolution of the loss over time, along with a vertical line representing the loss at which the weights were chosen.

A demonstration of the output of the U-Net is given in Figure 7.11 which shows the input, output, and truth images for an event from ProtoDUNE-SP simulation.

7.3.2 Michel Electron Reconstruction

Michel electron reconstruction was evaluated on a dataset which was part of the same batch of simulation as the training, test, and validation data, but distinct from all of them.

7.3.2.1 Hit Selection

The U-Net produces a sharply peaked output distribution in both data and simulation as seen in Figure 7.12, which shows sharp peaks in the distribution

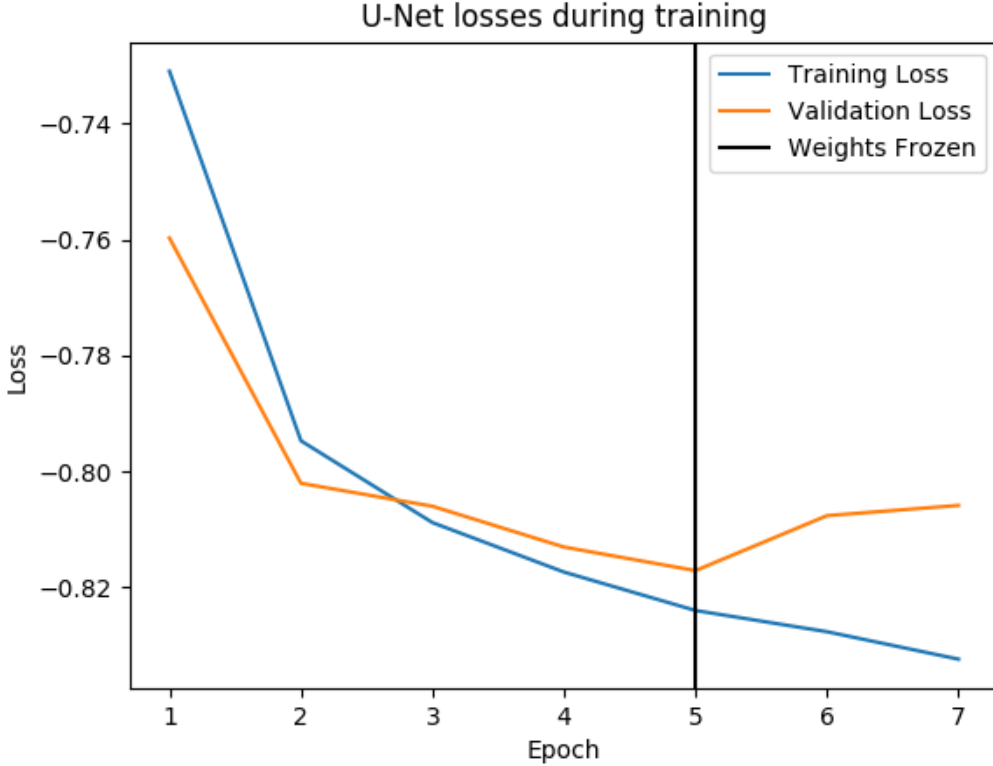


Figure 7.10: U-Net training and validation loss as a function of epoch.

at 0 and 1. The distribution has slightly sharper peaks in simulation as with seen with the hit tagging CNN from the previous chapter, this is unsurprising due to the fact that the simulation does not perfectly match the data. TODO.

Is there a good way to mitigate this?

Hits from the input images are selected as Michel electron hits if their score exceed a selection threshold of 0.9. The number of hits selected per event for data and simulation is shown in figure 7.13. Around 10 hits are selected on average per event, with a slightly larger spread in data than in simulation.

The performance of the hit tagging algorithm was analysed with the simulated sample. The U-Net output distribution for true Michel electron hits and falsely tagged hits is shown in Figure 7.14, along with a ratio of the true and false hits as a function of energy. The ratio shows a strong separation between true hits and false hits, which appear at high scores and low scores respectively.

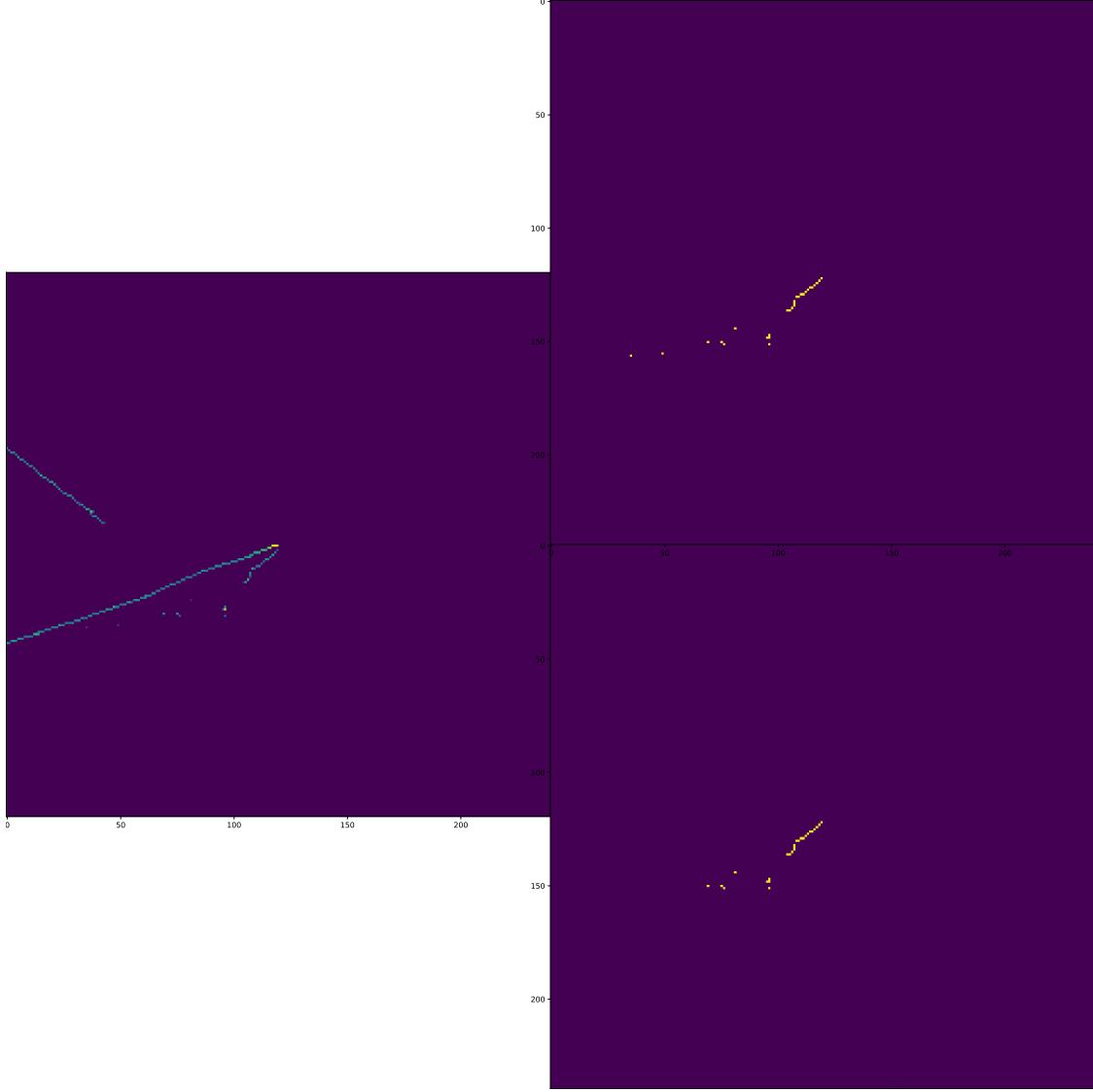


Figure 7.11: Example input, true output, and prediction images for U-Net. Left: Input image. Top Right: True Output. Bottom Right: U-Net Prediction.

Based on the score distributions for true and false hits the precision and completeness of the hit tagging algorithm can be evaluated. The precision and completeness are defined as

$$\text{Precision} = \frac{N_{TP}}{N_{TP} + N_{FP}} \quad (7.2)$$

$$\text{Completeness} = \frac{N_{TP}}{N_{TP} + N_{FN}} \quad (7.3)$$

where N_{TP} , N_{FP} , and N_{FN} are the number of true-positive, false-positive, and false-negative hits respectively. These parameters give a quantitative evaluation

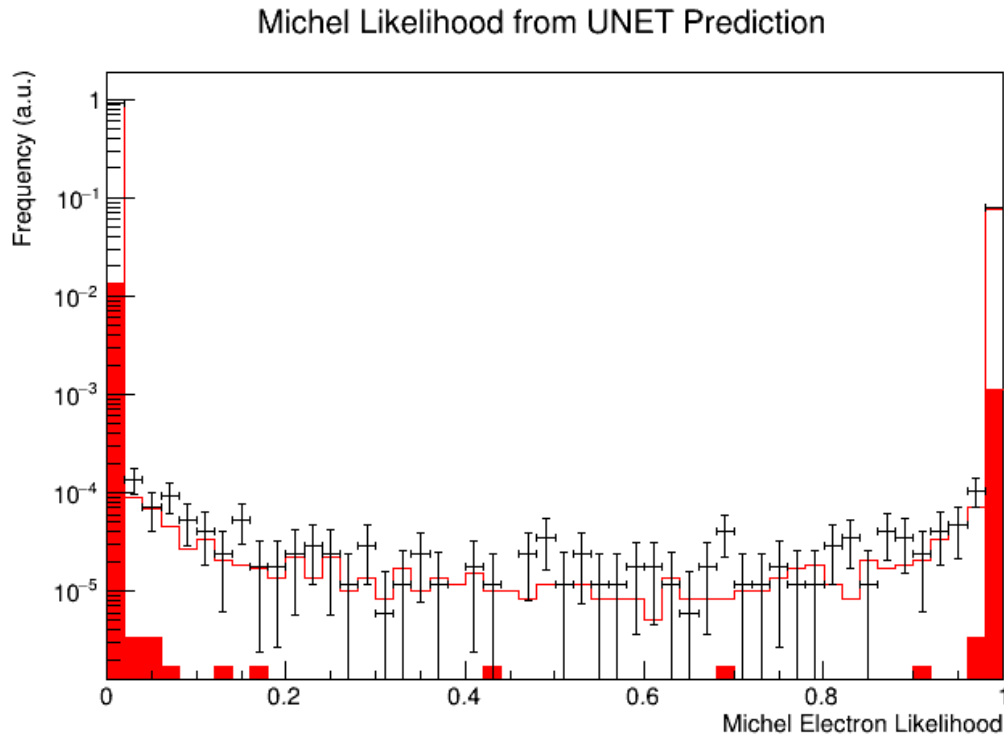


Figure 7.12: U-Net Predicted Distribution.

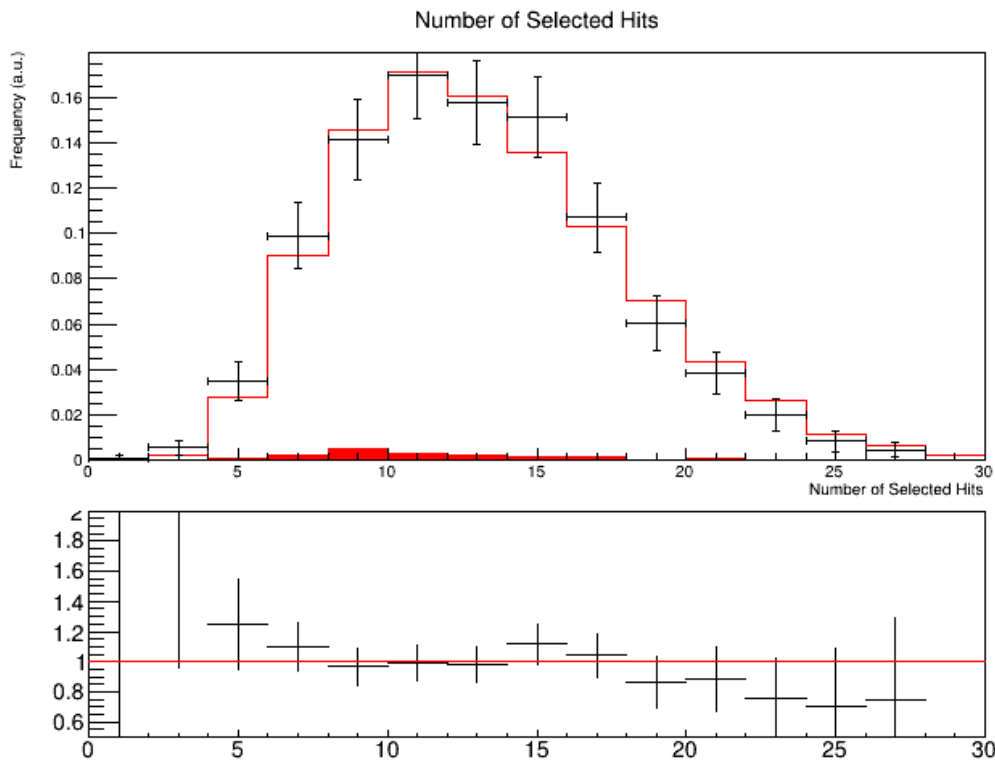


Figure 7.13: Number of hits in Michel electron events.

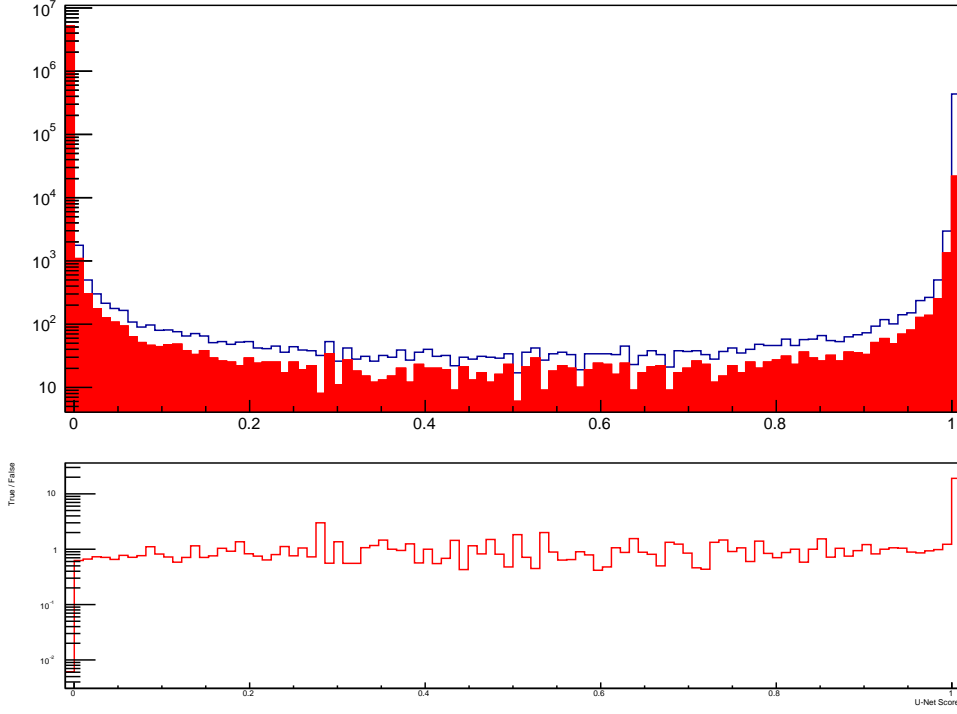


Figure 7.14: U-Net output distribution.

of the performance of the hit tagging algorithm, allowing for comparison between different algorithms. The purity and completeness of the hit tagging was calculated for a range of selection thresholds in the range $[10^{-7}, 1 - 10^{-7}]$, Figure 7.15 shows the purity against completeness for the values in this range. The hit tagging algorithm produces a high precision and completeness throughout range of thresholds, however the steepness of the distributions means that the choice of threshold makes little difference to the performance meaning that little can be done to optimise the performance by varying the threshold.

7.3.2.2 Ionisation Energy Reconstruction

The total ionisation energy is reconstructed by summing the hit-by-hit ionisation energy for all hits selected by the U-Net. The ionisation energy for each hit is reconstructed from the hit integral in ADC as

$$E_{hit} = \frac{I_{hit} \times C_X \times C_{YZ} \times N \times W_{ion}}{C \times R}, \quad (7.4)$$

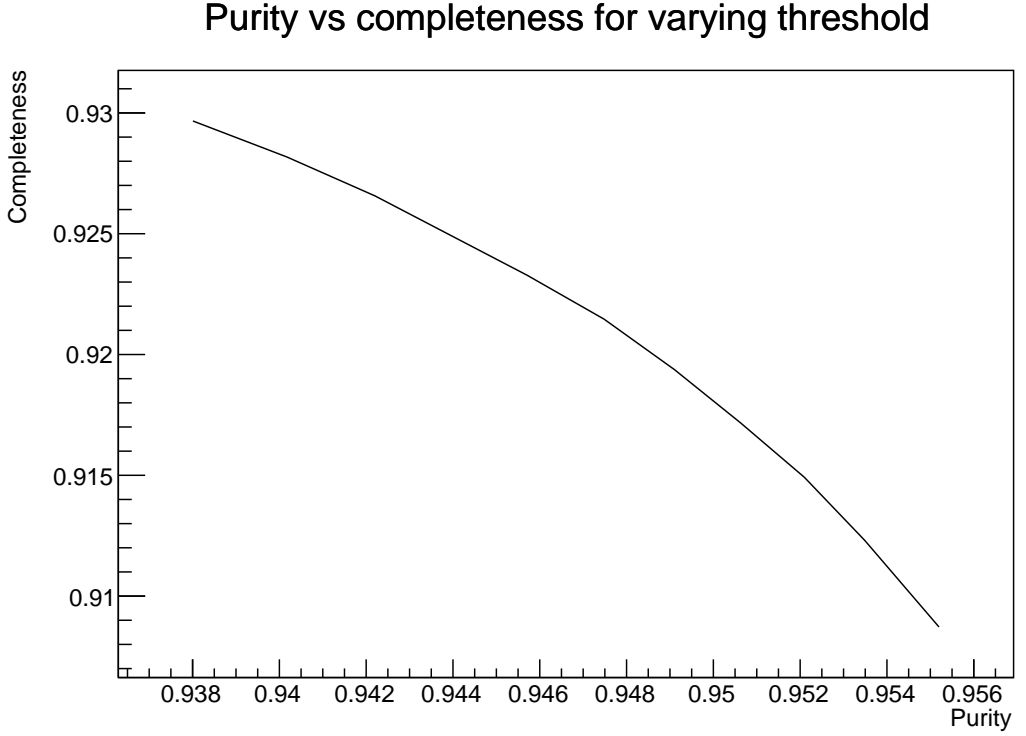


Figure 7.15: U-Net purity vs completeness.

where E_{hit} is the reconstructed hit energy in MeV, I_{hit} is the integrated hit charge in ADC, C_X is the X-correction factor which is dependent on the X coordinate of the hit within the TPC, C_{YZ} is the YZ-correction factor which is dependent on the Y and Z coordinates of the hit within the TPC, N is a dimensionless normalisation factor which normalises the data and MC distributions to give the same magnitude, W_{ion} is the ionisation energy of argon in MeV per electron, C is a constant conversion factor which has units ADC per electron, and R is the recombination factor. The distribution of reconstructed hit energies in ProtoDUNE-SP data and simulation is shown in Figure 7.16.

The position dependent calibration matrices correct for non-uniformity in the detector response across the TPC. In the X direction the main contributing factors are attenuation due to electron absorption, and variations in the electron drift velocity due to space charge effects. The main contributing factor for the YZ-correction matrix is wire-to-wire response variations.

As discussed in chapter 4 the recombination factor is a $\frac{dE}{dx}$ dependent factor

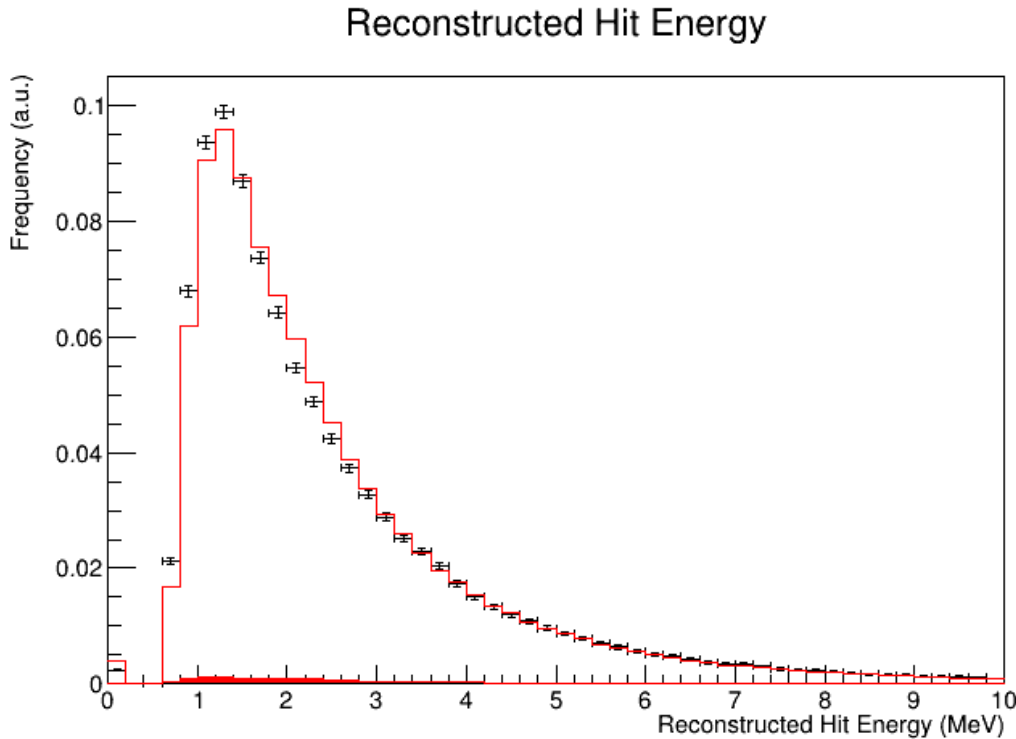


Figure 7.16: Reconstructed Hit Ionisation Energy

which depends on the conditions in the liquid argon. Due to the shortness of Michel electron tracks and the other charge deposits it is challenging to assign $\frac{dE}{dx}$ on a hit-by-hit basis for this sample, therefore, an average recombination factor is used for all hits. The recombination factor is calculated using the box model [TODO] under ProtoDUNE-SP operating conditions to be 0.69.

The reconstructed ionisation energy spectrum from Michel electron candidates is shown in Figure 7.17 along with the average ionisation energy per hit. The distribution peaks at around 18 MeV and has a tail up to just under 50 MeV.

TODO: analysis of ionisation reconstruction performance.

TODO: Energy resolution fits vs energy.

7.3.2.3 Michel Electron Energy Reconstruction

The true Michel electron energy includes contributions from scintillation light as well as radiated ionisation energy which is not contained within the images used in reconstruction. To estimate the total Michel electron energy the reconstructed

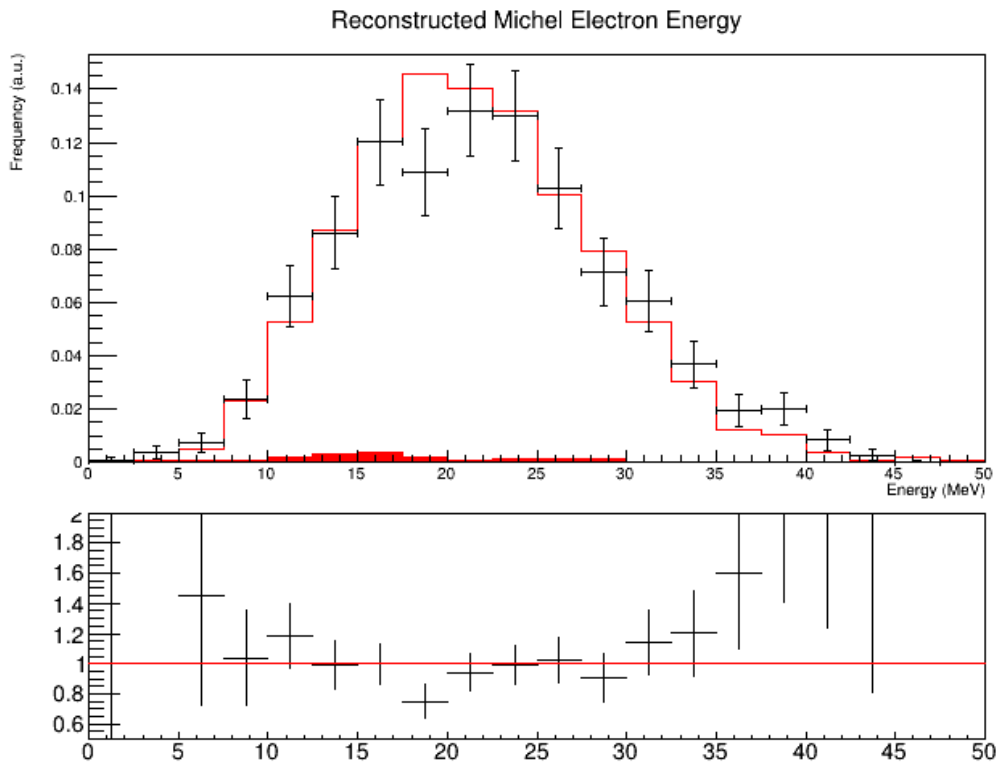


Figure 7.17: Reconstructed Michel Electron Ionisation Energy

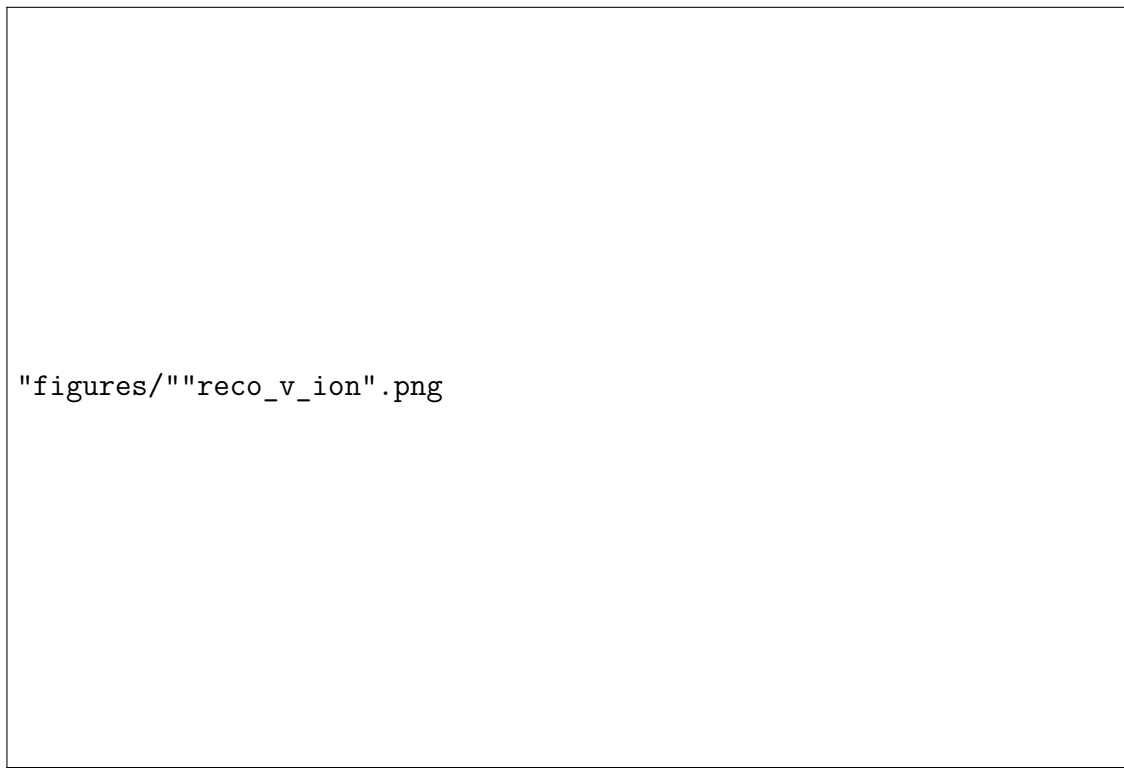


Figure 7.18: Reconstructed Ionisation vs True Ionisation.

```
"figures/""frac_diff_v_ion".png
```

Figure 7.19: Fractional energy difference between reconstructed and true Michel electron energy.

```
"figures/""res_bias_v_ion".png
```

Figure 7.20: Energy resolution and bias as a function of true ionisation energy.

ionisation energy needs to be scaled to account for these losses. As shown in Figure 7.5 there is a none-linear correlation between the true Michel electron energy and the available ionisation energy in reconstruction, therefore, a quadratic energy scaling factor was used to convert the reconstructed ionisation energy into a reconstructed Michel electron energy.

The energy scaling factor was estimated by fitting the reconstructed ionisation energy as a function of true Michel electron energy in ProtoDUNE-SP simulation with a quadratic correction as shown in Figure 7.21. This quadratic is then inverted to give the reconstructed Michel electron energy for a given reconstructed ionisation energy,

$$E_{michel} = \left(\frac{E_{ion}}{a} - d \right)^{\frac{1}{2}} - \frac{b}{2a}, \quad d = \frac{c}{a} - \left(\frac{b}{2a} \right)^2 \quad (7.5)$$

where E_{michel} is the reconstructed Michel electron energy, E_{ion} is the reconstructed ionisation energy, and a, b, and c are the parameters from the quadratic fit. The fit gives

$$a = TODO, \quad (7.6)$$

$$b = TODO, \quad (7.7)$$

$$c = TODO. \quad (7.8)$$

The reconstructed Michel electron energy spectrum is shown in Figure 7.22, alongside the true Michel electron energy spectrum from the simulation. There is a significant difference in the shape of the two spectra, this is due to the significant energy loss to scintillation and radiation that cannot be collected in ProtoDUNE-SP due to challenges in the reconstruction.

TODO: Energy resolution fits vs energy.

The energy uncertainty and bias are estimated by fitting the fractional energy difference between the reconstructed and true Michel electron energies as a function of true Michel electron energy. The fractional energy difference, defined as

$$\Delta = \frac{E_{reco} - E_{true}}{E_{true}}, \quad (7.9)$$

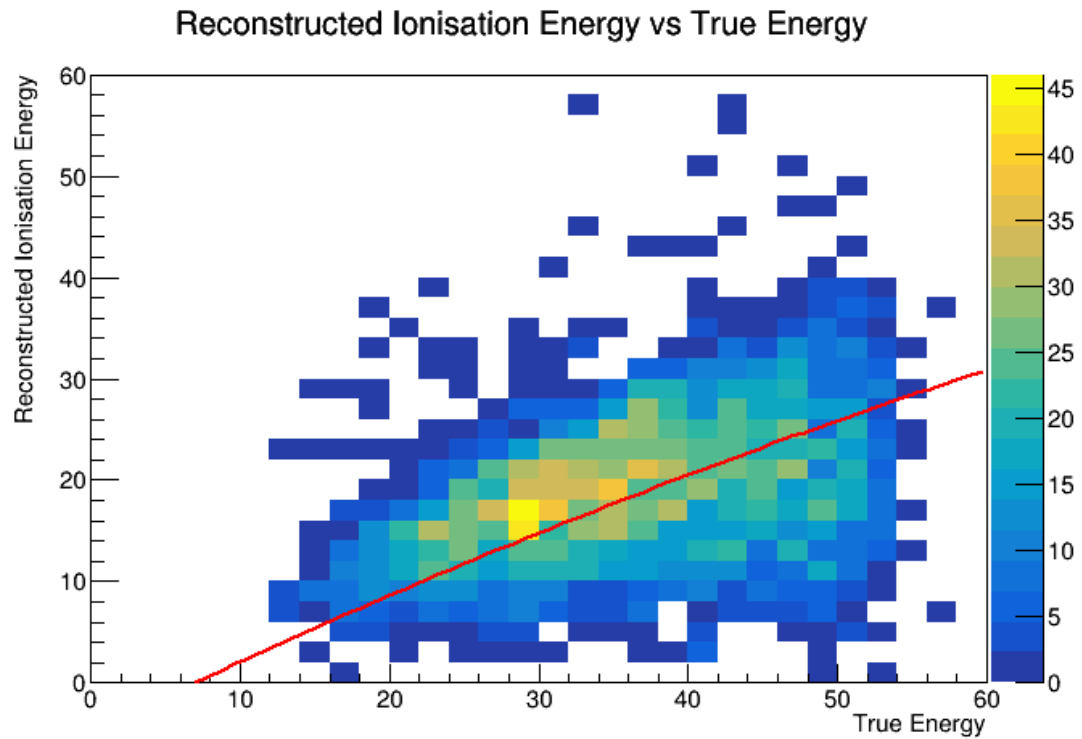


Figure 7.21: Quadratic Energy Scale Factor.

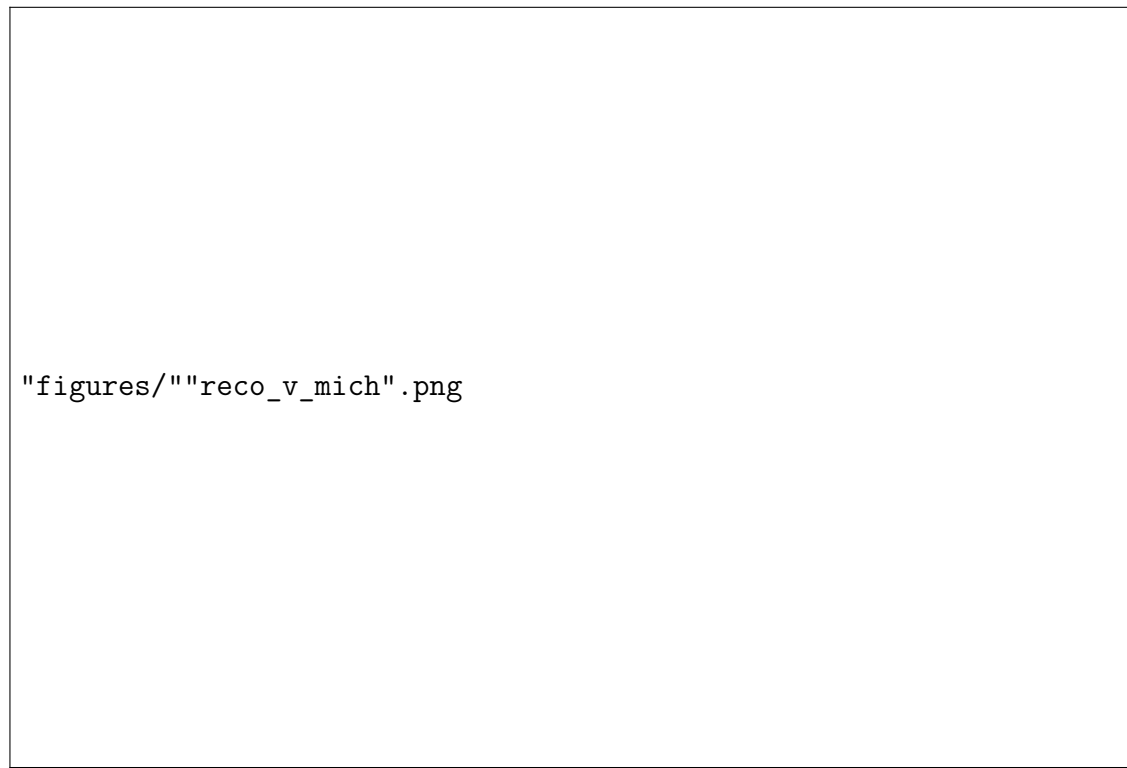


Figure 7.22: Reconstructed Energy vs True Michel Electron Energy.

```
"figures/""frac_diff_v_energy".png
```

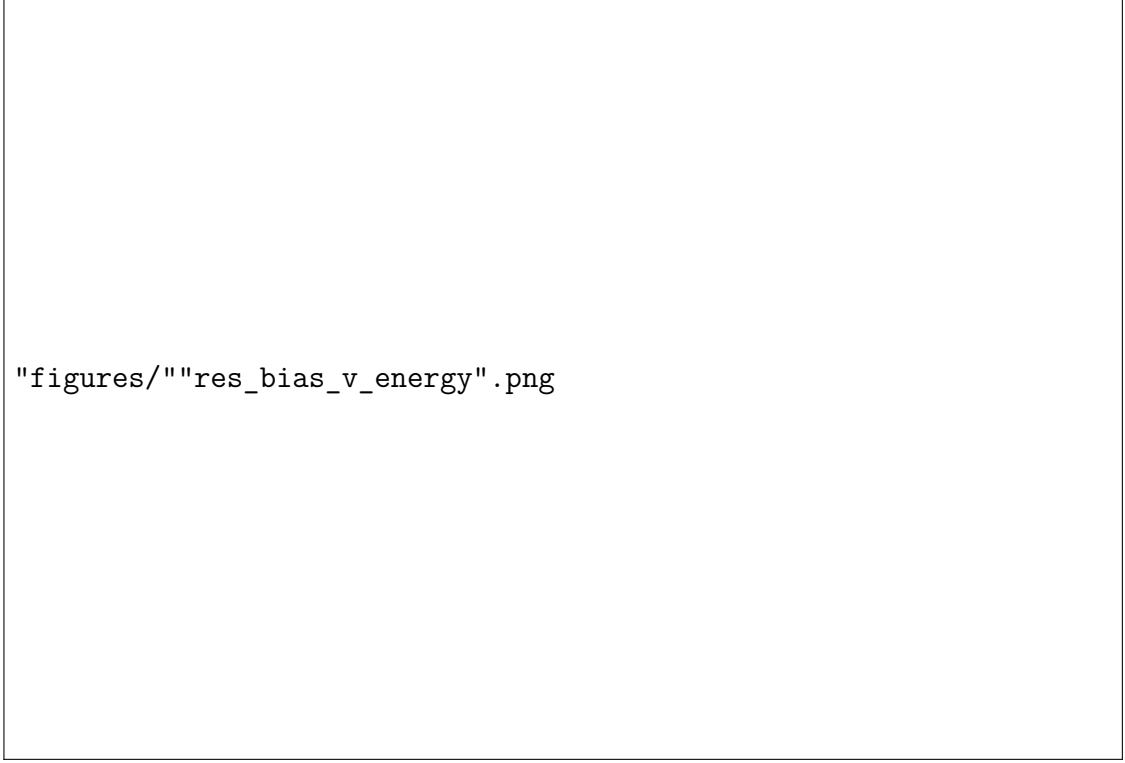
Figure 7.23: Fractional energy difference between reconstructed and true Michel electron energy.

is considered in bins of true Michel electron energy which are plotted in Figure 7.23. This difference is fit with a gaussian distribution in each bin in order to estimate the energy uncertainty and bias as a function of the true Michel electron energy.

The energy resolution and bias as a function of true Michel electron energy are estimated as the standard deviation and mean of the gaussian fit to the fractional energy difference in each energy bin, these values are plotted in Figure 7.24. TODO: analysis of results.

7.4 Conclusions

- Reco energy scaling
- Uncertainty vs energy
- Differences in dune far detector



"figures/""res_bias_v_energy".png

Figure 7.24: Energy resolution and bias as a function of true Michel electron energy.

8

Implications for DUNE

This chapter will analyse the implications of the measured uncertainties on analyses for the DUNE experiment. In particular the impact of the measured energy scale uncertainty and energy scale bias on supernova neutrino physics in DUNE will be analysed. The difference in conditions between ProtoDUNE–SP and DUNE will be highlighted and the expected implications for energy scale uncertainties in DUNE will be discussed.

The work for this section has yet to be started as it will be dependent on the outcome of the Michel electron analysis in the previous section. I expect to be able to start work on this analysis in September/October 2019 after preliminary results of the Michel electron analysis; work for this section will be completed by the end of December 2019.

8.1 Supernova Neutrinos in DUNE

8.2 Impacts of Energy Uncertainties

9

Conclusions

This chapter will summarise the work presented in the thesis and provide concluding remarks on the implications of the results for future analyses in LArTPC experiments.

References

- [1] G. et al. Vedovato. “GW170817: Observation of Gravitational Waves from a Binary Neutron Star Inspiral”. In: *Physical Review Letters* 119.16 (2017), pp. 30–33.
- [2] M. G. et al. Aartsen. “Multimessenger observations of a flaring blazar coincident with high-energy neutrino IceCube-170922A”. In: *Science* 361.6398 (2018). arXiv: [1807.08816](#).
- [3] Kate Scholberg. “Supernova Neutrino Detection”. In: *Ann. Rev. Nucl. Part. Sci.* 62 (2012), pp. 81–103. arXiv: [1205.6003 \[astro-ph.IM\]](#).
- [4] R. et al. Acciarri. “Long-Baseline Neutrino Facility (LBNF) and Deep Underground Neutrino Experiment (DUNE)”. In: (2016). arXiv: [1601.05471 \[physics.ins-det\]](#).
- [5] R. et al. Acciarri. “Design and Construction of the MicroBooNE Detector”. In: *JINST* 12.02 (2017), P02017. arXiv: [1612.05824 \[physics.ins-det\]](#).
- [6] F. Cavanna et al. “LArIAT: Liquid Argon In A Testbeam”. In: (2014). arXiv: [1406.5560 \[physics.ins-det\]](#).
- [7] M. et al. Antonello. “A Proposal for a Three Detector Short-Baseline Neutrino Oscillation Program in the Fermilab Booster Neutrino Beam”. In: (2015). arXiv: [1503.01520 \[physics.ins-det\]](#).
- [8] B. et al Abi. “The Single-Phase ProtoDUNE Technical Design Report”. In: (2017). arXiv: [1706.07081 \[physics.ins-det\]](#).
- [9] R. et al Acciarri. “Michel Electron Reconstruction Using Cosmic-Ray Data from the MicroBooNE LArTPC”. In: *JINST* 12.09 (2017), P09014. arXiv: [1704.02927 \[physics.ins-det\]](#).
- [10] E. Fermi. “Versuch einer Theorie der β -Strahlen. I”. In: *Zeitschrift für Physik* 88.3-4 (1934), pp. 161–177.
- [11] H. Bethe and R. Peierls. “The Neutrino”. In: *Nature* 133.532 (1934).
- [12] F. Reines and C. L. Cowan. “Detection of the free neutrino”. In: *Physical Review* 92.3 (1953), pp. 830–831.
- [13] G. Danby et al. “Observation of high-energy neutrino reactions and the existence of two kinds of neutrinos”. In: *Physical Review Letters* 9.1 (1962), pp. 36–44.
- [14] F. J. et al. Hasert. “Observation of neutrino-like interactions without muon or electron in the gargamelle neutrino experiment”. In: *Physics Letters B* 46.1 (1973), pp. 138–140.
- [15] K. et al. Kodama. “Observation of tau neutrino interactions”. In: *Physics Letters, Section B: Nuclear, Elementary Particle and High-Energy Physics* 504.3 (2001), pp. 218–224.

- [16] “Electroweak parameters of the Z^0 resonance and the standard model”. In: *Physics Letters B* 276.1 (1992), pp. 247–253. URL:
<http://www.sciencedirect.com/science/article/pii/037026939290572L>.
- [17] Raymond Davis, Don S. Harmer, and Kenneth C. Hoffman. “Search for neutrinos from the sun”. In: *Physical Review Letters* 20.21 (1968), pp. 1205–1209.
- [18] John N. Bahcall, Neta A. Bahcall, and Giora Shaviv. “Present status of the theoretical predictions for the Cl36 solar-neutrino experiment”. In: *Physical Review Letters* 20.21 (1968), pp. 1209–1212.
- [19] K. S. et al. Hirata. “Experimental study of the atmospheric neutrino flux”. In: *Physics Letters B* 205.2-3 (1988), pp. 416–420.
- [20] Y. et al. Fukuda. “Evidence for oscillation of atmospheric neutrinos”. In: *Physical Review Letters* 81.8 (1998), pp. 1562–1567.
- [21] Q. R. et al. Ahmad. “Direct Evidence for Neutrino Flavor Transformation from Neutral-Current Interactions in the Sudbury Neutrino Observatory”. In: *Physical Review Letters* 89.1 (2002), pp. 6–11. arXiv: 0204008v2 [arXiv:nucl-ex].
- [22] A. Yu. Smirnov. “Solar neutrinos: Oscillations or No-oscillations?” In: (Sept. 2016). arXiv: 1609.02386 [hep-ph].
- [23] K. et al. Eguchi. “First Results from KamLAND: Evidence for Reactor Antineutrino Disappearance”. In: *Physical Review Letters* 90.2 (2003), p. 6. arXiv: 0212021v1 [arXiv:hep-ex].
- [24] T. et al. Araki. “Measurement of neutrino oscillation with KamLAND: Evidence of spectral distortion”. In: *Physical Review Letters* 94.8 (2005), pp. 1–5. arXiv: 0406035v3 [arXiv:hep-ex].
- [25] N. et al. Agafonova. “Observation of a first ν_τ candidate event in the OPERA experiment in the CNGS beam”. In: *Physics Letters B* 691.3 (2010), pp. 138–145. URL: <http://linkinghub.elsevier.com/retrieve/pii/S0370269310007537>.
- [26] N. et al. Agafonova. “Final Results of the OPERA Experiment on ν_τ Appearance in the CNGS Neutrino Beam”. In: *Physical Review Letters* 120.21 (2018), p. 211801. URL: <https://doi.org/10.1103/PhysRevLett.120.211801>.
- [27] M. et al Aker. “First operation of the KATRIN experiment with tritium”. In: *Eur. Phys. J. C* 80.3 (2020), p. 264. arXiv: 1909.06069 [physics.ins-det].
- [28] Carlo Giunti et al. *Fundamentals of Neutrino Physics and Astrophysics*. eng. Oxford University Press, 2007.
- [29] M. et al. Tanabashi. “Review of Particle Physics”. In: *Phys. Rev. D* 98 (3 Aug. 2018), p. 030001. URL:
<https://link.aps.org/doi/10.1103/PhysRevD.98.030001>.
- [30] Stephen King. “Neutrino Mass and Mixing in the Seesaw Playground”. In: *Nuclear Physics B* 908 (Nov. 2015).
- [31] C. et al. Arnaboldi. “CUORE: A cryogenic underground observatory for rare events”. In: *Nuclear Instruments and Methods in Physics Research, Section A: Accelerators, Spectrometers, Detectors and Associated Equipment* 518.3 (2004), pp. 775–798. arXiv: 0212053 [hep-ex].

- [32] V. et al. Álvarez. “NEXT-100 technical design report (TDR). Executive summary”. In: *Journal of Instrumentation* 7.6 (2012). arXiv: [1202.0721](#).
- [33] S. et al. Andringa. “Current Status and Future Prospects of the SNO+ Experiment”. In: *Advances in High Energy Physics* 2016 (2016). arXiv: [1508.05759](#).
- [34] S. et al. Fukuda. “Solar 8B and hep Neutrino Measurements from 1258 Days of Super-Kamiokande Data”. In: *Phys. Rev. Lett.* 86 (25 June 2001), pp. 5651–5655. URL: <https://link.aps.org/doi/10.1103/PhysRevLett.86.5651>.
- [35] F. Capozzi et al. “Neutrino masses and mixings: Status of known and unknown 3ν parameters”. In: *Nucl. Phys.* B908 (2016), pp. 218–234. arXiv: [1601.07777 \[hep-ph\]](#).
- [36] K. et al. Abe. “Measurement of neutrino and antineutrino oscillations by the T2K experiment including a new additional sample of ν_e interactions at the far detector”. In: *Phys. Rev. D* 96 (9 Nov. 2017), p. 092006. URL: <https://link.aps.org/doi/10.1103/PhysRevD.96.092006>.
- [37] P. et al. Adamson. “Combined Analysis of ν_μ Disappearance and $\nu_\mu \rightarrow \nu_e$ Appearance in MINOS Using Accelerator and Atmospheric Neutrinos”. In: *Phys. Rev. Lett.* 112 (19 May 2014), p. 191801. URL: <https://link.aps.org/doi/10.1103/PhysRevLett.112.191801>.
- [38] M. A. et al. Acero. “First measurement of neutrino oscillation parameters using neutrinos and antineutrinos by NOvA”. In: *Phys. Rev. Lett.* 123 (15 Oct. 2019), p. 151803. URL: <https://link.aps.org/doi/10.1103/PhysRevLett.123.151803>.
- [39] F.P. et al An. “Observation of electron-antineutrino disappearance at Daya Bay”. In: *Phys. Rev. Lett.* 108 (2012), p. 171803. arXiv: [1203.1669 \[hep-ex\]](#).
- [40] Y. et al Abe. “First Measurement of θ_{13} from Delayed Neutron Capture on Hydrogen in the Double Chooz Experiment”. In: *Phys. Lett. B* 723 (2013), pp. 66–70. arXiv: [1301.2948 \[hep-ex\]](#).
- [41] J.K. et al Ahn. “Observation of Reactor Electron Antineutrino Disappearance in the RENO Experiment”. In: *Phys. Rev. Lett.* 108 (2012), p. 191802. arXiv: [1204.0626 \[hep-ex\]](#).
- [42] K. et al. Abe. “Constraint on the Matter-Antimatter Symmetry-Violating Phase in Neutrino Oscillations”. In: *Nature* 580 (2020), pp. 339–344. arXiv: [1910.03887](#). URL: <http://arxiv.org/abs/1910.03887>.
- [43] J.A. Formaggio and G.P. Zeller. “From eV to EeV: Neutrino Cross Sections Across Energy Scales”. In: *Rev. Mod. Phys.* 84 (2012), pp. 1307–1341. arXiv: [1305.7513 \[hep-ex\]](#).
- [44] Irene Tamborra et al. “Self-sustained asymmetry of lepton-number emission: A new phenomenon during the supernova shock-accretion phase in three dimensions”. In: *Astrophys. J.* 792.2 (2014), p. 96. arXiv: [1402.5418 \[astro-ph.SR\]](#).
- [45] K. et al Hirata. “Observation of a Neutrino Burst from the Supernova SN 1987a”. In: *Phys. Rev. Lett.* 58 (1987). Ed. by K.C. Wali, pp. 1490–1493.

- [46] R. M. et al. Bionta. “Observation of a neutrino burst in coincidence with supernova 1987A in the Large Magellanic Cloud”. In: *Phys. Rev. Lett.* 58 (14 Apr. 1987), pp. 1494–1496. URL: <https://link.aps.org/doi/10.1103/PhysRevLett.58.1494>.
- [47] Thomas J. Loredo and Don Q. Lamb. “Bayesian analysis of neutrinos observed from supernova SN-1987A”. In: *Phys. Rev. D* 65 (2002), p. 063002. arXiv: [astro-ph/0107260](#).
- [48] Alessandro Mirizzi et al. “Supernova Neutrinos: Production, Oscillations and Detection”. In: *Riv. Nuovo Cim.* 39.1-2 (2016), pp. 1–112. arXiv: [1508.00785 \[astro-ph.HE\]](#).
- [49] K. et al Abe. “Real-Time Supernova Neutrino Burst Monitor at Super-Kamiokande”. In: *Astropart. Phys.* 81 (2016), pp. 39–48. arXiv: [1601.04778 \[astro-ph.HE\]](#).
- [50] Babak et al Abi. “Deep Underground Neutrino Experiment (DUNE), Far Detector Technical Design Report, Volume II DUNE Physics”. In: (Feb. 2020). arXiv: [2002.03005 \[hep-ex\]](#).
- [51] R. et al Acciarri. “Long-Baseline Neutrino Facility (LBNF) and Deep Underground Neutrino Experiment (DUNE): Conceptual Design Report, Volume 2: The Physics Program for DUNE at LBNF”. In: (Dec. 2015). arXiv: [1512.06148 \[physics.ins-det\]](#).
- [52] Babak et al Abi. “Deep Underground Neutrino Experiment (DUNE), Far Detector Technical Design Report, Volume I Introduction to DUNE”. In: (Feb. 2020). arXiv: [2002.02967 \[physics.ins-det\]](#).
- [53] Babak et al Abi. “Deep Underground Neutrino Experiment (DUNE), Far Detector Technical Design Report, Volume IV Far Detector Single-phase Technology”. In: (Feb. 2020). arXiv: [2002.03010 \[physics.ins-det\]](#).
- [54] B. et al. Abi. “The Single-Phase ProtoDUNE Technical Design Report”. In: (2017). arXiv: [1706.07081](#). URL: <http://arxiv.org/abs/1706.07081>.
- [55] A.A. Machado and E. Segreto. “ARAPUCA a new device for liquid argon scintillation light detection”. In: *JINST* 11.02 (2016), p. C02004.
- [56] E. et al Segreto. “Liquid Argon test of the ARAPUCA device”. In: *JINST* 13.08 (2018), P08021. arXiv: [1805.00382 \[physics.ins-det\]](#).
- [57] B. Abi et al. “First results on ProtoDUNE-SP LArTPC performance from a test beam run at the CERN Neutrino Platform”. In: *Manuscript in preparation for submission to JINST* (2020).
- [58] R. Herbst et al. “Design of the SLAC RCE Platform: A general purpose ATCA based data acquisition system”. In: *2014 IEEE Nuclear Science Symposium and Medical Imaging Conference (NSS/MIC)*. 2014, pp. 1–4.
- [59] J. Anderson et al. “FELIX: a PCIe based high-throughput approach for interfacing front-end and trigger electronics in the ATLAS Upgrade framework”. In: *Journal of Instrumentation* 11.12 (Dec. 2016), pp. C12023–C12023. URL: <https://doi.org/10.1088%2F1748-0221%2F11%2F12%2Fc12023>.
- [60] K. Biery et al. “artdaq: An Event-Building, Filtering, and Processing Framework”. In: *IEEE Transactions on Nuclear Science* 60.5 (2013), pp. 3764–3771.

- [61] E. L. Snider and G. Petrillo. “LArSoft: Toolkit for simulation, reconstruction and analysis of liquid argon TPC neutrino detectors”. In: *Journal of Physics: Conference Series* 898.4 (2017).
- [62] C. Green et al. “The Art Framework”. In: *J. Phys. Conf. Ser.* 396 (2012). Ed. by Michael Ernst et al., p. 022020.
- [63] A.C. Booth et al. “Particle production, transport, and identification in the regime of 1–7 GeV/c”. In: *Phys. Rev. Accel. Beams* 22.6 (2019), p. 061003.
- [64] T. Roberts et al. “G4beamline Particle Tracking in Matter Dominated Beam Lines”. In: (Jan. 2008).
- [65] T.T. Böhlen et al. “The FLUKA Code: Developments and Challenges for High Energy and Medical Applications”. In: *Nuclear Data Sheets* 120 (2014), pp. 211–214. URL:
<http://www.sciencedirect.com/science/article/pii/S0090375214005018>.
- [66] D. Heck et al. “CORSIKA: A Monte Carlo code to simulate extensive air showers”. In: (Feb. 1998).
- [67] S. et al Agostinelli. “GEANT4: A Simulation toolkit”. In: *Nucl. Instrum. Meth. A* 506 (2003), pp. 250–303.
- [68] C. et al Adams. “Ionization electron signal processing in single phase LArTPCs. Part I. Algorithm Description and quantitative evaluation with MicroBooNE simulation”. In: *JINST* 13.07 (2018), P07006. arXiv: [1802.08709](https://arxiv.org/abs/1802.08709) [physics.ins-det].
- [69] J. S. Marshall and M. A. Thomson. “The Pandora software development kit for pattern recognition”. In: *European Physical Journal C* 75.9 (2015), pp. 1–16. arXiv: [1506.05348](https://arxiv.org/abs/1506.05348).
- [70] R. et al Acciarri. “The Pandora multi-algorithm approach to automated pattern recognition of cosmic-ray muon and neutrino events in the MicroBooNE detector”. In: *Eur. Phys. J. C* 78.1 (2018), p. 82. arXiv: [1708.03135](https://arxiv.org/abs/1708.03135) [hep-ex].
- [71] R. et al. Acciarri. “A study of electron recombination using highly ionizing particles in the ArgoNeuT Liquid Argon TPC”. In: *Journal of Instrumentation* 8.8 (2013). arXiv: [1306.1712](https://arxiv.org/abs/1306.1712).
- [72] I. Antcheva et al. “ROOT — A C++ framework for petabyte data storage, statistical analysis and visualization”. In: *Computer Physics Communications* 180.12 (2009), pp. 2499–2512. URL:
<http://www.sciencedirect.com/science/article/pii/S0010465509002550>.
- [73] M Adinolfi et al. “LHCb data quality monitoring”. In: *Journal of Physics: Conference Series* 898 (Oct. 2017), p. 092027. URL:
<https://doi.org/10.1088%2F1742-6596%2F898%2F9%2F092027>.
- [74] *Flask*. URL: <https://flask.palletsprojects.com>.
- [75] *The Bokeh Visualization Library*. URL: <https://bokeh.org>.
- [76] Travis Oliphant. *NumPy: A guide to NumPy*. USA: Trelgol Publishing. 2006–. URL: <http://www.numpy.org/>.
- [77] *Atomic and Nuclear Properties of Materials*. URL:
<http://pdg.lbl.gov/2017/AtomicNuclearProperties/>.

- [78] Yung-Su Tsai. “Pair Production and Bremsstrahlung of Charged Leptons”. In: *Rev. Mod. Phys.* 46 (1974). [Erratum: Rev.Mod.Phys. 49, 521–423 (1977)], p. 815.
- [79] Bruno Rossi. *High Energy Particles*. 1952.
- [80] *ESTAR: Stopping-power and range tables for electrons*. URL: <https://physics.nist.gov/PhysRefData/Star/Text/ESTAR.html>.
- [81] *XCOM:Photon Cross Sections Database*. URL: <https://www.nist.gov/pml/xcom-photon-cross-sections-database>.
- [82] R. et al Acciarri. “First Observation of Low Energy Electron Neutrinos in a Liquid Argon Time Projection Chamber”. In: *Phys. Rev. D* 95.7 (2017), p. 072005. arXiv: [1610.04102 \[hep-ex\]](https://arxiv.org/abs/1610.04102).
- [83] R Reed and RJ MarksII. *Neural smithing: supervised learning in feedforward artificial neural networks*. 1999.
- [84] Yann Lecun, Yoshua Bengio, and Geoffrey Hinton. “Deep learning”. In: *Nature* 521.7553 (2015), pp. 436–444. arXiv: [1807.07987](https://arxiv.org/abs/1807.07987).
- [85] Kaiming He et al. “Delving deep into rectifiers: Surpassing human-level performance on imagenet classification”. In: *Proceedings of the IEEE International Conference on Computer Vision* (2015), pp. 1026–1034. arXiv: [1502.01852](https://arxiv.org/abs/1502.01852).
- [86] Christian Szegedy et al. “Going deeper with convolutions”. In: *Proceedings of the IEEE Computer Society Conference on Computer Vision and Pattern Recognition*. 2015. arXiv: [1409.4842](https://arxiv.org/abs/1409.4842).
- [87] George Cybenko. “Approximation by superpositions of a sigmoidal function”. In: *MCSS* 2 (1989), pp. 303–314.
- [88] L. D. Jackel et al. *Backpropagation Applied to Handwritten Zip Code Recognition*. 2008. arXiv: [1004.3732](https://arxiv.org/abs/1004.3732).
- [89] Y. LeCun, K. Kavukcuoglu, and C. Farabet. “Convolutional networks and applications in vision”. In: *Proceedings of 2010 IEEE International Symposium on Circuits and Systems*. 2010, pp. 253–256.
- [90] *NN-SVG: Publication ready NN–architecture schematics*. URL: <http://alexlenail.me/NN-SVG>.
- [91] Kaiming He et al. “Deep Residual Learning for Image Recognition”. In: *The IEEE Conference on Computer Vision and Pattern Recognition (CVPR)*. June 2016.
- [92] Russell D. Reed and Robert J. Marks. *Neural Smithing: Supervised Learning in Feedforward Artificial Neural Networks*. Cambridge, MA, USA: MIT Press, 1998.
- [93] David E Rumelhart, Geoffrey E Hinton, and Ronald J Williams. “Learning representations by back-propagating errors”. In: *Nature* 323.6088 (1986), pp. 533–536. URL: <https://doi.org/10.1038/323533a0>.
- [94] A. Aurisano et al. “A Convolutional Neural Network Neutrino Event Classifier”. In: *JINST* 11.09 (2016), P09001. arXiv: [1604.01444 \[hep-ex\]](https://arxiv.org/abs/1604.01444).
- [95] R. et al Acciarri. “Convolutional Neural Networks Applied to Neutrino Events in a Liquid Argon Time Projection Chamber”. In: *JINST* 12.03 (2017), P03011. arXiv: [1611.05531 \[physics.ins-det\]](https://arxiv.org/abs/1611.05531).

- [96] Martin Abadi et al. “TensorFlow: A system for large-scale machine learning”. In: *12th USENIX Symposium on Operating Systems Design and Implementation (OSDI 16)*. 2016, pp. 265–283. URL: <https://www.usenix.org/system/files/conference/osdi16/osdi16-abadi.pdf>.
- [97] Nitish Srivastava et al. “Dropout: a simple way to prevent neural networks from overfitting”. In: *Journal of Machine Learning Research* 15 (2014), pp. 1929–1958.
- [98] Michael Mooney. “The MicroBooNE Experiment and the Impact of Space Charge Effects”. In: *Proceedings, Meeting of the APS Division of Particles and Fields (DPF 2015): Ann Arbor, Michigan, USA, 4-8 8 2015*. 2015. arXiv: [1511.01563 \[physics.ins-det\]](https://arxiv.org/abs/1511.01563).
- [99] Tom Fawcett. “An Introduction to ROC Analysis”. In: *Pattern Recognition Letters* 27.8 (2006), pp. 861–874.